1   **Sphingosine 1-phosphate-regulated transcriptomes in heterogenous arterial and lymphatic**

2   **endothelium of the aorta**

3

4   Eric Engelbrecht[#,1], Michel V. Levesque[#,1], Liqun He[2,3], Michael Vanlandewijck[2,3], Anja

5   Nitzsche[4], Andrew Kuo[1], Sasha A. Singh[5], Masanori Aikawa[5], Kristina Holton[6], Richard L Proia[7],

6   Mari Kono[7], William T. Pu[8,9], Eric Camerer[4], Christer Betsholtz[2,3], Timothy Hla[1,*]

7

8   [1]*Vascular Biology Program, Boston Children's Hospital, Deapartment of Surgery, Harvard*

9   *Medical School, Boston, MA, USA*

10   [2]*Department of Immunology, Genetics and Pathology, Rudbeck Laboratory, Uppsala University,*

11   *Uppsala, Sweden*

12   [3]*Karolinska Institutet/AstraZeneca Integrated Cardio Metabolic Centre (KI/AZ ICMC),*

13   *Karolinska Institutet, Blickagången 6, SE-141 57 Huddinge, Sweden.*

14   [4]*Université de Paris, INSERM U970, Paris Cardiovascular Research Center, Paris, France*

15   [5]*Center for Interdisciplinary Cardiovascular Sciences, Department of Medicine, Brigham and*

16   *Women's Hospital, Harvard Medical School, Boston, MA*

17   [6]*Harvard Medical School Research Computing, Boston, MA, USA*

18   [7]*Genetics of Development and Disease Branch, National Institute of Diabetes and Digestive and*

19   *Kidney Diseases, National Institutes of Health, Bethesda, MD, USA*

20   [8]*Department of Cardiology, Boston Children's Hospital, Harvard Medical School, Boston, MA,*

21   *USA*

22   [9]*Harvard Stem Cell Institute, Harvard University, Cambridge, MA, USA*

23

24   *- Corresponding author, email: Timothy.Hla@childrens.harvard.edu

25   #- Eric Engelbrecht and Michel Levesque contributed equally to this study.

Abstract

Despite the medical importance of G protein-coupled receptors (GPCRs), *in vivo* cellular heterogeneity of GPCR signaling and downstream transcriptional responses are not understood. We report the comprehensive characterization of transcriptomes (bulk and single-cell) and chromatin domains regulated by sphingosine 1-phosphate receptor-1 (S1PR1) in adult mouse aortic endothelial cells. First, S1PR1 regulates NFκB and nuclear glucocorticoid receptor pathways to suppress inflammation-related mRNAs. Second, spatially distinct S1PR1 signaling in the aorta is associated with heterogenous endothelial cell (EC) subtypes. For example, a transcriptomically distinct arterial EC population at vascular branch points (aEC1) exhibits ligand-independent S1PR1/ß-arrestin coupling. In contrast, circulatory S1P-dependent S1PR1/ß-arrestin coupling was observed in non-branch point aEC2 cells that exhibit an inflammatory signature. Moreover, an adventitial lymphatic EC (LEC) population shows suppression of lymphangiogenic and inflammation-related transcripts in a S1P/S1PR1-dependent manner. These insights add resolution to existing concepts of GPCR signaling and S1P biology.

3

Introduction

42

43   Sphingosine 1-phosphate (S1P), a circulating lipid mediator, acts on G protein-coupled

44 S1P receptors (S1PRs) to regulate a variety of organ systems. S1PR1, abundantly expressed by

45 vascular endothelial cells (ECs), responds to both circulating and locally-produced S1P to regulate

46 vascular development, endothelial barrier function, vasodilatation and inflammation (Proia & Hla,

47 2015).

48   S1P binding to S1PR1 activates heterotrimeric $G_{\alpha i/o}$ proteins, which regulate downstream

49 signaling molecules such as protein kinases, small GTPases, and other effector molecules to

50 influence cell behaviors, such as shape, migration, adhesion and cell-cell interactions. Even though

51 S1PR1 signaling is thought to evoke transcriptional responses that couple rapid signal transduction

52 events to long-term changes in cell behavior, such mechanisms are poorly understood, especially

53 in the vascular system.

54   Subsequent to $G_{\alpha i/o}$ protein activation, the S1PR1 C-terminal tail gets phosphorylated and

55 binds to ß-arrestin, leading to receptor desensitization and endocytosis (Liu et al., 1999; Oo et al.,

56 2007). While S1PR1 can be recycled back to the cell surface for subsequent signaling, sustained

57 receptor internalization brought about by supra-physiological S1P stimulation or functional

58 antagonists leads to recruitment of ubiquitin ligases and lysosomal/proteasomal degradation of the

59 receptor (Oo et al., 2011). Thus, ß-arrestin coupling down-regulates S1PR1 signals. However,

60 studies of other GPCRs suggest that ß-arrestin coupling could lead to biased signaling distinct

61 from $G_{\alpha i/o}$ -regulated events (Wisler, Rockman, & Lefkowitz, 2018). Distinct transcriptional

62 changes brought about by $G_{\alpha i/o}$ – and ß-arrestin-dependent pathways are not known.

63   Our understanding of GPCR signaling *in vivo* is limited. To address this, Kono et al. (2014)

64 developed S1PR1 reporter mice which record receptor activation at single-cell resolution (Kono

4

65   et al., 2014). Adapted from the "Tango" system (Barnea et al., 2008), S1PR1-GFP signaling

66   (S1PR1-GS) mice convert ß-arrestin recruitment to the GPCR to H2B-GFP expression (Kono et

67   al., 2014). We previously used the S1PR1-GS mouse and showed that high levels of endothelial

68   GFP expression (i.e. S1PR1/ß-arrestin coupling) are prominent at the lesser curvature of the aortic

69   arch and the orifices of intercostal branch points (Galvani et al., 2015). In addition, inflammatory

70   stimuli (e.g. lipopolysaccharide) induced rapid coupling of S1PR1 to ß-arrestin and GFP

71   expression in endothelium in an S1P-dependent manner (Kono et al., 2014). These data suggest

72   that the S1PR1-GS mouse is a valid model to study GPCR activation in vascular ECs *in vivo*.

73   To gain insights into the molecular mechanisms of S1PR1 regulation of endothelial

74   transcription and the heterogenous nature of S1PR1 signaling *in vivo*, we performed bulk

75   transcriptome and open chromatin profiling of GFP^{high} and GFP^{low} aortic ECs from S1PR1-GS

76   mice. We also performed transcriptome and open chromatin profiling of aortic ECs in which *S1pr1*

77   was genetically ablated (*S1pr1-ECKO*) (Galvani et al., 2015). In addition, we conducted single-

78   cell (sc) RNA-seq of GFP^{low} and GFP^{high} aortic ECs. Our results show that S1PR1 suppresses the

79   expression of inflammation-related mRNAs by inhibiting the NFκB pathway. Second, the high

80   S1PR1 signaling ECs (GFP^{high} cells) are more similar to *S1pr1-ECKO* ECs at the level of the

81   transcriptome. Third, scRNA-seq revealed eight distinct aorta-associated EC populations

82   including six arterial EC subtypes, adventitial lymphatic ECs, and venous ECs, the latter likely

83   from the vasa vasorum. S1PR1 signaling was highly heterogenous within these EC subtypes but

84   was most frequent in adventitial LECs and two arterial EC populations. Immunohistochemical

85   analyses led to anatomical localization of these aortic EC populations and defined markers. In the

86   lymphatic ECs of the aorta, S1PR1 signaling restrains inflammatory and immune-related

87   transcripts. These studies provide a comprehensive resource of transcriptional signatures in aortic

88   ECs, which will be useful to further investigate the multiple roles of S1P in vascular physiology

89   and disease.

90

Results

Profiling the transcriptome of GFP^{high} and GFP^{low} mouse aortic endothelium

93   S1PR1 expression in aortic endothelium is relatively uniform (Galvani et al., 2015).

94   However, S1PR1 coupling to ß-arrestin, as reported by H2B-GFP expression in S1PR1-GS mice,

95   exhibits clear differences in specific areas of the aorta. For example, thoracic aortae of S1PR1-GS

96   mice show high levels of GFP expression in ECs at intercostal branch points (Galvani et al., 2015),

97   but not in ECs of control mice harboring only the *H2B-GFP* reporter allele (Figure 1A). The first

98   2-3 rows of cells around the circumference of branch point orifices exhibit the greatest GFP

99   expression (Figure 1A). In addition, heterogeneously dispersed non-branch point GFP+ ECs were

100   also observed, including at the lesser curvature of the aortic arch (Figure 1A). Areas of the aorta

101   that are distal (> ~10 cells) from branch points, as well as the greater curvature, exhibit relatively

102   low frequencies of GFP+ ECs (Figure 1A). GFP+ mouse aortic ECs (MAECs) are not co-localized

103   with Ki-67, a marker of proliferation, suggesting that these cells are not actively cycling (Figure

104   1A). However, fibrinogen staining was frequently co-localized with GFP+ MAECs, suggesting

105   that ß-arrestin recruitment to S1PR1 was associated with increased vascular leak (Figure 1A).

106   These findings suggest sharp differences in S1PR1 signaling throughout the normal mouse aortic

107   endothelium.

108   For insight into the aortic endothelial transcriptomic signature associated with high levels

109   of S1PR1/ß-arrestin coupling, we harvested RNA from fluorescent-activated cell sorted (FACS)

110   GFP^{high} and GFP^{low} MAECs and performed RNA-seq (Figure 1B). To identify genes that are

6

111 regulated by S1PR1 signaling, we sorted MAECs from tamoxifen-treated *Cdh5*-Cre[ERT2] *S1pr1*[f/f]

112 (*S1pr1-ECKO*) and *S1pr1*[f/f] (*S1pr1-WT*) littermates (Figure 1-figure supplement 1A). We noted

113 that GFP[high], GFP[low], *S1pr1-WT* and *S1pr1-ECKO* MAECs each expressed endothelial lineage

114 genes (*Pecam1*, *Cdh5*) and lacked hematopoietic and VSMC markers (*Ptprc, Gata1,* and *Myocd*),

115 validating our MAEC isolation procedure (Figure 1-figure supplement 1B). Efficient CRE-

116 mediated recombination of *S1pr1* was confirmed in sorted MAECs from *S1pr1-ECKO* mice

117 (Figure 1-figure supplement 1B).

118 Differential expression analysis using edgeR identified 1,103 GFP[high]-enriched and 1,042

119 GFP[low]-enriched transcripts (p-value < 0.05) (Figure 1C and Figure 1-figure supplement 1B; see

120 also Supplementary File 1). In contrast, *S1pr1-ECKO* MAECs showed fewer differentially

121 expressed genes (DEGs), with 258 up- and 107 down-regulated transcripts (Figure 1C and Figure

122 1-figure supplement 1C; see also Supplementary File 1). Intersection of these two sets of DEGs

123 showed that only 9.5% (204 transcripts) were common (Figure 1C and Supplementary File 1),

124 suggesting that the majority (~90%) of transcripts that are differentially expressed in MAECs from

125 S1PR1-GS mice are not regulated by S1PR1 signaling. Rather, S1PR1/ß-arrestin coupling may

126 correlate with heterogenous EC subtypes in the mouse aorta.

127 Among the 204 common DEGs, 151 were both *S1pr1-ECKO* upregulated and enriched in

128 the GFP[high] population (Figure 1C). In contrast, much lower numbers of transcripts were found in

129 the intersection of GFP[high] and *S1pr1-ECKO* downregulated (7 transcripts), GFP[low] and *S1pr1-*

130 *ECKO* upregulated (8 transcripts) and GFP[low] and *S1pr1-ECKO* downregulated (38 transcripts)

131 (Figure 1C). We computed the statistical significance of these gene set overlaps using the

132 GeneOverlap R package (Shen et al., 2013). The GFP[high]:*S1pr1-ECKO*-up overlap was significant

133 (151 transcripts, p-value = 3.80E-126), as was the GFP[low]:*S1pr1-ECKO*-down overlap (38

134   transcripts, p-value = 3.80E-126), and the other two tested overlaps were not significant (p-value

135   > 0.3) (Figure 1-figure supplement 1E). These data suggest that the transcriptome of MAECs

136   exhibiting high S1PR1/ß-arrestin coupling (GFP^{high}) is more similar to that of *S1pr1-ECKO*.

137   We used Ingenuity Pathway Analysis (IPA®, Qiagen) to examine biological processes

138   regulated by S1PR1 signaling and loss of function in MAECs. Transcripts involved in

139   inflammatory processes were prominently up-regulated in both GFP^{high} and *S1pr1-ECKO* MAECs

140   (Figure 1D; see also Supplementary File 2). For example, positive tumor necrosis factor (TNF)-α,

141   lipopolysaccharide, and interferon-γ signaling were observed in both *S1pr1-ECKO* and GFP^{high}

142   MAECs. In contrast, a negative glucocorticoid signature was observed in these cells (Figure 1D).

143   Examples of differentially regulated transcripts are chemokines (*Ccl2*, *Clc5*, *Ccl7*, *Ccl21c*),

144   cytokines (*Il33*, *Il7*), inflammatory modulators (*Irf8*, *NFκBie*, *TNFaip8l1*) and cyclooxygenase-2

145   (*Ptgs2*) (Figure 1E and Figure 1-figure supplements 1C and 1D). This suggests that S1PR1

146   suppresses inflammatory gene expression in mouse aortic endothelium. We noted that transcripts

147   in the TGFß signaling pathway (*Thbs1*, *Smad3*, *Bmpr1a*, *Col4a4*, *Pcolce2*) were prominently

148   downregulated in the GFP^{high} population (Figure 1D and Figure 1-figure supplement 1C).

149   Furthermore, both GFP^{high} and *S1pr1-ECKO* MAECs were enriched with *Lyve1*, *Flt4*, and *Ccl21c*

150   transcripts, which encode proteins with well-defined roles in lymphatic EC (LEC) differentiation

151   and function (Ulvmar & Makinen, 2016) (Figure 1E, Figure 1-figure supplement 1F). Taken

152   together, these data suggest that S1PR1 represses expression of inflammatory genes in aortic

153   endothelium and that GFP^{high} MAECs include aorta-associated LECs and are heterogeneous.

154   **Chromatin accessibility landscape of MAECs**

155   We used the assay for transposase-accessible chromatin with sequencing (ATAC-seq)

156   (Buenrostro, Giresi, Zaba, Chang, & Greenleaf, 2013) to identify putative *cis*-elements that

8

157   regulate differential gene expression between GFP^{high} versus GFP^{low} and *S1pr1-WT* versus *S1pr1-*

158   *ECKO* MAECs. ATAC-seq utilizes a hyper-active Tn5 transposase (Adey et al., 2010) that

159   simultaneously cuts DNA and ligates adapters into sterically unhindered chromatin. This allows

160   for amplification and sequencing of open chromatin regions containing transcriptional regulatory

161   domains such as promoters and enhancers. After alignment, reads from three experiments were

162   trimmed to 10 bp, centered on Tn5 cut sites, then merged. These merged reads were used as inputs

163   to generate two peak sets (MACS2, FDR < 0.00001) of 73,492 for GFP^{low} MAECs and 65,694 for

164   GFP^{high} MAECs (Figure 2A). MAECs isolated from *WT* and *S1pr1-ECKO* mice harbored 93,859

165   and 76,082 peaks, respectively (Figure 2A). Peaks were enriched in promoter and intragenic

166   regions (Figure 2-figure supplement 1A). We noted that the *Cdh5* gene exhibited numerous open

167   chromatin peaks, while *Gata1* was inaccessible (Figure 2-figure supplement 1B). Furthermore, we

168   observed a global correlation between chromatin accessibility and mRNA expression for all 20,626

169   annotated coding sequences (CDS's) in the NCBI RefSeq database (Figure 2-figure supplement

170   2). These data suggest that our ATAC-seq data is of sufficient quality for detailed interrogation.

171   Differential chromatin accessibility analysis of GFP^{high} versus GFP^{low} MAECs identified

172   501 peaks with reduced accessibility (GFP^{low} peaks) and 3,612 peaks with greater accessibility

173   (GFP^{high} peaks) in GFP^{high} MAECs (FDR < 0.05, Figure 2B and Supplementary File 3). For *WT*

174   and *ECKO* counterparts, this analysis identified 303 peaks with reduced accessibility (*S1pr1-WT*

175   peaks) and 472 peaks with enhanced accessibility (*S1pr1-ECKO* peaks) in *S1pr1-ECKO* MAECs

176   (Figure 2B and Supplementary File 3). The ~7-fold higher number of GFP^{high}-enriched peaks

177   suggests that GFP^{high} MAECs are more "activated" (elevated number of chromatin remodeling

178   events) and/or are a heterogeneous mixture of EC subtypes.

179 To identify relevant transcription factors (TFs), we used the Hypergeometric Optimization

180 of Motif EnRichment (HOMER) (Heinz et al., 2010) suite of tools to reveal over-represented

181 motifs in each set of differentially accessible peaks (DAPs). GFP^{high} peaks were enriched with

182 p65-NFκB, AP-1, STAT3, SOX17, COUP-TFII, and NUR77 motifs (Figure 2C and

183 Supplementary File 3). In contrast, GFP^{low} peaks showed reduced occurrence of these motifs

184 (Figure 2D). *S1pr1-ECKO* peaks were enriched with p65-NFκB motifs, while *S1pr1-WT* peaks

185 were markedly enriched with glucocorticoid response elements (GREs) and modestly enriched

186 with STAT3, GATA2, ATF1, SOX17 and COUP-TFII motifs (Figure 2E and 2F). Examination of

187 ATAC-seq reads centered on selected binding sites (p65, NUR77, COUP-TFII, ATF1, GATA2,

188 and GRE) showed local decreases in accessibility at motif centers, suggestive of chromatin

189 occupancy by these factors (Figures 2G and 2H).

190 We used the ATAC-seq footprinting software HINT-ATAC (Z. Li et al., 2019) to assess

191 genome-wide putative chromatin occupancy by TFs. HINT-ATAC identified enhanced

192 footprinting scores at NFKB1 and NFKB2 motifs in *S1pr1-ECKO* MAECs, whereas GFP^{high}

193 MAECs showed increasesd scores at RELA motifs and to a lesser extent at NFKB1 and NFKB2

194 motifs (Figure 2-figure supplement 3A and 3B). This analysis also identified motifs of the

195 TCF/LEF family (LEF1, TCF7, TCF7L2) as GFP^{high}-enriched, but not *S1pr1-ECKO*-enriched

196 (Figure 2-figure supplement 3A-D). Consistent with HOMER analysis of DAPs, HINT-ATAC

197 identified NR2F2 (COUP-TFII), NR4A1 (NUR77), TCF4, and SOX17 motifs as exhibiting greater

198 footprinting scores in GFP^{high} MAECs, while GFP^{low} MAECs showed enhanced putative

199 chromatin occupancy at ATF1 motifs.

200 Analysis of DAPs showed that only the p65-NFκB motif was commonly enriched between

201 GFP^{high} and *S1pr1-ECKO* MAECs. This observation is consistent with our RNA-seq analysis,

10

202 which identified cytokine/NFκB pathway suppression by S1PR1 signaling in MAECs (Figure 1D).

203 Enrichment of COUP-TFII, NUR77, and AP-1/bZIP motifs in open chromatin of GFP^{high} MAECs,

204 but not *S1pr1-ECKO* MAECs, further suggests that high levels of S1PR1/ß-arrestin coupling

205 occurs in heterogenous populations of aortic ECs.

206

Single-cell RNA-seq analysis of GFP^{high} and GFP^{low} MAECs reveals 8 distinct EC clusters

208 Imaging studies demonstrated that GFP^{high} MAECs are restricted to specific anatomical

209 locations. To test the hypothesis that these represent specific EC subpopulations, we employed

210 single-cell RNA-seq (scRNA-seq) on FACS-sorted GFP^{high} and GFP^{low} MAECs. In total, 1152

211 cells were sequenced (768 GFP^{high} and 384 GFP^{low}) using the Smart-seq2 protocol. An average of

212 300,000 aligned reads/cell were obtained and corresponded to ~3,200 transcripts/cell. *Cdh5*

213 transcripts were broadly detected, consistent with endothelial enrichment of sorted cells (Figure 3-

214 figure supplement 1A). *S1pr1* and *Arrb2* were also broadly detected (Figure 3-figure supplement

215 1A), suggesting that receptor activation rather than expression of these factors accounts for

216 heterogenous reporter expression in MAECs.

217 Analysis of GFP^{high} and GFP^{low} MAECs using a custom velocyto/pagoda2 pipeline (Fan et

218 al., 2016; La Manno et al., 2018) revealed 9 clusters upon T-distributed stochastic neighborhood

219 embedding (t-SNE) projection (Figure 3A). 6 of the 9 clusters grouped together in a "cloud",

220 whereas 3 clusters formed distinct populations. We used hierarchical differential expression

221 analysis to identify signature marker genes of each cluster (Figure 3B).

222 Genes uniquely detected in one of the distinct clusters included vascular smooth muscle

223 cell (VSMC)-specific transcripts such as *Myh11*, *Myom1*, and *Myocd* (Figure 3B and 3C; Figure

224 3-figure supplement 1B). Therefore, this cluster was designated VSMC-like as these cells may

11

225   represent MAECs sorted along with fragments of VSMCs, or "doublets" of ECs and VSMCs.

226   Because these cells may represent contamination in an otherwise pure pool of aortic ECs, we

227   omitted this VSMC-like cluster from subsequent analyses. The remaining eight EC clusters were

228   further analyzed.

229   Lymphatic EC (LEC) markers such as *Flt4* (VEGFR3), *Prox1*, and *Lyve1*, as well as the

230   venous marker *Nr2f2* (COUP-TFII), were detected in a distinct cluster (Figures 3B and 3D; Figure

231   3-figure supplement 1B). A smaller but nonetheless distinct cluster of ECs was also enriched with

232   *Nr2f2* transcripts but lacked lymphatic markers, suggesting that these cells are of venous origin

233   (Figures 3B and 3E; Figure 3-figure supplement 1B). Arterial lineage markers *Sox17, Gja5* and

234   *Notch4* were expressed in the 6 clusters comprising the "cloud" of ECs (aEC1-6) (Figures 3B and

235   3F; Figure 3-figure supplement 1B).

236   We individually compared LECs, vECs, and VSMCs to the remainder of ECs as a "pseudo-

237   bulk" cluster to generate a list of transcripts enriched (Z-score > 3) for each of these three clusters.

238   We performed the same analysis for aEC1, aEC2, aEC3, aEC4, aEC5, and aEC6, but used only

239   arterial ECs as the comparator. For example, aEC1-enriched transcripts were identified by

240   generating a "pseudo-bulk" merge of all aEC2, aEC3, aEC4, aEC5, and aEC6 cells, while aEC2-

241   enriched transcrips were compared to the pseudo-bulk merge of aEC1, aEC3, aEC4, aEC5, and

242   aEC6. The top 32 transcripts that resulted from this analysis are shown in Figure 3-figure

243   supplement 2. Among the arterial clusters, aEC1 and aEC2 harbored the greatest numbers of

244   enriched transcripts (Z-score > 3) with 411 and 1517, respectively (Figure 3-figure supplement

245   3A; see also Supplementary File 4). We noted that aEC5 exhibited the fewest (77) enriched

246   transcripts (Figure 3-figure supplement 3A). Representative marker genes of aEC1, aEC2, aEC3,

247   and aEC4 are shown in t-SNE embedding in Figure 3G-J.

248   LEC (97% GFP^{high}), vEC (100% GFP^{high}), aEC1 (97% GFP^{high}) and aEC2 (92% GFP^{high})

249   harbored the greatest proportion of GFP^{high} MAECs, suggesting that S1PR1/ß-arrestin coupling is

250   robust in these ECs subtypes (Figure 3-figure supplement 3A and 3B). In contrast, aEC3-6

251   contained lower frequencies of GFP^{high} MAECs. aEC4 (30% GFP^{high}) exhibited the lowest

252   frequency of MAECs with S1PR1/ß-arrestin coupling. The GFP^{high}-dominated clusters (LEC,

253   vEC, aEC1, and aEC2) were enriched with several transcripts related to sphingolipid metabolism,

254   such as *Spns2*, *Sptlc2*, *Ugcg*, *Enpp2*, *Ormdl3*, *Degs1*, and *Sgms2* (Figure 3-figure supplement 4A;

255   see also Supplementary File 5). Notably, *S1pr1* transcripts were enriched in aEC1 cells by ~1.8-

256   fold relative to the remainder of arterial ECs (Figure 3-figure supplement 4A; see also

257   Supplementary File 4).

258   Pagoda2 clustering suggested that aEC1 cells were more similar to LECs and vECs than to

259   the remainder of arterial ECs. This is illustrated by the first split of the hierarchical clustering

260   dendrogram, which separated LEC, vEC, and aEC1 from the remainder of arterial ECs (aEC2-6)

261   (Figure 3B). To identify genes that underlie the similarity between LEC, vEC, and aEC1, we

262   identified all transcripts commonly enriched (46 transcripts, Z-score > 3) and depleted (92

263   transcripts, Z-score < -3) in each of these 3 clusters when individually compared to a pseudo-bulk

264   merge of aEC2-6 (Supplementary File 4). Examples of LEC, vEC, and aEC1 co-enriched

265   transcripts were *Itga6*, *Apold1*, *Kdr*, *Fabp4*, *Robo4*, *Tcf4*, and *Adgrf5* (Figure 3-figure supplement

266   4B). Conversely, *Sod3*, *Pcolce2*, *Col4a4*, *Frzb*, *Sfrp1*, *Gxylt2*, and *Bmpr1a* were depleted from

267   LEC, vEC, and aEC1. Notably, these depleted transcripts were highly enriched in aEC4, which is

268   30% GFP^{high} MAECs. In contrast, LEC, vEC, and aEC1 are each > 95% GFP^{high}.

269   We note that the abovementioned transcripts (Figure 3-figure supplement 4B) were among

270   those most differentially expressed between GFP^{high} and GFP^{low} MAECs by bulk RNA-seq (Figure

13

271 1-figure supplement 1C). This is demonstrative of consistency between our bulk and single-cell

272 datasets.

273   For functional insights into arterial EC clusters, we analyzed aEC1-aEC4 enriched

274 transcripts with the Gene Set Enrichment Analysis (GSEA) tool (Figures 4A-D). aEC1 cells were

275 enriched with transcripts associated with GPCR/MAPK signaling (*Rasgrp3*, *Rapgef4*, *Rgs10*,

276 *Mapk4k3*, *S1pr1*) as well as VEGF, integrin, and tight-junction pathways (*Flt1*, *Vegfc*, *Pgf*, *Igf2*,

277 *Vcan*, *Sema3g*, *S100a4*, *Jam2*, *Cldn5*). The aEC2 cluster presented a different profile with enriched

278 terms related to immune/inflammatory pathways, TGFß signaling and mRNA processing.

279 Elevated expression of *Vcam1*, *Icam1*, *Traf6*, *Cxcl12* and *NFkb1* may suggest that these ECs

280 represent an inflammatory cluster.

281   In contrast, aEC3 cells were enriched with "immediate-early" transcripts, including those

282 of the AP-1 transcription factor family (*Atf3*, *Jun*, *Jund*, *Junb*, *Fos*, *Fosb*). Enhanced expression of

283 *Atf3* and related TFs of the bZIP family in aEC3 may have contributed to increased accessibility

284 at ATF, FOSB::JUN, and FOSB::JUNB binding sites in GFP^{low} MAECs (Figure 2D and 2G;

285 Figure 2-figure supplement 3C). Notably, a recent study of young (8-week) and aged (18-month)

286 normal mouse aortic endothelium also identified a cluster of *Atf3*-positive cells only in young

287 endothelium, as determined by both scRNA-seq and immunostaining for ATF3 (McDonald et al.,

288 2018). Markers of these cells were also identified as top aEC3 markers (e.g. *Fosb*, *Jun*, *Jund*, *Junb*,

289 *Dusp1*) suggesting that aEC3 cells are similar to the regenerative *Atf3*-positive cluster described

290 by McDonald et al. (2018).

291   aEC4 cells were enriched with transcripts related to cell-ECM interations,

292 glycosaminoglycan metabolism, and collagen formation (*Pcolce2*, *Frzb*, *Spon1*, *Col4a4*, *Mfap5*,

293 *Hyal2*). The other two arterial clusters (aEC5 and aEC6) appeared less distinctive (i.e. harbored

14

294 relatively few enriched transcripts with high Z-scores and fold change values) and therefore were

295 not analyzed. Collectively, these data suggest that scRNA-seq identified more than four distinct

296 MAEC subtypes with unique transcriptomic signatures.

297 Next, we integrated our dataset with information from two recent scRNA-seq studies that

298 also sub-categorized ECs of the normal mouse aorta (Kalluri et al., 2019; Lukowski et al., 2019).

299 Lukowski et al. (2019) sequenced individual FACS-sorted Lineage$^-$CD34$^+$ cells and identified 2

300 major EC clusters, designated "Cluster 1" and "Cluster 2". Kalluri et al. (2019) identified 3 major

301 EC clusters by sequencing individual cells from whole-aorta digests. Both studies used 10x

302 Genomics droplet sequencing for cell capture and gene expression library preparation. Top

303 markers of "Cluster 1" (Lukowski et al., 2019) were primarily expressed by LEC, vEC and aEC1

304 (Figure 4-figure supplement 1A). "Cluster 1" shared markers with "EC2" (Kalluri et al., 2019),

305 such as *Rgcc*, *Rbp7*, *Cd36*, *Gpihbp1* (Figure 4-figure supplement 1A and 1B). Similarly, several

306 "EC2" markers, while enriched in aEC1 relative to aEC2-6 (e.g. *Flt1*, *Rgcc*), were also expressed

307 in LEC and vEC (e.g. *Pparg*, *Cd36*, *Gpihbp1*, *Rbp7*) (Figure 4-figure supplement 1B). "EC3"

308 (Kalluri et al., 2019) markers were strongly enriched in LEC and vEC (e.g. *Nr2f2*, *Flt4*, *Lyve1*),

309 and the authors noted that these cells were likely of lymphatic origin (Figure 4-figure supplement

310 1B). The remaining two clusters, "Cluster 2" (Lukowski et al., 2019) and "EC1" (Kalluri et al.,

311 2019), strongly resembled the aggregate of aEC2-6 as they were enriched with *Gata6*, *Vcam1*,

312 *Dcn*, *Mfap5*, *Sfrp1*, *Eln*, and *Cytl1* (Figure 4-figure supplement 1A and 1B). Taken together, these

313 information from three independent groups strongly suggest that a major source of heterogeneity

314 in the normal adult mouse aorta, as revealed by scRNA-seq analysis, includes differences between

315 LEC, vEC, aEC1 and aEC2-6.

316

15

Localization of heterogenous arterial EC populations

Among the arterial populations, aEC1 and aEC2 exhibited the highest frequencies of S1PR1/ß-arrestin coupling (> 90%). Thus, we addressed the anatomical location of these arterial clusters in the normal adult mouse aorta by immunolocalization of markers. We utilized antibodies against noggin (NOG), alkaline phosphatase (ALPL), and integrin alpha-6 (ITGA6), which are highly enriched in aEC1, as well as fibroblast-specific protein-1 (FSP1, encoded by *S100a4*) and claudin-5 (CLDN5), which are enriched in, but not exclusive to, aEC1 (Figure 5A). We also utilized antibodies against thrombospondin-1 (TSP1, encoded by *Thbs1*) and vascular cell adhesion molecule 1 (VCAM1), which are enriched in aEC2 and depleted in aEC1 (Figure 5A).

En face immunofluorescence staining showed that NOG and ITGA6 were expressed by GFP^high MAECs at intercostal branch points (Figure 5B and 5C). These GFP^high MAECs comprise the first 2-3 rows of cells around the circumference of branch orifices and include ~20-30 cells in total. In contrast, cells that are more than 2-3 cells away from branch point orifices did not express NOG or ITGA6 (Figure 5B and 5C). This was also seen for cytoplasmic staining of ALPL (Figure 5D). CLDN5 and FSP1 staining demarcate branch point MAECs but also exhibited heterogeneous staining of surrounding ECs (Figure 5E).

In contrast, TSP1 staining was exluded from ITGA6-expressing GFP^high MAECs at branch points (Figure 5F; see also Figure 5-figure supplement 1A). Rather, GFP^high MAECs located distally from the circumference of branch points expressed TSP1 in a patchy pattern (Figure 5G). We confirmed the endothelial nature of TSP1 immunoreactivity by staining sagittal sections of thoracic aortae (Figure 5-figure supplement 1B).

Similar to TSP1, VCAM1 staining was low at branch points, while surrounding cells showed heterogeneous levels of immunoreactivity in a somewhat asymmetric manner (Figure 5H).

16

340   We identified isolated GFP+ cells and patches of GFP+ cells distal from branch points with high

341   VCAM1 immunoreactivity (Figure 5-figure supplement 2A). As expected, intraperitoneal LPS

342   administration induced VCAM1 expression uniformly in aortic ECs (Figure 5-figure supplement

343   2B). These data suggest that the aEC1 population includes MAECs that are anatomically specific

344   to branch points, while the aEC2 population is located distally and heterogeneously from branch

345   points but nonetheless exhibits S1PR1/ß-arrestin signaling.

346

347   **Analysis of branch point-specific arterial ECs cluster aEC1**

348   Having identified the aEC1 cluster as including cells which demarcate thoracic branch

349   points orifices, we sought to characterize these unique cells in further detail. As shown in Figure

350   4A, aEC1-enriched transcripts are associated with a diverse range of signaling pathways, including

351   MAPK/GPCR, VEGF, and integrin signaling. Among aEC1-enriched transcripts, 16 were up-

352   regulated in *S1pr1-ECKO* MAECs, 5 were down-regulated (including *S1pr1*) and the remaining

353   390 were not differentially expressed (Figure 6A). The 16 *ECKO* up-regulated transcripts included

354   positive regulators of angiogenesis (*Pgf*, *Apold1*, *Itga6*, *Kdr*) (Mirza, Capozzi, Xu, McCullough,

355   & Liu, 2013; Olsson, Dimberg, Kreuger, & Claesson-Welsh, 2006; Primo et al., 2010), regulators

356   of GPCR signaling (*Rgs2*, *Rasgrp3*), and *Cx3cl1* (Fractalkine), which encodes a potent monocyte

357   chemoattractant (White & Greaves, 2012). We noted that several aEC1-enriched transcipts were

358   also expressed in LEC and vEC, but nonetheless were depleted from the remainder of arterial ECs

359   (aEC2-6) (Figure 6B). We examined the 25 transcripts most specific to aEC1 (log_2 [fold-change]

360   vs. all ECs > 4) and observed that 5 of these (*Dusp26*, *Eps8l2*, *Hapln1*, *Lrmp*, and *Rasd1*) showed

361   differential expression upon loss of S1PR1 function in MAECs (Figure 6C). Therefore, the

362   majority of transcripts specific to aEC1 do not appear to require S1PR1 signaling for normal levels

363 of expression. For example, protein levels of the aEC1 marker ITGA6 were not markedly affected

364 at branch point orifices in *S1pr1-ECKO* animals (Figure 6D). The ~2-fold increase in *Itga6*

365 transcript levels in *ECKO* MAECs may be due to expression in heterogeneous (non aEC-1)

366 populations, reflecting increases in LECs and/or aEC2-6. Nonetheless, these data suggest that

367 S1PR1 signaling is required for normal expression of some, but not the majority, of transcripts

368 enriched in aEC1 cells located at orifices of intercostal branch points.

369 We addressed whether circulatory S1P is required for S1PR1/ß-arrestin coupling in arterial

370 aortic endothelium by genetically deleting the two murine sphingosine kinase enzymes, *Sphk1* and

371 *Sphk2*. We generated S1PR1-GS mice harboring *Sphk1*$^{f/f}$ and *Sphk2*$^{-/-}$ alleles, bred this strain with

372 the tamoxifen-inducible *Rosa26-Cre-ER*^{T2} allele, and induced *Sphk1* deletion by tamoxifen

373 injection into adult mice (see Methods). Plasma S1P concentrations in Cre- animals were 631 ±

374 280 nM, whereas S1P was undetectable in plasma from Cre+ mice. Cre+ mice harbored ~7-fold

375 fewer non-branch point GFP+ ECs relative to Cre- mice (Figure 6E and 6F). In contrast, the

376 number of branch point GFP+ EC was not significantly different between Cre+ and Cre- animals,

377 suggesting that S1PR1/ß-arrestin coupling (GFP expression) in branch point aEC1 cells is largely

378 independent of S1P-mediated activation of S1PR1 (Figure 6E and 6F). Furthermore, ITGA6

379 expression at branch point orifices was unaltered in Cre+ mice and therefore is independent of

380 circulatory S1P. Taken together, these data suggest that the unique transcriptome of aEC1 cells is

381 largely independent of S1P/S1PR1 signaling.

382 For insight into unique regulators of transcription in aEC1 cells, we identified all TFs

383 enriched and depleted in this cluster (Figure 7-figure supplement 1A; see also Suplementary File

384 5). Among arterial ECs, TFs highly enriched (Z-score > 7) in aEC1 are *Hey1*, *Nr4a2* (NURR1),

385 *Nr4a1* (NUR77), *Sox17*, *Ebf1*, and *Bcl6b* (Figure 7A and Figure 7-figure supplement 1A and 1B).

386   *Lef1* transcripts were detected at significant levels only in aEC1 cells (Figure 7-figure supplement

387   1A and 1B). Transcripts encoding other TFs, such as *Tcf4*, *Ets1*, *Sox18*, *Epas1*, *Mef2c*, and *Tox2*,

388   were aEC1-enriched (Z-score > 3 and < 7) but more heterogeneously distributed in other arterial

389   clusters (Figure 7A and Figure 7-figure supplement 1A). These data are consistent with our ATAC-

390   seq analysis, which showed over-represntation of SOX17, TCF4, and NUR77 motifs in chromatin

391   specifically open in GFP^{high} MAECs. In contrast, *Gata6* (ubiquitous among aEC2-6) and *Gata3*

392   (heterogeneous among aEC2-6) were both depleted from aEC1 (Figure 7A and Figure 7-figure

393   supplement 1A and 1B).

394   Immunostaining of thoracic aorta *en face* preparations for LEF1 showed nuclear

395   immunoreactivity in GFP^{high} ECs at branch point orifices but not in adjacent ECs (Figure 7B). We

396   noted that all LEF1+ cells also exhibited ITGA6 expression, confirming these two proteins as

397   markers of aEC1 cells at branch point orifices (Figure 7B). These data suggest involvement of

398   LEF1, a downstream TF of Wnt/ß-catenin signaling, in regulating gene expression in aEC1 cells.

399   We further explored roles for LEF1, SOX17, NUR77, and GATA6 in aEC1 gene

400   expression by examining binding sites for these factors near genes encoding aEC1-enriched

401   transcripts. A prominent GFP^{high}-specific peak in the first intron of *Itga6* harbored a LEF1 motif

402   (Figure 7C). In addition, a GFP^{high}-enriched peak ~115 kb upstream of the transcription start site

403   (TSS) harbored a SOX17 motif. Similarly, we identified bindings sites for SOX17 and NUR77 in

404   GFP^{high}-specific peaks upstream of the *Nog* gene (Figure 7C). Each of these putative enhancers

405   lacked GATA6 motifs. In contrast, the *Frzb* and *Pcolce2* genes, which encode aEC4-enriched

406   transcripts and were up-regulated in GFP^{low} MAECs (Figure 1-figure supplement 1B), harbored

407   intronic GFP^{low} MAEC-specific peaks with GATA6 binding sites (Figure 7-figure supplement

408   2A).

409   For broader insight into TF activity near aEC1 genes, we extracted all GFP^{high} and GFP^{low}

410   merged peaks that intersected a 100 kb window centered on the TSSs of all aEC1-enriched (Z-

411   score > 3) and -depleted (Z-score < -3) genes. HOMER analysis of these peaks showed enrichment

412   of SOX17, "Ets1-distal", MEF2C, and NUR77 motifs near the aEC1-enriched genes (Figure 7-

413   figure supplement 1C). In contrast, GATA motifs (GATA2, GATA3, GATA6), as well as the

414   NKX2.2 motif, were enriched near aEC1-depleted genes (Figure 7-figure supplement 1C).

415   Collectively, these data suggest roles for specific transcription factors, such as LEF1, SOX17,

416   NUR77, and GATA6, in mediating transcriptional events which distinguish aEC1 from the

417   remainder of aortic arterial ECs.

418   Examination of postnatal day 6 (P6) S1PR1-GS aortae showed that MAECs at branch point

419   orifices expressed GFP and ITGA6 in a manner similar to adult S1PR1-GS mice (Figure 7D). We

420   observed that non-branch point GFP+ EC were less frequent in P6 mice, suggesting that

421   heterogeneity among non-branch point ECs changes over time. Indeed, this hypothesis is

422   consistent with McDonald et al. (2019), who reported that aEC3 marker transcripts (e.g. *Atf3*) are

423   absent in aged mice (McDonald et al., 2018). Taken together, these data suggest that aEC2-like

424   (GFP^{high}) cells occur at greater frequency as aEC3-like cells disappear over time in the intima of

425   the murine aorta. Furthermore, these P6 data strongly suggest that the GFP^{high} status of MAECs at

426   branch point orifices, as well as their unique gene expression program, is not dynamic throughout

427   postnatal life. Rather, the gene expression specification of these cells likely occurs during

428   development in tandem with epigenetic changes (i.e. chromatin accessibility) and is stable

429   throughout adulthood.

430   Together, these findings characterize the postnatal, aortic branch point-specific arterial EC

431   subpopulation designated aEC1. These cells have a unique anatomical location and exhibit high

20

432   S1PR1/ß-arrestin coupling. The transcriptome of this EC subpopulation does not appear to be

433   directly regulated by S1PR1 signaling. Rather, a combination of TFs, such as NUR77, NURR1,

434   SOX17, HEY1, and LEF1, may regulate cluster-defining transcripts in these cells.

435

436   **S1PR1 signaling in adventital lymphatic ECs regulates immune and inflammatory gene**

437   **expression**

438   To locate aorta-associated LEC with high frequency (97%) of S1PR1/ß-arrestin coupling,

439   we utilized antibodies against LYVE1 and VEGFR3 (*Flt4*). LYVE1 marks most but not all LEC

440   subtypes and VEGFR3 is a pan-LEC marker (Wang et al., 2017). Sagittal sections of the S1PR1-

441   GS mouse thoracic aorta revealed that a subset of adventitial LYVE1+ LECs are positive for

442   S1PR1/ß-arrestin coupling (Figure 8A).

443   Next, we prepared whole mounts of thoracic aortae and collected confocal Z-stacks of only

444   the adventitial layer (Figures 8B and 8C). We observed three distinct expression patterns:

445   VEGFR3+LYVE1+GFP+ (orange stars), VEGFR+LYVE1^{low}GFP+ (cyan stars), and

446   VEGFR3+LYVE1+GFP- (magenta stars). We noted that the VEGFR3+LYVE1+GFP- areas were

447   associated with blind-ended, bulbous structures. In addition to expression in aEC1, *Itga6*

448   transcripts were detected in vEC and LEC populations (Figure 8-figure supplement 1A).

449   Consistently, we observed GFP+ITGA6+LYVE1+ LEC on the adventitial side of the aorta, in

450   proximity to a GFP+ITGA6+LYVE1- arterial branch point (Figure 8-figure supplement 1B).

451   We examined the role of LEC-derived S1P in LEC S1PR1/ß-arrestin coupling by

452   generating S1PR1-GS mice deficient in lymph S1P (*S1pr1*$^{ki/+}$:*Sphk1*$^{f/f}$:*Sphk2*$^{-/-}$:*Lyve1-Cre*$^{+}$)

453   (Pham et al., 2010). LECs were identified in mesenteric vessels by immunostaining for the LEC-

454   specific transcription factor prospero homeobox protein 1 (PROX1). Similar to our observations

21

455   in the aorta, GFP+PROX1+ cells were heterogeneous, with some PROX1+ structures showing

456   high levels of GFP expression and others showing little to none (Figure 8D). Nonetheless, we

457   observed a significant decrease in the frequency of PROX1+GFP+ LECs in Cre+ mice (Figure 8D

458   and 8E), demonstrating that LEC-derived S1P is required for S1PR1/ß-arrestin coupling in LECs.

459   These data are consistent with abundant LEC expression of the S1P transporter *Spns2* (Figure 3-

460   figure supplement 4A), which is also required for normal levels of lymph S1P (Simmons et al.,

461   2019). Taken together, scRNA-seq analysis of aortic ECs identified two anatomically distinct

462   arterial EC populations (branch point and non-branch point), as well as a subset of adventital LECs,

463   each of which shows high S1PR1/ß-arrestin coupling.

464   For insight into S1PR1-mediated gene expression in aorta-associated LECs, we divided

465   *S1pr1-ECKO* upregulated genes (Figure 1C and Figure 1-figure supplement 1D) according to their

466   cluster assignments from scRNA-seq analysis. 48% of upregulated genes were enriched in the

467   LEC cluster (Z-score > 3 versus the remainder of ECs), while only 7% were enriched in vEC

468   and/or aEC1-6 (Figure 9A and Suplementary File 6). None of the *S1pr1-ECKO* downregulated

469   transcripts were enriched in the LEC cluster. A heatmap of the 78 LEC transcripts up-regulated in

470   *S1pr1-ECKO* MAECs is shown in Figure 9B. Among these were chemokine/cytokine pathway

471   genes (*Irf8, Lbp, Il7, Il33 Ccl21, Tnfaip8l1*) as well as lymphangiogenesis-associated genes (*Kdr,*

472   *Prox1, Lyve1, Nr2f2*) (Figure 9B and Figure 9-figure supplement 1A). This suggests that loss of

473   S1PR1 signaling in LECs alters transcriptional programs associated with lymphangiogenesis and

474   inflammation/immunity.

475   Lymphatic vessels associated with the aorta and large arteries, although not well studied,

476   are thought to be involved in key physiological and pathological processes in vascular and immune

477   systems (Csanyi & Singla, 2019; Galkina & Ley, 2009). For example, LEC expression of CCL21

22

478   mediates dendritic cell recruitment to lymphatic vessels during homeostasis and pathological

479   conditions (Vaahtomeri et al., 2017). This chemokine was abundantly expressed in the LEC cluster

480   (Figure 8-figure supplement 1A) and was upregulated by S1PR1 loss-of-function (Figure 9B and

481   Figure 9-figure supplement 1A). Whole mount staining of S1PR1-GS mice thoracic aortae for

482   LYVE1 and CCL21 revealed aorta-associated CCL21+ lymphatics with high levels of S1PR1/ß-

483   arrestin coupling (Figures 9C and 9D). We noted that CCL21 protein appeared as peri-nuclear

484   puncta that likely marks the *trans*-Golgi network, as observed in dermal LECs (Vaahtomeri et al.,

485   2017). Sagittal sections of the thoracic aorta indicate that GFP^{high}, LYVE1^{+} adventitial lymphatics

486   express CCL21 protein (Figure 9D), suggesting that ß-arrestin-dependent downregulation of

487   S1PR1 correlates with CCL21 expression (Figure 9D).

488   These studies show that S1PR1/ß-arrestin coupling in a subset of adventitial lymphatics

489   correlates with S1PR1-mediated attenuation of lymphagiogenic/inflammatory gene expression.

490   We observed that the fraction of PDPN^{+} LECs was not altered between *S1pr1-ECKO* and *WT* aorta

491   tissues (Figure 9–figure supplement 1B), indicating that there is not widespread lymphagiogenesis

492   or LEC proliferation. However, analysis of *Flt4* vs *Pdpn* expression and *Ccl21a* vs *Pdpn*

493   expression showed that there are LECs that express *Flt4* and *Ccl21a* but not *Pdpn* (Figure 9-figure

494   supplement 2). Therefore, it is possible that *S1pr1-ECKO* leads to expansion of a PDPN^{low}

495   population in the adventitia. Nonetheless, these data indicate that S1PR1 mediates gene expression

496   in adventitial lymphatics of the homeostatic adult mouse aorta.

497

Discussion

499

500   Intracellular signaling through G protein- and ß-arrestin-dependent pathways is tightly

501   regulated at the levels of GPCR expression and ligand availability. Endothelium of major organs,

23

502   such as brain, lung, skeletal muscle, and the aorta, express unique sets of GPCRs with only 5

503   receptors commonly expressed, one of which is *S1pr1* (Kaur et al., 2017). Despite ubiquitoius

504   endothelial *S1pr1* expression (Galvani et al., 2015), receptor activation *in vivo*, as reported by GFP

505   in S1PR1-GS mice, revealed heterogeneous signaling in multiple organs (Kono et al., 2014). Here,

506   we describe high frequency of aortic GFP+ (i.e. S1PR1/ß-arrestin coupling) EC around intercostal

507   branch point orifices and heterogeneous GFP+ EC throughout the remainder of intimal aortic

508   endothelium. We and others have shown that endothelial ablation of *S1pr1* (*S1pr1-ECKO*) or

509   reduction of circulatory S1P disrupts endothelial barriers (Camerer et al., 2009; Christensen et al.,

510   2016; Christoffersen et al., 2011; Oo et al., 2011; Yanagida et al., 2017). Furthermore, the

511   descending aorta of *S1pr1-ECKO* mice displayed exacerbated plaque formation in the *Apoe*$^{-/-}$

512   Western diet (WD)-induced atherosclerosis model (Galvani et al., 2015). However, we lack

513   information regarding EC transcriptional responses that correlate with or are directly downstream

514   of S1PR1 signaling. Here, we profiled the transcriptomes and open chromatin landscapes of aortic

515   ECs with high (GFP^{high}) or low (GFP^{low}) levels of S1PR1/ß-arrestin coupling, as well as *S1pr1-*

516   *ECKO* aortic ECs.

517   *S1pr1-ECKO* MAECs upregulated transcripts in TNFα/cytokine signaling pathways and

518   exhibited enhanced chromatin accessibility at NFκB binding sites. Concomitantly, glucocorticoid

519   receptor pathway was suppressed. These mRNA and chromatin signatures were shared between

520   *S1pr1-ECKO* and GFP^{high} MAECs, suggesting that persistent ß-arrestin recruitment to S1PR1 can

521   result in down-regulation of membrane-localized S1PR1 and a subsequent loss-of-function

522   phenotype. There were many (2,145) DEGs between GFP^{high} and GFP^{low} MAECs, but relatively

523   few (365) between *ECKO* and *WT* MAECs, which suggested that the GFP^{high} and/or GFP^{low}

524   populations reported aortic EC subtypes in addition to S1PR1-regulated transcripts. Indeed,

24

525   chromatin regions uniquely open in GFP^{high} MAECs were enriched with binding sites for TFs that

526   have well-defined but divergent roles in endothelial cells, such as SOX17 (arterial) (Corada et al.,

527   2013; Zhou, Williams, Smallwood, & Nathans, 2015) and COUP-TFII (venous/lymphatic)

528   (Lindskog et al., 2014). Nonetheless, we present the first collection of putative regulatory regions

529   from freshly isolated mouse aortic ECs, which is a critical dataset for future studies of individual

530   enhancer functionalities.

531   Our scRNA-seq analysis addressed with high resolution the heterogeneity among MAECs.

532   We identified 6 arterial EC clusters (aEC1-6), 1 lymphatic EC cluster (LEC) and 1 venous EC

533   cluster (vEC). Immunohistochemical analyses revealed LEC cells as including lymphatic

534   structures of the aortic adventita, aEC1 cells as circumscribing intercostal branch point orifices,

535   and aEC2 cells as heterogeneously dispersed throughout intimal endothelium. Each of these

536   clusters harbored high frequency (> 90%) of GFP^{high} EC. We also described aEC3 cells, which

537   contained comparatively few (< 60%) GFP^{high} ECs. aEC3 cells strongly resembled an *Atf3*-positive

538   cluster reported by Mcdonald et al. (2018) that mediates endothelial regeneration (McDonald et

539   al., 2018). Considering that *Atf3*-positive ECs were absent in old (18-month) mice (McDonald et

540   al., 2018), we hypothesize that aEC3-like cells disappear over time while aEC2-like cells increase

541   in frequency in the aorta intima. This notion is supported by the higher frequency of non-branch

542   point GFP^{high} intimal ECs in adult mice relative to P6 pups.

543   Concordant with findings from two recent aorta scRNA-seq studies (Kalluri et al., 2019;

544   Lukowski et al., 2019), our clustering segregated vEC, LEC, and aEC1 from aEC2-6. We suspect

545   that use of S1PR1-GS mice facilitated deconvolution of LEC and vEC from the distinct aEC1

546   population. Despite their proximity to intercostal branch points, aEC1 cells do not exhibit a

547   transcriptomic signature prototypical of inflammation, as might be expected (Chiu & Chien, 2011).

25

548   Furthermore, high levels of S1PR1/ß-arrestin coupling and expression of unique genes (e.g. *Itga6*)

549   in aEC1 cells are independent of both circulatory S1P and age in postnatal mice. To further explore

550   temporal regulation of cluster-specific genes, we examined scRNA-seq of FACS-sorted

551   VEGFR2^{high} cells from E8.25 embryos (Pijuan-Sala et al., 2019). These embryonic cells exhibited

552   expression of aEC1-enriched transcripts (*Lef1*, *Itga6*, *Rasgrp3*, *Alpl*, *Hey1*, *Flt1*, *Igf2*), but

553   depletion of aEC2-6-enriched transcripts (*Thbs1*, *Sod3*, *Vcam1*, *Sfrp1*, *Ace*, *Bmp6*, *Dcn*). This

554   suggests that aEC1 cells are more characteristic of embryonic EC than are the majority of intimal

555   ECs. Similarly, vEC/LEC-specific transcripts (*Prox1*, *Nr2f2*, *Kdr*) were also expressed in these

556   embryonic cells. Thus, transcriptomic similarities between aEC1 and LEC/vEC in the adult aorta

557   may be retained from development, perhaps through epigenetic modifications common between

558   these cell types. It is also possible that the unique anatomical location of aEC1 (at the

559   circumferential ridge at aortic branch point) may promote a distinct EC phenotype either because

560   of spatial positioning or environmental factors.

561   *S1pr1-ECKO* and *S1pr1$^{-/-}$* animals display an aortic hyper-branching phenotype between

562   E11.5 and E13.5 that is incompatible with life after E14.5 (Gaengel et al., 2012). Therefore, S1PR1

563   is required for normal embryonic branching morphogenesis. Consistently, E9.5-E10.5 S1PR1-GS

564   embryos show high GFP expression (S1PR1/ß-arrestin coupling) throughout the dorsal aorta

565   (Kono et al., 2014). This contrasts with the adult aortae, wherein the highest levels of S1PR1/ß-

566   arrestin coupling are concentrated around the orifices of intercostal branch points. These findings

567   further suggest that that the unique gene expression program of aEC1 cells is established during

568   morphogenesis of intercostal arteries during development.

569   The extent to which aEC1 cells at branch point orifices are functionally distinct remains to

570   be determined. Identification of ITGA6 as a marker of this population will facilitate future studies.

26

571 For example, combinations of pan-EC, LEC, and ITGA6 antibodies can be used to purify or enrich

572 this population in developmental or disease models (e.g. atherosclerosis). Moreover, *cis*-elements

573 proximal to aEC1-specific genes can be applied to the "Dre-rox/Cre-loxP" system (Pu et al., 2018)

574 to specifically manipulate gene expression in aEC1 cells.

575   Non-branch point (i.e. aEC2) cells required circulatory S1P for normal levels of S1PR1/ß-

576 arrestin coupling. Similarly, mesenteric LECs required S1P in lymph for normal levels of S1pr1/ß-

577 arrestin coupling. Notably, we did not detect *S1pr1-ECKO* down-regulated transcripts in aEC2 or

578 LEC clusters, but we did detect 4 such transcripts in aEC1 cells, which were *Dusp26*, *Enah*,

579 *Eps8l2*, and *Hapln1*. Among the clusters identified in this study, LEC-enriched transcripts were

580 affected the most upon EC ablation of *S1pr1*. This suggests that loss of S1P/S1PR1 signaling either

581 alters cell-intrisic phenotypes of peri-aortic LECs or induces expansion of one or multiple LEC

582 subtypes.

583   There is accumulating direct and indirect evidence for key roles of adventital lymphatics

584 in atherogenesis (Csanyi & Singla, 2019; Maiellaro & Taylor, 2007). For example, auto-antibodies

585 against oxidized LDL (OxLDL) inhibit macrophage OxLDL uptake and mitigate atherosclerosis

586 (Shaw et al., 2000). This implies that antigen presenting cells (APCs) phagocytose OxLDL

587 epitopes, then travel via adventitial lymphatics to lymphoid organs (e.g. lymph nodes) and present

588 OxLDL antigens to B cells. Murine atherosclerotic lesions were found to harbor "atypical,

589 lymphatic-like" capillaries that were VEGFR3+ but LYVE1- (Taher et al., 2016), which is

590 consistent with our observations of adventitial LEC heterogeneity. Considering the critical role of

591 lymphatic EC-derived CCL21 in regulating the trafficking of APCs (Vaahtomeri et al., 2017), and

592 perhaps other adaptive immune cells, there is an impetus to determine the extent to which adventital

593 lymphatics are a viable target for atherosclerosis therapy.

594   While there is scant information about the roles of S1P/S1PR1 signaling in adult lymphatic

595   vasculature, our findings lay a groundwork for future studies of S1PR1-mediated LEC phenotype

596   regulation in homeostatic processes and inflammatatory/ autoimmune diseases. A recent study

597   found that lymph-derived S1P facilitates CCL21 deposition in high endothelial venules and

598   dendritic cell recruitment (Simmons et al., 2019). While *S1pr1-ECKO* animals exhibit exacerbated

599   atherosclerosis (Galvani et al., 2015), we cannot discern whether this was due to phenotypes of

600   lymphatic ECs, arterial ECs, or both cell types. Future studies should use artery- and lymphatic-

601   specific Cre-drivers to distinguish between the roles of S1PR1 in different types of vasculature.

602   Such mechanistic studies will help to determine the utility of S1PR1 modulators in treating

603   lymphatic-mediated vasculopathies.

604

Methods

Mice

607   Animal experiment protocols were approved by the Institutional Animal Care and Use

608   Committees (IACUC) of Boston Children's Hospital and the French Department of Eduction.

609   S1PR1-GS mice were previously reported (Kono et al., 2014). S1PR1-GS mice used for

610   experiments harbored a single *S1pr1^{knockin}* (*S1pr1-tTA-IRES-mArrb2-TEV*) allele (*S1pr1*$^{ki/+}$) as well

611   as a single *H2B-GFP* reporter allele. *S1pr1*$^{f/f}$ mice (Allende, Yamashita, & Proia, 2003) were bred

612   with *Cdh5-Cre*^{ERT2} mice (Sorensen, Adams, & Gossler, 2009) to generate *S1pr1-ECKO* mice, as

613   previously described (Galvani et al., 2015) (Jung et al., 2012). Gene deletion was achieved by

614   intraperitoneal injection of tamoxifen (2 mg/day) at 5-6 weeks of age for five consecutive days.

615   Tamoxifen treated mice were rested for a minimum of 2 weeks prior to experiments.

616   S1PR1-GS mice deficient in LEC S1P production were generated by excising a conditional

617   knockout allele for *Sphk1* in an *Sphk2* knockout background with *Lyve1-Cre*

618   (*S1pr1*$^{ki/+}$:*Sphk1*$^{f/f}$:*Sphk2*$^{-/-}$:*Lyve1-Cre*$^+$) essentially as described by Cyster and colleagues (Pham

619   et al., 2010) and excision efficiency confirmed by the induction of lymphopenia. S1PR1-GS mice

620   deficient in plasma S1P (S1PR1-GS-S1P-less) were generated by crossing S1PR1-GS mice with

621   *Sphk1*$^{f/f}$:*Sphk2*$^{-/-}$:*Rosa26-Cre-ER*^{T2} mice to obtain *S1pr1*$^{ki/+}$:*GFP*$^+$:*Sphk1*$^{f/f}$:*Sphk2*$^{-/-}$:*Rosa26-Cre-*

622   *ER*$^{T2+}$ mice (the *Rosa26-Cre-ER*^{T2} allele is described in (Takeda, Cowan, & Fong, 2007)).

623   Tamoxifen was administered to S1PR1-GS-S1P-less mice and Cre- littermate controls as described

624   above. Experiments were performed between 23 and 25 weeks after the final tamoxifen dose.

625   Adult (aged 8 to 12 weeks) males and females were used for sequencing experiments.

626   Males and females of similar age (7 to 18 weeks) were used for imaging studies, unless indicated

627   otherwise. For examination of VCAM1 (Figure 5-figure supplement 2B), 200 μL

628   lipopolysaccharide (Sigma, L2630) in PBS was injected i.p. (5.5 mg/kg) for nine hours followed

629   by euthanasia and tissue harvest.

630

FACS isolation and single cell sequencing of mouse aortic endothelial cells

632   After CO_2 euthanasia, the right atrium was opened and the left ventricle was perfused with

633   10 mL phosphate-buffered saline (PBS) (Corning). Aortae were dissected from the root to below

634   the common iliac bifurcation and transferred into ice ice-cold 1x HBSS (Sigma, H1641). Whole

635   aortae were incubated in HBSS containing elastase (4.6 U/mL, LS002292, Worthington), dispase

636   II (1.3 U/mL, Roche), and hyaluronidase (50.5 U/mL, Sigma, H3506) at 37˚C for 10 minutes in

637   wells of a 6-well plate. Aortae were then transferred to a 100 mm dish with 1 mL HBSS and minced

638   using small scissors. Minced aortae were transferred to a low protein binding 5 mL tube containing

639   Liberase (0.6 U/mL, Sigma), collagenase II (86.7 U/mL, LS004174, Worthington), and DNase

640   (62.0 U/mL, Sigma, D4527) in 4.3 mL HBSS and incubated at 37˚C for 40 minutes with rotation

641   in a hybridization oven. The cell suspension was then triturated 10 times through an 18 G needle

642   to dissociate clumps, followed by addition of 400 µL STOP solution (3 mM EDTA, 0.5% fatty

643   acid-free bovin serum albumin (FAF-BSA) (Sigma, A6003) in 1x HBSS). For the remainder of

644   the procedure, cells were kept on ice and all centrifugation steps were performed at 4˚C.

645   Cells were spun at 500 xg for 5 minutes, the supernatant was removed, then cells were

646   washed with 4 mL STOP solution and spun at 500 xg for 5 minutes. The supernatant was removed,

647   then cells were washed with 4 mL blocking solution (0.25% FAF-BSA in HBSS) and filtered

648   through FACS tubes with filter caps (Falcon). After centrifugation and supernatant removal, cells

649   were stained with phycoerythrin (PE)-conjugated anti-mouse CD31 (MEC13.3, Biolegend, San

650   Diego, CA), allophycocyanin (APC)-conjugated anti-mouse CD45 (30-F11, Biolegend) and APC-

651   conjugated TER119 (Biolegend, 116212) antibodies in blocking solution with anti-CD16/32 (2.5

652   µg/mL) for 45 minutes on ice. DAPI (0.7 µM) was added for the final 5 minutes of staining to

653   exclude dead cells. Aortic cells were washed with 4.5 mL FACS buffer (0.25% FAF-BSA in PBS)

654   before sorting for selection of CD31$^+$/CD45$^-$/TER119$^-$/GFP^{high} and CD31$^+$/CD45$^-$/TER119$^-$

655   /GFP^{low} cells using BD FACSAria^{TM} II (BD Bioscience) (see Figure 1B). Cells from *S1pr1*-WT

656   and -*ECKO* mice were sorted using the GFP^{low} gate (see Figure 1-figure supplement 1A) because

657   it includes MAECs from mice genetically negative for the *H2B-GFP* reporter allele and stained

658   with the same antibody panel. Cells from 2-4 aortae of age and sex-matched adult mice were

659   pooled for each individual experiment (ATAC-seq, RNA-seq and scRNA-seq). Cells were sorted

660   into either 0.1% FAF-BSA/PBS or buffer RLT (Qiagen) supplemented with β-mercaptoethanol

661   for ATAC-seq and RNA-seq, respectively.

662   For single-cell RNA-seq, GFP[high] and GFP^{low} cells were gated as described above. Library

663 preparation from single cells was performed as previously described (Vanlandewijck et al., 2018).

664 Briefly, cells were deposited into individual wells of 384-well plates containing 2.3 µL of lysis

665 buffer (0.2% Triton-X (Sigma, T9284), 2U/µL RNase inhibitor (ClonTech, 2313B), 2 mM dNTP's

666 (ThermoFisher Scientific, R1122), 1 µM Smart-dT30VN (Sigma), ERCC $1{:}4 \times 10^{7}$ dilution

667 (Ambion, # 4456740)) prior to library preparation using the Smart-seq2 protocol (Picelli et al.,

668 2014).

669

670 **Bulk RNA-seq and analysis**

671   Cells sorted into buffer RLT were subjected to total RNA extraction using the RNeasy

672 Micro Kit (Qiagen). The High Sensitivity RNA ScreenTape (Agilent) was used to verify RNA

673 quality before synthesis of double-stranded cDNA from 5-10 ng RNA using the SMART-Seq2 v4

674 Ultra Low RNA Kit for Sequencing (Takara) according to the manufacturer's instructions. Agilent

675 2100 Bioanalyzer and High Sensitivity DNA Kit (Agilent) were used to verify cDNA quality.

676 cDNA libraries were prepared for sequencing using the Illumina Nextera XT2 kit (Illumina), and

677 ~20-40 million paired-end reads (2 x 75 bp) were sequenced for each sample.

678   Reads from each sample were aligned to the MGSCv37 (mm9) genome assembly using

679 STAR (Dobin et al., 2013) with the options: --runMode alignReads --outFilterType BySJout --

680 outFilterMultimapNmax 20 --alignSJoverhangMin 8 --alignSJDBoverhangMin 1 --

681 outFilterMismatchNmax 999 --alignIntronMin 10 --alignIntronMax 1000000 --

682 alignMatesGapMax 1000000 --outSAMtype BAM SortedByCoordinate --quantMode

683 TranscriptomeSAM. Gene-level counts over UCSC annotated exons were calculated using the

684 Rsubread package and "featureCounts" script (Liao, Smyth, & Shi, 2013) with options: -M –O –p

685 –d 30 –D 50000. The resultant count table was input to edgeR (M. D. Robinson, McCarthy, &

686 Smyth, 2010) for differential gene expression analysis. The .bam files from STAR were input to

687 the RSEM (B. Li & Dewey, 2011) script "rsem-calculate-expression" with default parameters to

688 generate FPKMs for each replicate.

689

690 **ATAC-seq analysis**

691 ATAC-seq libraries were prepared according to the previously described fast-ATAC

692 protocol (Corces et al., 2016). Briefly, 800-4,000 FACS-isolated cells in 0.1% FAF-BSA/PBS

693 were pelleted by centrifugation at $400 \times g$ at 4°C for 5 min. Supernatant was carefully removed to

694 leave the cell pellet undisturbed, then cells were washed once with 1 mL ice-cold PBS. The

695 transposition mix [25 μL buffer TD, 2.5 μL TDE1 (both from Illumina FC-121-1030), 1 μL of

696 0.5% digitonin (Promega, G9441) and 16 μl nuclease-free water] was prepared and mixed by

697 pipetting, then added to the cell pellet. Pellets were disrupted by gently flicking the tubes, followed

698 by incubation at 37°C for 30 minutes in an Eppendorf ThermoMixer with constant agitation at 300

699 rpm. Tagmented DNA was purified using the MinElute Reaction Cleanup Kit (Qiagen, 28204),

700 and subjected to cycle-limiting PCR as previously described (Buenrostro et al., 2013). Transposed

701 fragments were purified using the MinElute PCR Purification Kit (Qiagen, 28004) and Agilent

702 DNA Tapestation D1000 High Sensitivity chips (Agilent) were used to quantify libraries. ~20-60

703 million paired-end reads (2 x 75 bp) were sequenced for each sample on a NextSeq instrument

704 (Illumina).

705 Read alignment to the MGSCv37 (mm9) genome assembly was performed with bowtie2

706 (Langmead & Salzberg, 2012) and the options: --very-sensitive –X 2000 –no-mixed –no-

707 discordant. Duplicated fragments were removed using the Picard "MarkDuplicates" script with the

32

708 options: Remove_Duplicates=true Validation_stringency=lenient

709 (http://broadinstitute.github.io/picard/).

710 Paired-end reads were separated, centered on Tn5 cut sites, and trimmed to 10 bp using a

711 custom in-house script. Peaks were called using the MACS2 "callpeak" script (Zhang et al., 2008)

712 with options: -B –keep-dup all –nomodel –nolambda –shift -75 –extsize 150. Reads mapping to

713 murine blacklisted regions and mitochondrial DNA were masked out of peak lists using the

714 Bedtools "intersect -v" script (Quinlan & Hall, 2010).

715 Replicates from each biological group were merged using the bedops "merge" script to

716 generate one high-confidence peak set for each of the four biological groups (GFP^{high}, GFP^{low},

717 *S1pr1-ECKO*, *S1pr1-WT*) (Neph et al., 2012). These four peak sets were then merged to generate

718 a merged, consensus peak set of 123,473 peaks. For each replicate, reads covering consensus peak

719 intervals were counted using the Bedtools "coverage" script with the "-counts" option (Quinlan &

720 Hall, 2010). The resultant count table was input to edgeR (M. D. Robinson et al., 2010) to

721 determine differentially accessible peaks (DAPs).

722 DAPs were used as input for the HOMER "findMotifsGenome.pl" script with the option

723 "-size given" to identify motifs enriched in peaks with enhanced accessibility in either GFP^{high},

724 GFP^{low}, *S1pr1-ECKO*, or *S1pr1-WT* MAECs (Heinz et al., 2010).

725 Nucleotide-resolution coverage (bigwig) tracks were generated by first combining trimmed

726 reads from each replicate, then inputting the resultant .bam files to the DeepTools (Ramirez et al.,

727 2016) "bamCoverage" script with options "—normalizeUsing RPGC –binSize 1". Heatmaps of

728 ATAC-seq reads within 600 bp of p65, NUR77, COUP-TFII, ATF1, GATA2, and GRE motifs

729 were generated by centering coverage tracks on each motif identified in DAPs. These motifs were

730 identified using the HOMER script "annotatePeaks.pl" with the "-m -mbed" options. All heatmaps

33

731   were generated using DeepTools and all genome browser images were captured using Integrative

732   Genomics Viewer (J. T. Robinson et al., 2011).

733

734   **scRNA-seq analysis**

735   1152 Fastq files (one per cell) were aligned to the GRCm38 (mm10) genome assembly

736   using STAR with options –runThreadN 4 –outSAMstrandField intronMotif –twopassmode Basic.

737   Bam files were input to the velocyto (http://velocyto.org/velocyto.py/) command-line script "run-

738   smartseq2" (La Manno et al., 2018). Expressed repetitive elments were downloaded from the

739   UCSC genome browser and masked from analysis using the "-m" option of the "run-smartseq2"

740   script. The resultant table of read counts per transcript ("loom" file) was input to the PAGODA2

741   (https://github.com/hms-dbmi/pagoda2) R package for further analysis (Fan et al., 2016; La

742   Manno et al., 2018). The details of our R code are provided in Supplementary File 9.

743   After variance normalization, the top 3000 overdispersed genes were used for principal

744   component analysis (PCA). An approximate k-nearest neighbor graph (k = 30) based on a costine

745   distance of the top 100 principal components was used for clustering. Cluster were determined

746   using the multilevel community detection algorithm. PCA results were plotted using the "tSNE"

747   embedding option of the PAGODA2 "r$getEmbedding" function. Heatmaps of gene expression

748   embedded on hierarchical clustering, differential expression analyses, and expression of individual

749   transcripts on the tSNE embedding were generated using the graphical user interface at

750   http://pklab.med.harvard.edu/nikolas/pagoda2/frontend/current/pagodaLocal/. We generated the

751   binary (.bin) file according to the Pagoda2 walkthrough: https://github.com/hms-

752   dbmi/pagoda2/blob/master/vignettes/pagoda2.walkthrough.oct2018.md. This binary file

753   (Supplementary File 7) can be uploaded to the graphical user interface for exploration of our

754   dataset. We generated a file of cluster labels (for LEC, vEC, VSMC, aEC1, aEC2, aEC3, aEC4,

755   aEC5, aEC6 as well as all other cluster grouping used for analysis), which can also be uploaded to

756   the graphical user interface for visualization of these clusters (Supplementary File 8).

757

758   **Immunohistochemistry**

759   Mice were euthanized as described above, then perfused through the left ventricle with 5

760   mL PBS immediately followed by 10 mL ice-fold 4% paraformaldehyde (PFA) in PBS. The left

761   ventricle was then perfused with 6 mL PBS. After aorta dissection, remaining fat tissue was

762   removed with the aorta suspended in PBS in a polystyrene dish. For sectioning, intact thoracic

763   aortae were additionally post-fixed in 4% PFA for 10 minutes, then briefly washed with PBS three

764   times. Aortae were then cryoprotected in 30% sucrose in PBS for 2 hours at 4° C, embedded in a

765   1:1 mixture of 30% sucrose PBS:OCT over dry ice, then sectioned at 14 µM intervals using a

766   cryostat (Leica Biosystems).

767   For *en face* preparations, fine scissors were used to cut the aorta open and expose the

768   endothelium for downstream flat-mount preparation. Aortae were placed into 24-well tissue

769   culture plates and permeabilized in 0.5% Triton X-100/PBS (PBS-T) for 30 minutes on a room-

770   temperature orbital shaker, then blocked in blocking solution (1% BSA (Fisher Scientific,

771   BP1605), 0.5% Donkey Serum (Sigma, D9663) in PBS-T for 1 hour. Primary antibody incubations

772   were carried out overnight in blocking solution, followed by detection with secondary antibodies.

773   Primary antibodies used were goat anti-VE-cadherin (1:300, R&D systems, AF1002), rabbit anti-

774   LYVE1 (1:300, 103-PA50AG, ReliaTech), goat anti-LYVE1 (1:300 , R&D systems, AF2125),

775   goat anti-VEGFR3 (1:200, R&D systems), rat anti-ITGA6 (1:200, BioLegend, 313602) goat anti-

776   ALPL (1:200, R&D systems, AF2910), biotinylated mouse-anti TSP1 (1:200, ThermoFisher,

35

777   MA5-13395), Alexa Fluor 488-conjugated mouse anti-CLDN5 (1:100, Invitrogen, 352588), rabbit

778   anti-FSP1 (1:300, MilliporeSigma, 07-2274), goat anti-CD31 (1:300, R&D systems, AF3628), rat

779   anti-CD31 (1:100, HistoBiotec, DIA-310), rabbit anti-LEF1 (1:200, Cell Signaling Technologies,

780   2230), rat anti-VCAM1 (1:200, MilliporeSigma, CBL1300), goat anti-NOG (1:200, R&D systems,

781   AF719), goat anti-CCL21 (1:200 , R&D systems, AF457), goat anti-PROX1 (1:200, R&D

782   systems, AF2727). Following primary antibody incubation, aortae were washed three times in

783   PBS-T for 20 minutes each, then incubated with secondary antibodies in blocking solution at room

784   temperature for 90 minutes. Donkey anti-rat, anti-rabbit, and anti-goat secondary antibodies were

785   purchased from ThermoFisher or Jackson ImmunoResearch as conjugated to Alexa Fluor 405,

786   488, 546, 568, 594, or 647. TSP1 was detected with streptavidin from Jackson Immunoresearch

787   conjugated to Alexa Fluor 594 or 647. After secondary antibody incubation, aortae were washed

788   in PBS-T for 20 minutes four times, then once in PBS, then mounted in mounting reagent

789   (ProLong® Gold, Invitrogen) on a slide with the tunica intima in contact with the coverslip. A

790   textbook-sized weight was placed on top of the coverslip for 1 minute before sealing with nail

791   polish. Mesenteric vessels were whole-mounted and stained as described above.

792

793   **Confocal microscopy and image analysis**

794   Images were acquired using a Zeiss LSM810 confocal microscope equipped with an Plan-

795   Apochromat 20x/0.8 or a Plan-Apochromat 40x/1.4 oil DIC objective. Images were captured using

796   Zen2.1 (Zeiss) software and processed with Fiji (NIH). Zen2.1 software was used to threshold

797   GFP signal and manually count GFP+ nuclei per field (Figure 6). Fiji was used to quantify GFP

798   signal over PROX1+ areas (Figure 8). Figures were assembled in Adobe Illustrator.

799

S1P sample preparations

800

801   Plasma S1P was extracted as previously decribed (Frej et al., 2015) with minor

802 modification. Plasma aliquots (5 or 10 µL) were first diluted to 100 µL with TBS Buffer (50 mM

803 Tris-HCl pH 7.5, 0.15 M NaCl). S1P was extracted by adding 100 µL precipitation solution (20

804 nM D7-S1P in methanol) followed by 30 seconds of vortexing. Precipitated samples were

805 centrifuged at 18,000 rpm for 5 minutes and supernatant were transferred to vials for LC-MS/MS

806 analysis (see below).

807   C18-S1P (Avanti Lipids) was dissolved in methanol to obtain a 1 mM stock solution.

808 Standard samples were prepared by diluting the stock in 4% fatty acid free BSA (Sigma) in TBS

809 to obtain 1 µM and stored at -80 $^{\circ}$C. Before analysis, the 1 µM S1P solution was diluted with 4%

810 BSA in TBS to obtain the following concentrations: 0.5 µM, 0.25 µM, 0.125 µM, 0.0625 µM,

811 0.03125 µM, 0.0156 µM, and 0.0078 µM. S1P in diluted samples (100 µL) were extracted with

812 100 µL of methanol containing 20 nM of D7-S1P followed by 30 seconds of vortexing.

813 Precipitated samples were centrifuged at 18,000 rpm for 5 minutes and the supernatants were

814 transferred to vials for LC-MS/MS analysis. The internal deuterium-labeled standard (D7-S1P,

815 Avanti Lipids) was dissolved in methanol to obtain a 200 nM stock solution and stored at -20 °C.

816 Before analysis, the stock solution was diluted to 20 nM for sample precipitation.

817

LC-MS/MS S1P measurement and data analysis

818

819   The samples were analyzed with Q Exactive mass spectrometer coupled to a Vanquish

820 UHPLC System (Thermo Fisher Scientific). Analytes were separated using a reverse phase column

821 maintained at 60 $^{\circ}$C (XSelect CSH C18 XP column 2.5 µm, 2.1 mm X 50 mm, Waters). The

822 gradient solvents were as follows: Solvent A (water/methanol/formic acid 97/2/1 (v/v/v)) and

37

823   Solvent B (methanol/acetone/water/formic acid 68/29/2/1 (v/v/v/v)). The analytical gradient was

824   run at 0.4 mL/min from 50-100% Solvent B for 5.4 minutes, 100% for 5.5 minutes, followed by

825   one minute of 50% Solvent B. A targeted MS2 strategy (also known as parallel reaction

826   monitoring, PRM) was performed to isolate S1P (380.26 m/z) and D7-S1P (387.30 m/z) using a

827   1.6 m/z window, and the HCD-activated (stepped CE 25, 30, 50%) MS2 ions were scanned in the

828   Orbitrap at 70 K. The area under the curve (AUC) of MS2 ions (S1P, 264.2686 m/z; D7-S1P,

829   271.3125 m/z) was calculated using Skyline (MacLean et al., 2010).

830   Quantitative linearity was determined by plotting the AUC of the standard samples (C18-

831   S1P) normalized by the AUC of internal standard (D7-S1P); (y) versus the spiked concentration

832   of S1P (x). Correlation coefficient (R2) was calculated as the value of the joint variation between

833   x and y. Linear regression equation was used to determined analyte concentrations.

834

835 **Acknowledgements**

836 We thank Boston Children's Hospital & Harvard Stem Cell Institute Flow Cytometry Research

837 Facility and Harvard Medical School Biopolymers Facility for technical assistance. We also thank

838 members of the Hla laboratory for critical comments on the project and Dr. Sylvain Galvani for

839 technical advice regarding mouse aorta dissection. This work is supported by NIH grants (R35-

840 HL135821 to T.H.), Fondation Leducq Transatlantic Network grant (SphingoNet) to T.H., C.B.,

841 E.C. and R.L.P., intramural research program of NIDDK intramural program grants (R.L.P) and a

842 postdoctoral fellowship from the American Heart Association to A.K.

843

844 **Competing interests**

845 T.H. received grant support from ONO Pharmaceuticals (2015-2018), has filed patent applications

846 on ApoM, ApoM-Fc and HDL containing ApoM, and has consulted for the following commercial

847 entities: Astellas, Steptoe and Johnson, Gerson Lehrman Group Council, Janssen Research &

848 Development, LLC, and Sun Pharma advanced research group (SPARC).

849

References

Adey, A., Morrison, H. G., Asan, Xun, X., Kitzman, J. O., Turner, E. H., . . . Shendure, J. (2010). Rapid, low-input, low-bias construction of shotgun fragment libraries by high-density in vitro transposition. *Genome Biol, 11*(12), R119. doi:10.1186/gb-2010-11-12-r119

Allende, M. L., Yamashita, T., & Proia, R. L. (2003). G-protein-coupled receptor S1P1 acts within endothelial cells to regulate vascular maturation. *Blood, 102*(10), 3665-3667. doi:10.1182/blood-2003-02-0460

Barnea, G., Strapps, W., Herrada, G., Berman, Y., Ong, J., Kloss, B., . . . Lee, K. J. (2008). The genetic design of signaling cascades to record receptor activation. *Proc Natl Acad Sci U S A, 105*(1), 64-69. doi:10.1073/pnas.0710487105

Buenrostro, J. D., Giresi, P. G., Zaba, L. C., Chang, H. Y., & Greenleaf, W. J. (2013). Transposition of native chromatin for fast and sensitive epigenomic profiling of open chromatin, DNA-binding proteins and nucleosome position. *Nat Methods, 10*(12), 1213-1218. doi:10.1038/nmeth.2688

Camerer, E., Regard, J. B., Cornelissen, I., Srinivasan, Y., Duong, D. N., Palmer, D., . . . Coughlin, S. R. (2009). Sphingosine-1-phosphate in the plasma compartment regulates basal and inflammation-induced vascular leak in mice. *J Clin Invest, 119*(7), 1871-1879. doi:10.1172/jci38575

Chiu, J. J., & Chien, S. (2011). Effects of disturbed flow on vascular endothelium: pathophysiological basis and clinical perspectives. *Physiol Rev, 91*(1), 327-387. doi:10.1152/physrev.00047.2009

Christensen, P. M., Liu, C. H., Swendeman, S. L., Obinata, H., Qvortrup, K., Nielsen, L. B., . . . Christoffersen, C. (2016). Impaired endothelial barrier function in apolipoprotein M-deficient mice is dependent on sphingosine-1-phosphate receptor 1. *FASEB J, 30*(6), 2351-2359. doi:10.1096/fj.201500064

Christoffersen, C., Obinata, H., Kumaraswamy, S. B., Galvani, S., Ahnstrom, J., Sevvana, M., . . . Dahlback, B. (2011). Endothelium-protective sphingosine-1-phosphate provided by HDL-associated apolipoprotein M. *Proc Natl Acad Sci U S A, 108*(23), 9613-9618. doi:10.1073/pnas.1103187108

Corada, M., Orsenigo, F., Morini, M. F., Pitulescu, M. E., Bhat, G., Nyqvist, D., . . . Dejana, E. (2013). Sox17 is indispensable for acquisition and maintenance of arterial identity. *Nat Commun, 4*, 2609. doi:10.1038/ncomms3609

Corces, M. R., Buenrostro, J. D., Wu, B., Greenside, P. G., Chan, S. M., Koenig, J. L., . . . Chang, H. Y. (2016). Lineage-specific and single-cell chromatin accessibility charts human hematopoiesis and leukemia evolution. *Nat Genet, 48*(10), 1193-1203. doi:10.1038/ng.3646

Csanyi, G., & Singla, B. (2019). Arterial Lymphatics in Atherosclerosis: Old Questions, New Insights, and Remaining Challenges. *J Clin Med, 8*(4). doi:10.3390/jcm8040495

Dobin, A., Davis, C. A., Schlesinger, F., Drenkow, J., Zaleski, C., Jha, S., . . . Gingeras, T. R. (2013). STAR: ultrafast universal RNA-seq aligner. *Bioinformatics, 29*(1), 15-21. doi:10.1093/bioinformatics/bts635

Fan, J., Salathia, N., Liu, R., Kaeser, G. E., Yung, Y. C., Herman, J. L., . . . Kharchenko, P. V. (2016). Characterizing transcriptional heterogeneity through pathway and gene set overdispersion analysis. *Nat Methods, 13*(3), 241-244. doi:10.1038/nmeth.3734

895 Frej, C., Andersson, A., Larsson, B., Guo, L. J., Norstrom, E., Happonen, K. E., & Dahlback, B.
896   (2015). Quantification of sphingosine 1-phosphate by validated LC-MS/MS method
897   revealing strong correlation with apolipoprotein M in plasma but not in serum due to
898   platelet activation during blood coagulation. *Anal Bioanal Chem, 407*(28), 8533-8542.
899   doi:10.1007/s00216-015-9008-4
900 Gaengel, K., Niaudet, C., Hagikura, K., Lavina, B., Muhl, L., Hofmann, J. J., . . . Betsholtz, C.
901   (2012). The sphingosine-1-phosphate receptor S1PR1 restricts sprouting angiogenesis by
902   regulating the interplay between VE-cadherin and VEGFR2. *Dev Cell, 23*(3), 587-599.
903   doi:10.1016/j.devcel.2012.08.005
904 Galkina, E., & Ley, K. (2009). Immune and inflammatory mechanisms of atherosclerosis (*). *Annu
905   Rev Immunol, 27*, 165-197. doi:10.1146/annurev.immunol.021908.132620
906 Galvani, S., Sanson, M., Blaho, V. A., Swendeman, S. L., Obinata, H., Conger, H., . . . Hla, T.
907   (2015). HDL-bound sphingosine 1-phosphate acts as a biased agonist for the endothelial
908   cell receptor S1P1 to limit vascular inflammation. *Sci Signal, 8*(389), ra79.
909   doi:10.1126/scisignal.aaa2581
910 Heinz, S., Benner, C., Spann, N., Bertolino, E., Lin, Y. C., Laslo, P., . . . Glass, C. K. (2010).
911   Simple combinations of lineage-determining transcription factors prime cis-regulatory
912   elements required for macrophage and B cell identities. *Mol Cell, 38*(4), 576-589.
913   doi:10.1016/j.molcel.2010.05.004
914 Jung, B., Obinata, H., Galvani, S., Mendelson, K., Ding, B. S., Skoura, A., . . . Hla, T. (2012).
915   Flow-regulated endothelial S1P receptor-1 signaling sustains vascular development. *Dev
916   Cell, 23*(3), 600-610. doi:10.1016/j.devcel.2012.07.015
917 Kalluri, A. S., Vellarikkal, S. K., Edelman, E. R., Nguyen, L., Subramanian, A., Ellinor, P. T., . .
918   . Gupta, R. M. (2019). Single-Cell Analysis of the Normal Mouse Aorta Reveals
919   Functionally Distinct Endothelial Cell Populations. *Circulation, 140*(2), 147-163.
920   doi:10.1161/CIRCULATIONAHA.118.038362
921 Kaur, H., Carvalho, J., Looso, M., Singh, P., Chennupati, R., Preussner, J., . . . Wettschureck, N.
922   (2017). Single-cell profiling reveals heterogeneity and functional patterning of GPCR
923   expression in the vascular system. *Nat Commun, 8*, 15700. doi:10.1038/ncomms15700
924 Kono, M., Tucker, A. E., Tran, J., Bergner, J. B., Turner, E. M., & Proia, R. L. (2014).
925   Sphingosine-1-phosphate receptor 1 reporter mice reveal receptor activation sites in vivo.
926   *J Clin Invest, 124*(5), 2076-2086. doi:10.1172/JCI71194
927 La Manno, G., Soldatov, R., Zeisel, A., Braun, E., Hochgerner, H., Petukhov, V., . . . Kharchenko,
928   P. V. (2018). RNA velocity of single cells. *Nature, 560*(7719), 494-498.
929   doi:10.1038/s41586-018-0414-6
930 Langmead, B., & Salzberg, S. L. (2012). Fast gapped-read alignment with Bowtie 2. *Nat Methods,
931   9*(4), 357-359. doi:10.1038/nmeth.1923
932 Li, B., & Dewey, C. N. (2011). RSEM: accurate transcript quantification from RNA-Seq data with
933   or without a reference genome. *BMC Bioinformatics, 12*, 323. doi:10.1186/1471-2105-12-
934   323
935 Li, Z., Schulz, M. H., Look, T., Begemann, M., Zenke, M., & Costa, I. G. (2019). Identification of
936   transcription factor binding sites using ATAC-seq. *Genome Biol, 20*(1), 45.
937   doi:10.1186/s13059-019-1642-2
938 Liao, Y., Smyth, G. K., & Shi, W. (2013). The Subread aligner: fast, accurate and scalable read
939   mapping by seed-and-vote. *Nucleic Acids Res, 41*(10), e108. doi:10.1093/nar/gkt214

Lindskog, H., Kim, Y. H., Jelin, E. B., Kong, Y., Guevara-Gallardo, S., Kim, T. N., & Wang, R. A. (2014). Molecular identification of venous progenitors in the dorsal aorta reveals an aortic origin for the cardinal vein in mammals. *Development, 141*(5), 1120-1128. doi:10.1242/dev.101808

Liu, C. H., Thangada, S., Lee, M. J., Van Brocklyn, J. R., Spiegel, S., & Hla, T. (1999). Ligand-induced trafficking of the sphingosine-1-phosphate receptor EDG-1. *Mol Biol Cell, 10*(4), 1179-1190. doi:10.1091/mbc.10.4.1179

Lukowski, S. W., Patel, J., Andersen, S. B., Sim, S. L., Wong, H. Y., Tay, J., . . . Khosrotehrani, K. (2019). Single-Cell Transcriptional Profiling of Aortic Endothelium Identifies a Hierarchy from Endovascular Progenitors to Differentiated Cells. *Cell Rep, 27*(9), 2748-2758 e2743. doi:10.1016/j.celrep.2019.04.102

MacLean, B., Tomazela, D. M., Shulman, N., Chambers, M., Finney, G. L., Frewen, B., . . . MacCoss, M. J. (2010). Skyline: an open source document editor for creating and analyzing targeted proteomics experiments. *Bioinformatics, 26*(7), 966-968. doi:10.1093/bioinformatics/btq054

Maiellaro, K., & Taylor, W. R. (2007). The role of the adventitia in vascular inflammation. *Cardiovasc Res, 75*(4), 640-648. doi:10.1016/j.cardiores.2007.06.023

McDonald, A. I., Shirali, A. S., Aragon, R., Ma, F., Hernandez, G., Vaughn, D. A., . . . Iruela-Arispe, M. L. (2018). Endothelial Regeneration of Large Vessels Is a Biphasic Process Driven by Local Cells with Distinct Proliferative Capacities. *Cell Stem Cell, 23*(2), 210-225 e216. doi:10.1016/j.stem.2018.07.011

Mirza, M. A., Capozzi, L. A., Xu, Y., McCullough, L. D., & Liu, F. (2013). Knockout of vascular early response gene worsens chronic stroke outcomes in neonatal mice. *Brain Res Bull, 98*, 111-121. doi:10.1016/j.brainresbull.2013.07.011

Neph, S., Kuehn, M. S., Reynolds, A. P., Haugen, E., Thurman, R. E., Johnson, A. K., . . . Stamatoyannopoulos, J. A. (2012). BEDOPS: high-performance genomic feature operations. *Bioinformatics, 28*(14), 1919-1920. doi:10.1093/bioinformatics/bts277

Olsson, A. K., Dimberg, A., Kreuger, J., & Claesson-Welsh, L. (2006). VEGF receptor signalling - in control of vascular function. *Nat Rev Mol Cell Biol, 7*(5), 359-371. doi:10.1038/nrm1911

Oo, M. L., Chang, S. H., Thangada, S., Wu, M. T., Rezaul, K., Blaho, V., . . . Hla, T. (2011). Engagement of S1P(1)-degradative mechanisms leads to vascular leak in mice. *J Clin Invest, 121*(6), 2290-2300. doi:10.1172/JCI45403

Oo, M. L., Thangada, S., Wu, M. T., Liu, C. H., Macdonald, T. L., Lynch, K. R., . . . Hla, T. (2007). Immunosuppressive and anti-angiogenic sphingosine 1-phosphate receptor-1 agonists induce ubiquitinylation and proteasomal degradation of the receptor. *J Biol Chem, 282*(12), 9082-9089. doi:10.1074/jbc.M610318200

Pham, T. H., Baluk, P., Xu, Y., Grigorova, I., Bankovich, A. J., Pappu, R., . . . Cyster, J. G. (2010). Lymphatic endothelial cell sphingosine kinase activity is required for lymphocyte egress and lymphatic patterning. *J Exp Med, 207*(1), 17-27. doi:10.1084/jem.20091619

Picelli, S., Faridani, O. R., Bjorklund, A. K., Winberg, G., Sagasser, S., & Sandberg, R. (2014). Full-length RNA-seq from single cells using Smart-seq2. *Nat Protoc, 9*(1), 171-181. doi:10.1038/nprot.2014.006

Pijuan-Sala, B., Griffiths, J. A., Guibentif, C., Hiscock, T. W., Jawaid, W., Calero-Nieto, F. J., . . . Gottgens, B. (2019). A single-cell molecular map of mouse gastrulation and early organogenesis. *Nature, 566*(7745), 490-495. doi:10.1038/s41586-019-0933-9

Primo, L., Seano, G., Roca, C., Maione, F., Gagliardi, P. A., Sessa, R., . . . Bussolino, F. (2010). Increased expression of alpha6 integrin in endothelial cells unveils a proangiogenic role for basement membrane. *Cancer Res, 70*(14), 5759-5769. doi:10.1158/0008-5472.CAN-10-0507

Proia, R. L., & Hla, T. (2015). Emerging biology of sphingosine-1-phosphate: its role in pathogenesis and therapy. *J Clin Invest, 125*(4), 1379-1387. doi:10.1172/JCI76369

Pu, W., He, L., Han, X., Tian, X., Li, Y., Zhang, H., . . . Zhou, B. (2018). Genetic Targeting of Organ-Specific Blood Vessels. *Circ Res, 123*(1), 86-99. doi:10.1161/CIRCRESAHA.118.312981

Quinlan, A. R., & Hall, I. M. (2010). BEDTools: a flexible suite of utilities for comparing genomic features. *Bioinformatics, 26*(6), 841-842. doi:10.1093/bioinformatics/btq033

Ramirez, F., Ryan, D. P., Gruning, B., Bhardwaj, V., Kilpert, F., Richter, A. S., . . . Manke, T. (2016). deepTools2: a next generation web server for deep-sequencing data analysis. *Nucleic Acids Res, 44*(W1), W160-165. doi:10.1093/nar/gkw257

Robinson, J. T., Thorvaldsdottir, H., Winckler, W., Guttman, M., Lander, E. S., Getz, G., & Mesirov, J. P. (2011). Integrative genomics viewer. *Nat Biotechnol, 29*(1), 24-26. doi:10.1038/nbt.1754

Robinson, M. D., McCarthy, D. J., & Smyth, G. K. (2010). edgeR: a Bioconductor package for differential expression analysis of digital gene expression data. *Bioinformatics, 26*(1), 139-140. doi:10.1093/bioinformatics/btp616

Shaw, P. X., Horkko, S., Chang, M. K., Curtiss, L. K., Palinski, W., Silverman, G. J., & Witztum, J. L. (2000). Natural antibodies with the T15 idiotype may act in atherosclerosis, apoptotic clearance, and protective immunity. *J Clin Invest, 105*(12), 1731-1740. doi:10.1172/JCI8472

Shen, L., Shao, N. Y., Liu, X., Maze, I., Feng, J., & Nestler, E. J. (2013). diffReps: detecting differential chromatin modification sites from ChIP-seq data with biological replicates. *PLoS One, 8*(6), e65598. doi:10.1371/journal.pone.0065598

Simmons, S., Sasaki, N., Umemoto, E., Uchida, Y., Fukuhara, S., Kitazawa, Y., . . . Ishii, M. (2019). High-endothelial cell-derived S1P regulates dendritic cell localization and vascular integrity in the lymph node. *Elife, 8*. doi:10.7554/eLife.41239

Sorensen, I., Adams, R. H., & Gossler, A. (2009). DLL1-mediated Notch activation regulates endothelial identity in mouse fetal arteries. *Blood, 113*(22), 5680-5688. doi:10.1182/blood-2008-08-174508

Taher, M., Nakao, S., Zandi, S., Melhorn, M. I., Hayes, K. C., & Hafezi-Moghadam, A. (2016). Phenotypic transformation of intimal and adventitial lymphatics in atherosclerosis: a regulatory role for soluble VEGF receptor 2. *FASEB J, 30*(7), 2490-2499. doi:10.1096/fj.201500112

Takeda, K., Cowan, A., & Fong, G. H. (2007). Essential role for prolyl hydroxylase domain protein 2 in oxygen homeostasis of the adult vascular system. *Circulation, 116*(7), 774-781. doi:10.1161/CIRCULATIONAHA.107.701516

Ulvmar, M. H., & Makinen, T. (2016). Heterogeneity in the lymphatic vascular system and its origin. *Cardiovasc Res, 111*(4), 310-321. doi:10.1093/cvr/cvw175

Vaahtomeri, K., Brown, M., Hauschild, R., De Vries, I., Leithner, A. F., Mehling, M., . . . Sixt, M. (2017). Locally Triggered Release of the Chemokine CCL21 Promotes Dendritic Cell Transmigration across Lymphatic Endothelia. *Cell Rep, 19*(5), 902-909. doi:10.1016/j.celrep.2017.04.027

1032   Vanlandewijck, M., He, L., Mae, M. A., Andrae, J., Ando, K., Del Gaudio, F., . . . Betsholtz, C.
1033   (2018). A molecular atlas of cell types and zonation in the brain vasculature. *Nature, 554*(7693), 475-480. doi:10.1038/nature25739
1035   Wang, Y., Jin, Y., Mae, M. A., Zhang, Y., Ortsater, H., Betsholtz, C., . . . Jakobsson, L. (2017). Smooth muscle cell recruitment to lymphatic vessels requires PDGFB and impacts vessel size but not identity. *Development, 144*(19), 3590-3601. doi:10.1242/dev.147967
1038   White, G. E., & Greaves, D. R. (2012). Fractalkine: a survivor's guide: chemokines as antiapoptotic mediators. *Arterioscler Thromb Vasc Biol, 32*(3), 589-594. doi:10.1161/ATVBAHA.111.237412
1041   Wisler, J. W., Rockman, H. A., & Lefkowitz, R. J. (2018). Biased G Protein-Coupled Receptor Signaling: Changing the Paradigm of Drug Discovery. *Circulation, 137*(22), 2315-2317. doi:10.1161/CIRCULATIONAHA.117.028194
1044   Yanagida, K., Liu, C. H., Faraco, G., Galvani, S., Smith, H. K., Burg, N., . . . Hla, T. (2017). Size-selective opening of the blood-brain barrier by targeting endothelial sphingosine 1-phosphate receptor 1. *Proc Natl Acad Sci U S A, 114*(17), 4531-4536. doi:10.1073/pnas.1618659114
1048   Zhang, Y., Liu, T., Meyer, C. A., Eeckhoute, J., Johnson, D. S., Bernstein, B. E., . . . Liu, X. S. (2008). Model-based analysis of ChIP-Seq (MACS). *Genome Biol, 9*(9), R137. doi:10.1186/gb-2008-9-9-r137
1051   Zhou, Y., Williams, J., Smallwood, P. M., & Nathans, J. (2015). Sox7, Sox17, and Sox18 Cooperatively Regulate Vascular Development in the Mouse Retina. *PLoS One, 10*(12), e0143650. doi:10.1371/journal.pone.0143650
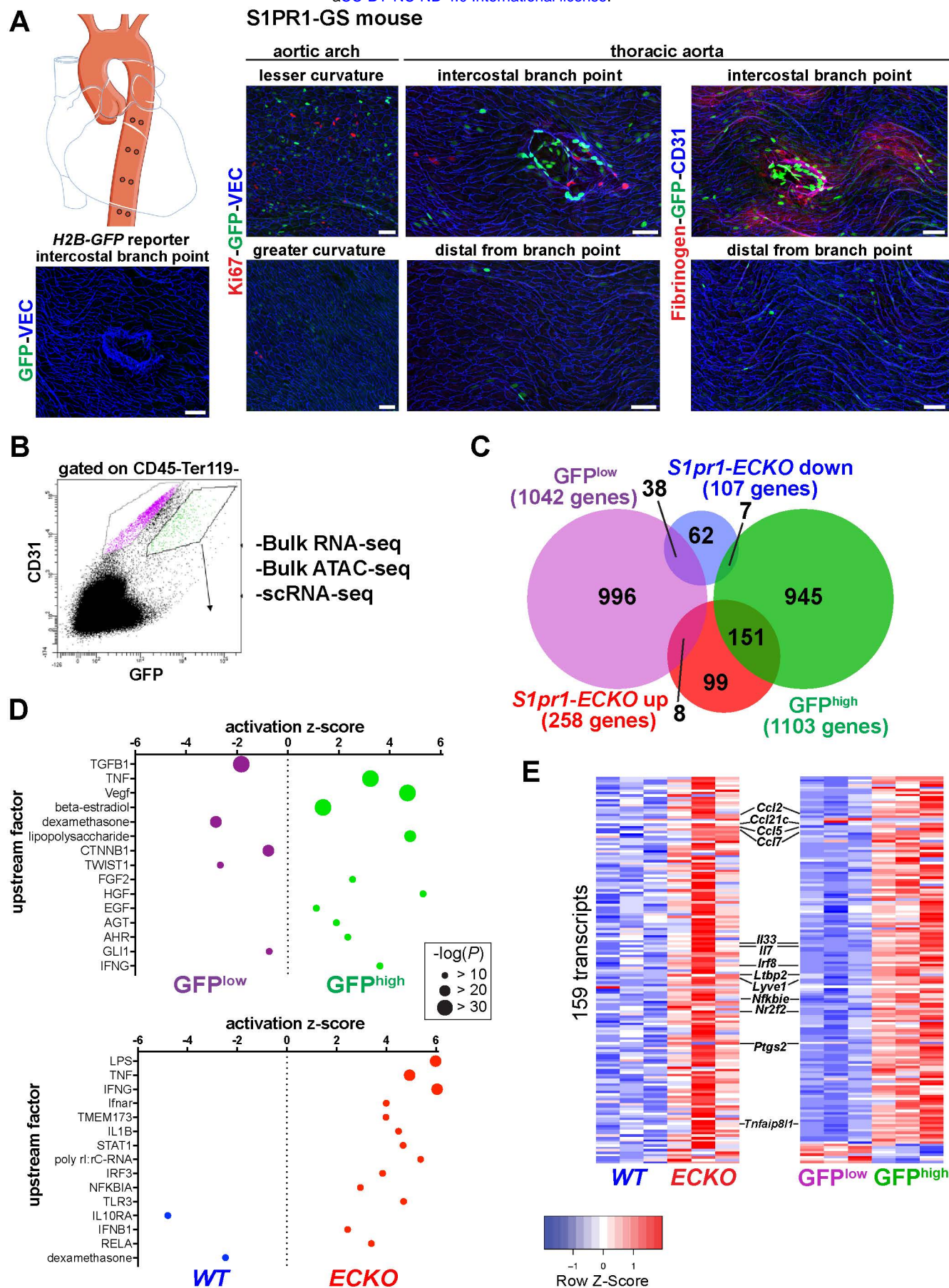
1054

Figure 1. High S1PR1/β-arrestin coupling in normal mouse aortic endothelium exhibits transcriptomic concordance with S1PR1 loss-of-function.
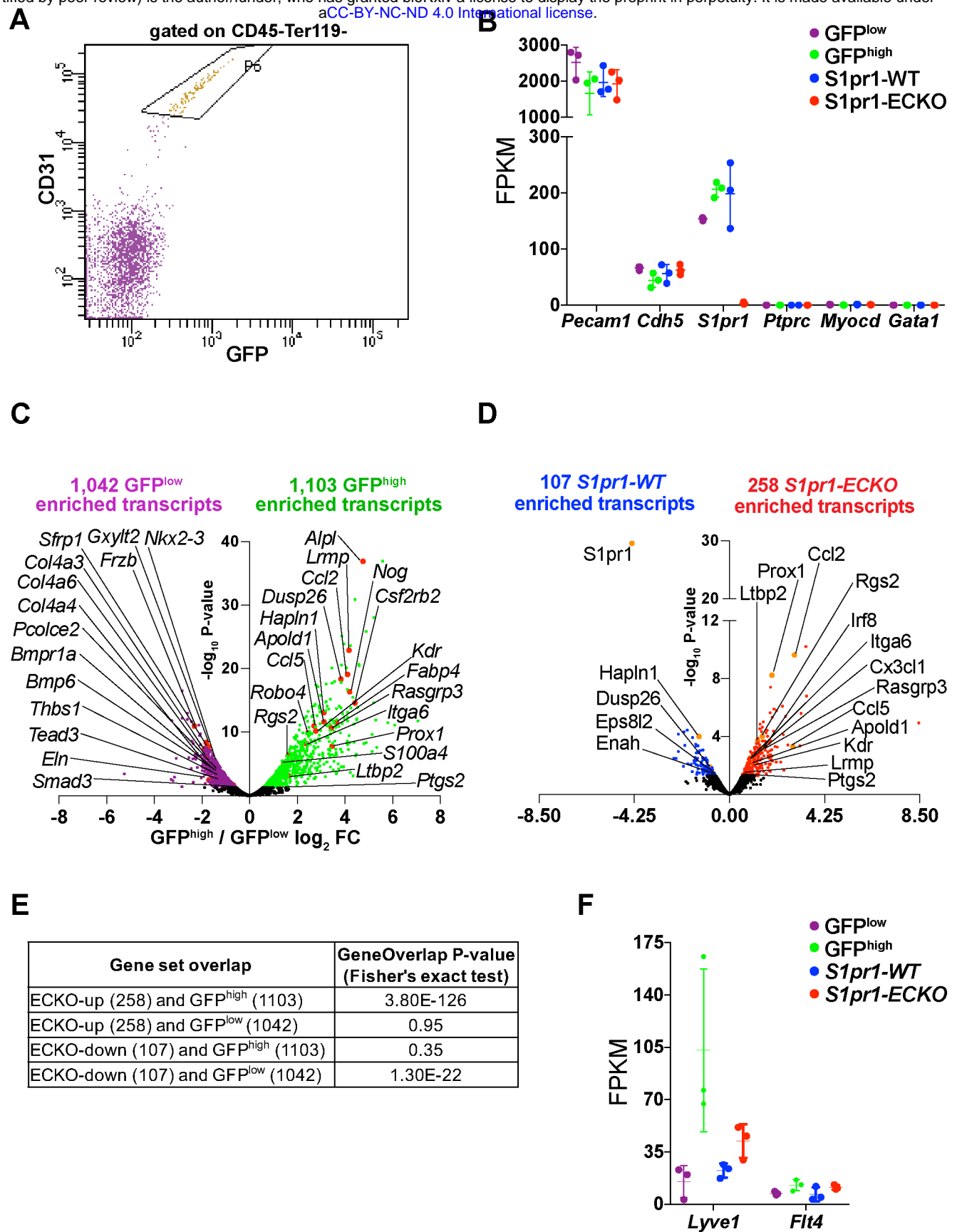
Figure 1 supplement 1. RNA-seq quality control and differential gene expression between GFP^{high} and GFP^{low} and *S1pr1-ECKO* and *WT* MAECs.
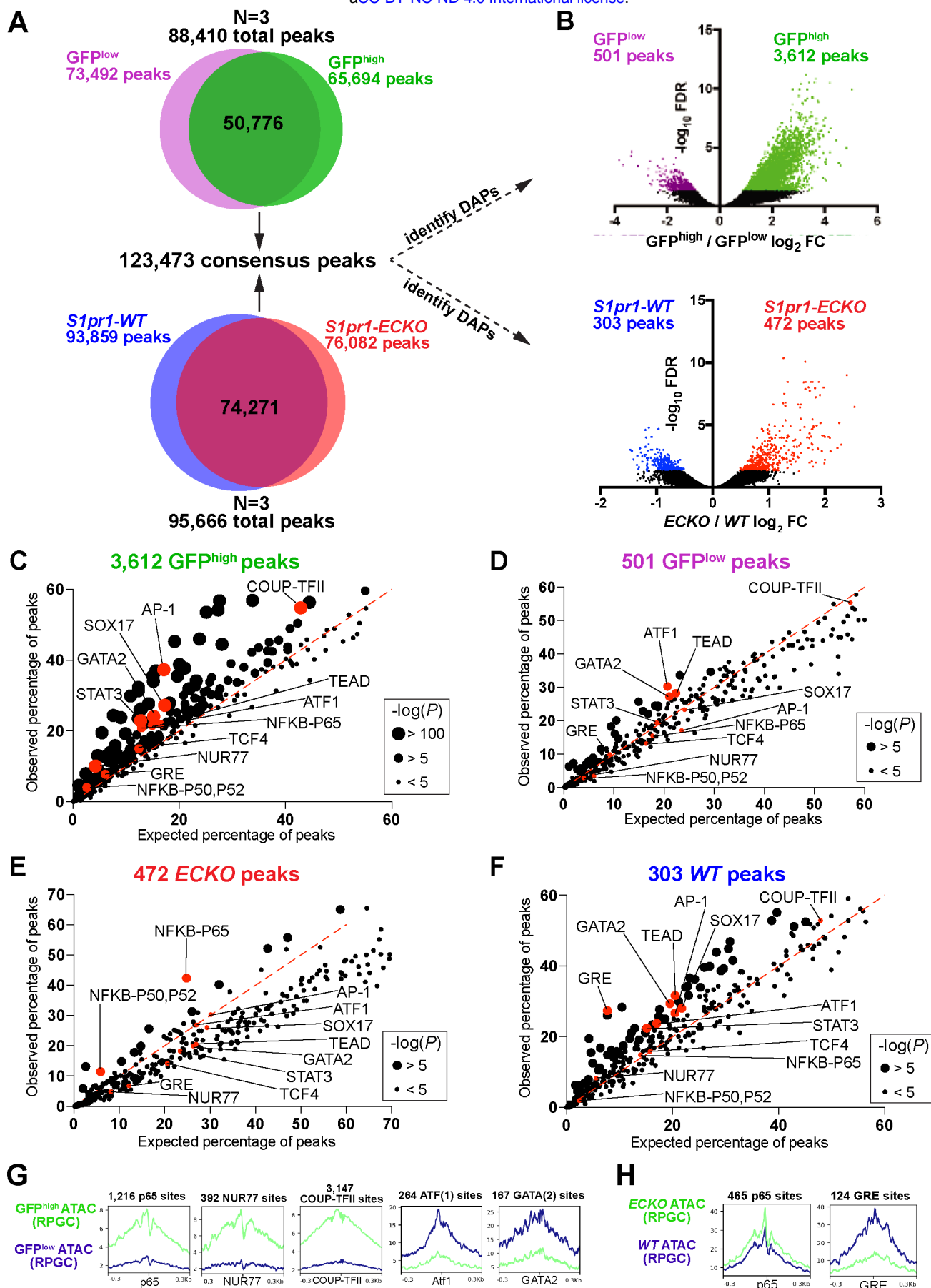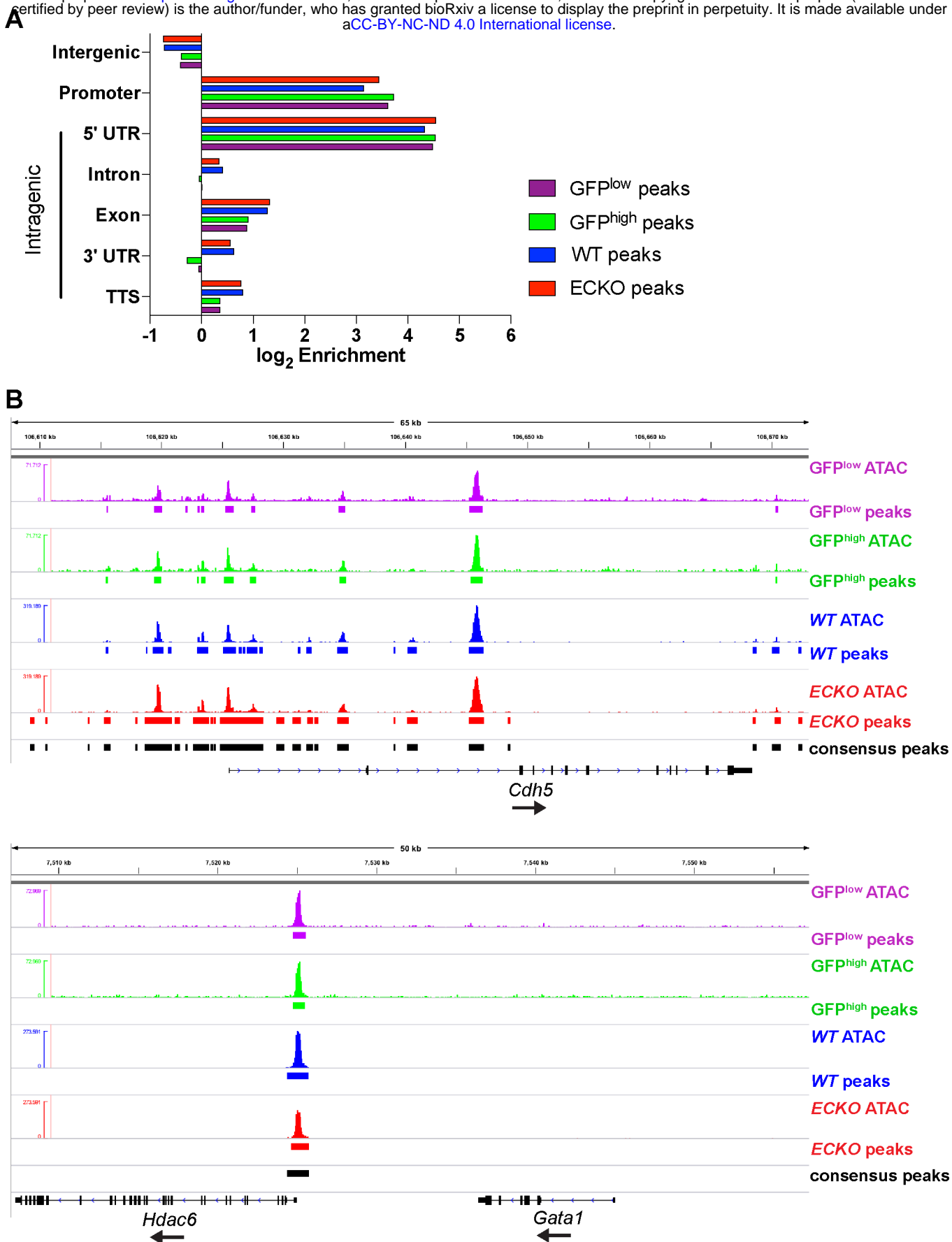
E

Gene set overlap	GeneOverlap P-value (Fisher's exact test)
ECKO-up (258) and GFP^{high} (1103)	3.80E-126
ECKO-up (258) and GFP^{low} (1042)	0.95
ECKO-down (107) and GFP^{high} (1103)	0.35
ECKO-down (107) and GFP^{low} (1042)	1.30E-22

46

Figure 2. S1PR1 loss-of-function and high levels of β-arrestin coupling are associated with an NFκB signature in open chromatin.

47

Figure 2 supplement 1. ATAC-seq quality control and peak annotation.

Figure 2 supplement 2. Genome-wide concordance between promoter-proximal chromatin accessibility and mRNA expression in sorted MAEC populations.

49

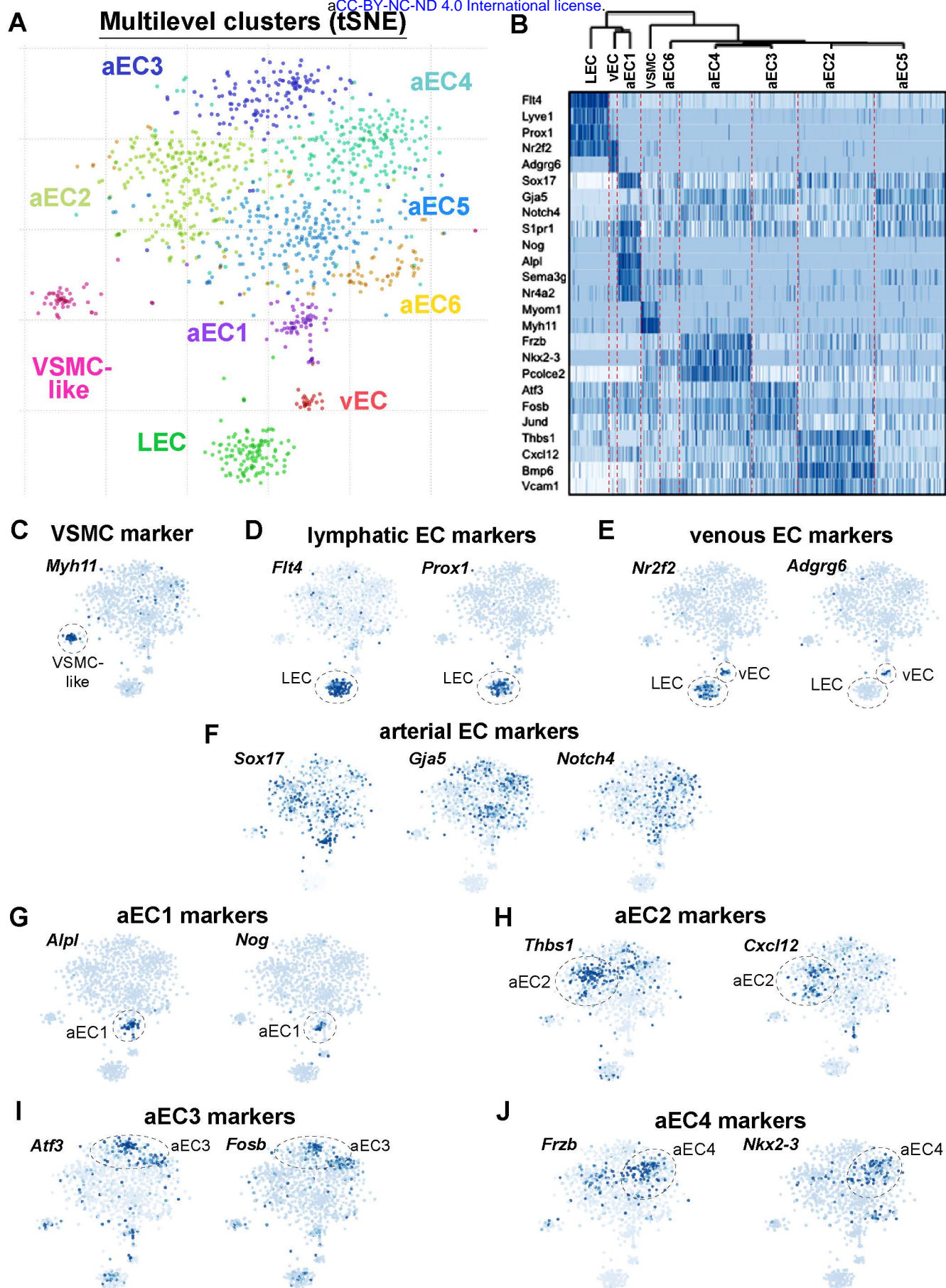**Figure 2 supplement 3.** Genome-wide chromatin footprinting with HINT-ATAC.

A **Multilevel clusters (tSNE)**

B

C **VSMC marker**

D **lymphatic EC markers**

E **venous EC markers**

F **arterial EC markers**

G **aEC1 markers**

H **aEC2 markers**

I **aEC3 markers**

J **aEC4 markers**

Figure 3. Single-cell RNA-sequencing of GFP^{high} and GFP^{low} MAECs.

Figure 3 supplement 1. Expression of cluster-defining transcripts in single GFP^{high} and GFP^{low} MAECs.
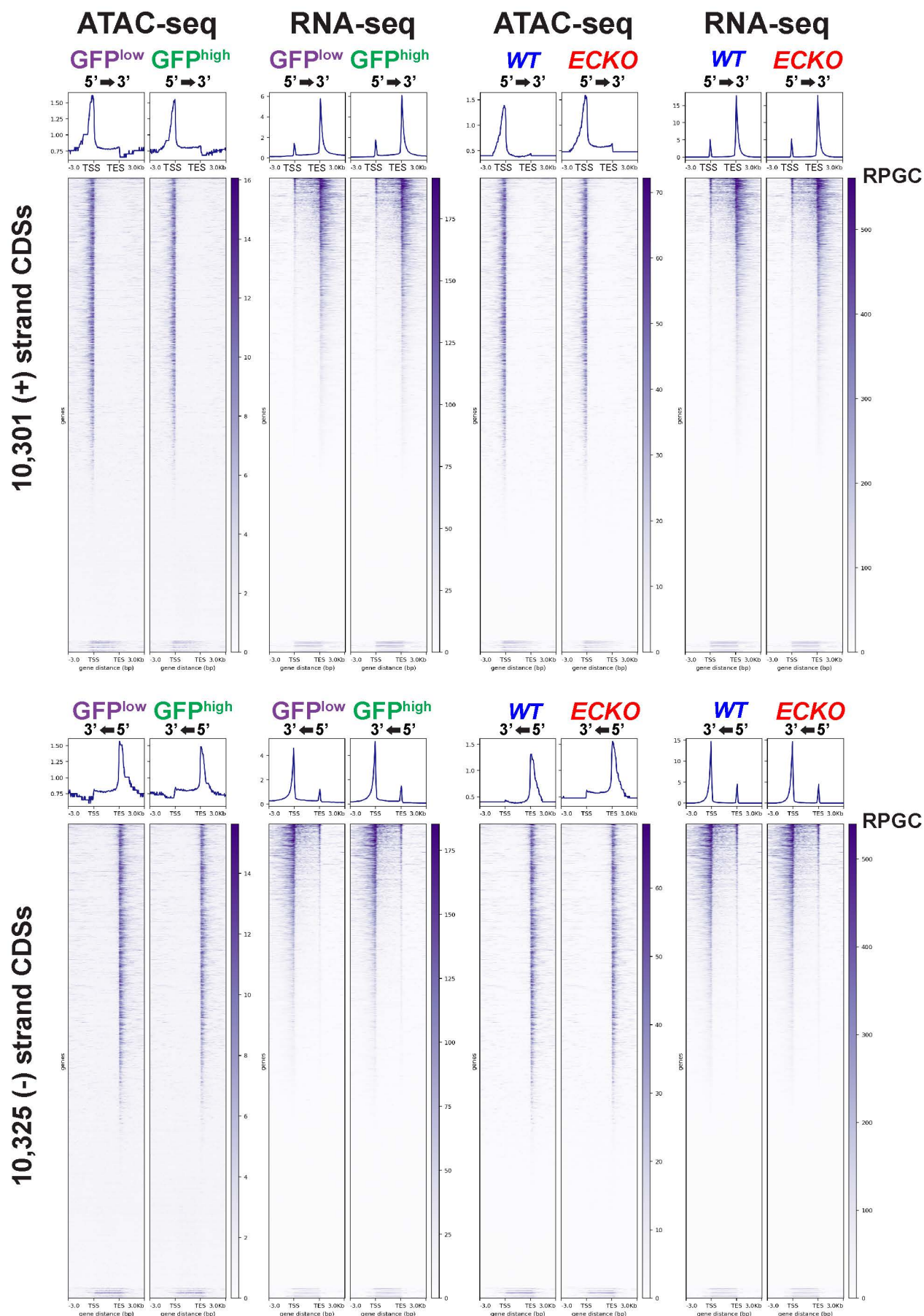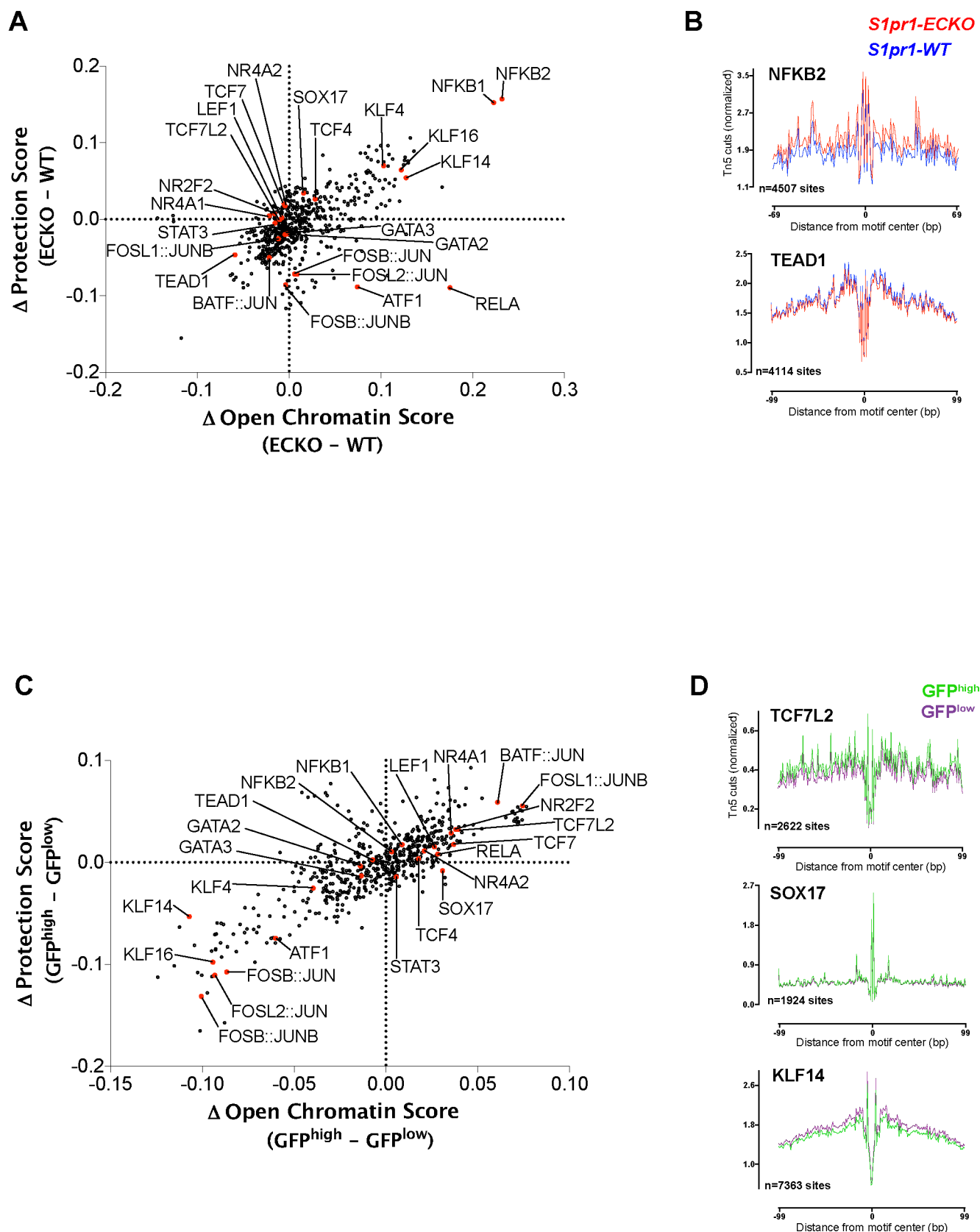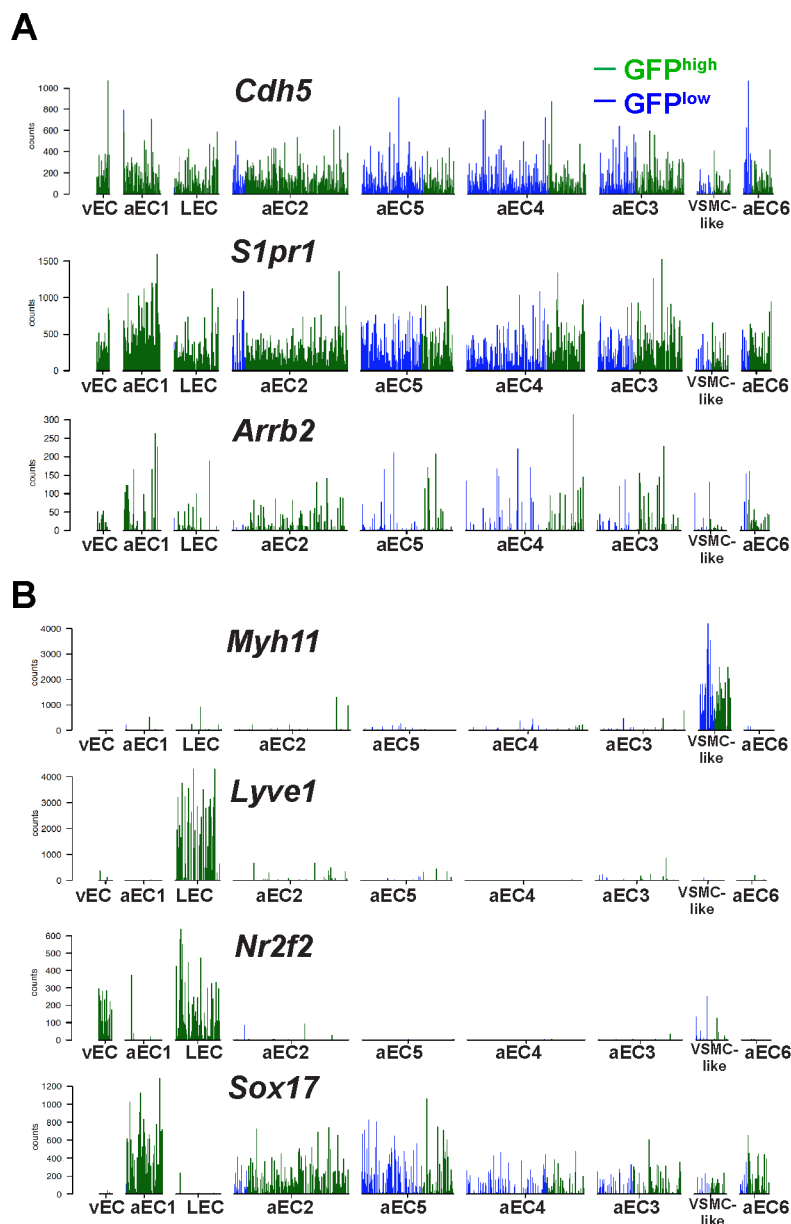
Figure 3 supplement 2. Top marker transcripts for each of the nine clusters defined by scRNA-seq analysis of GFP^{high} and GFP^{low} MAECs.

A

Cluster	Name	No. Cells	% GFP^{high}	Enriched transcripts (Z-score > 3)
1	LEC	114	96	893
2	vEC	32	100	283
3	aEC1	70	97	411
4	aEC2	236	92	1517
5	aEC3	134	56	189
6	aEC4	208	30	228
7	aEC5	227	49	77
8	aEC6	66	83	191
9	VSMC-like	64	59	628

B
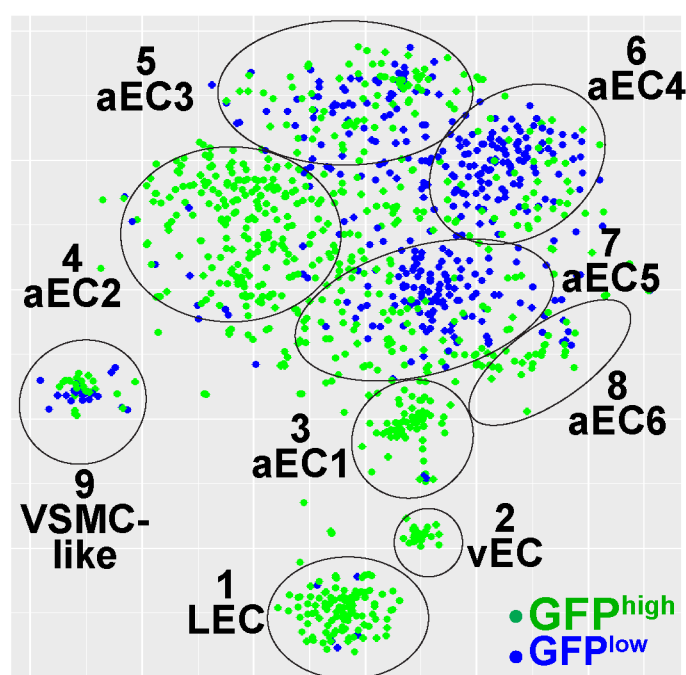
Figure 3 supplement 3. General features and nomenclature of the nine clusters defined by scRNA-seq analysis of GFP^{high} and GFP^{low} MAECs.

54
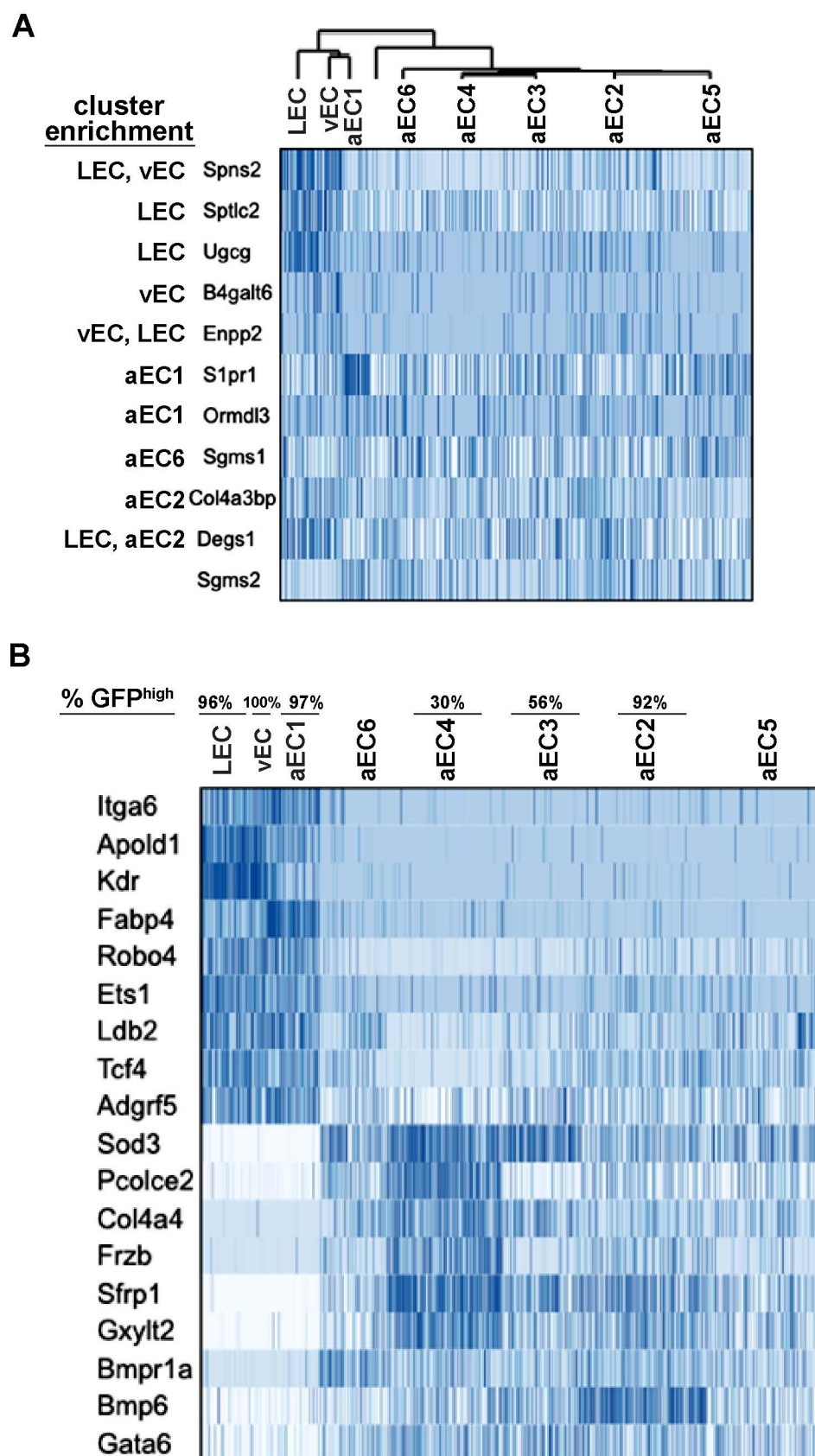
Figure 3 supplement 4. Transcripts co-enriched in LEC, vEC, and aEC1.
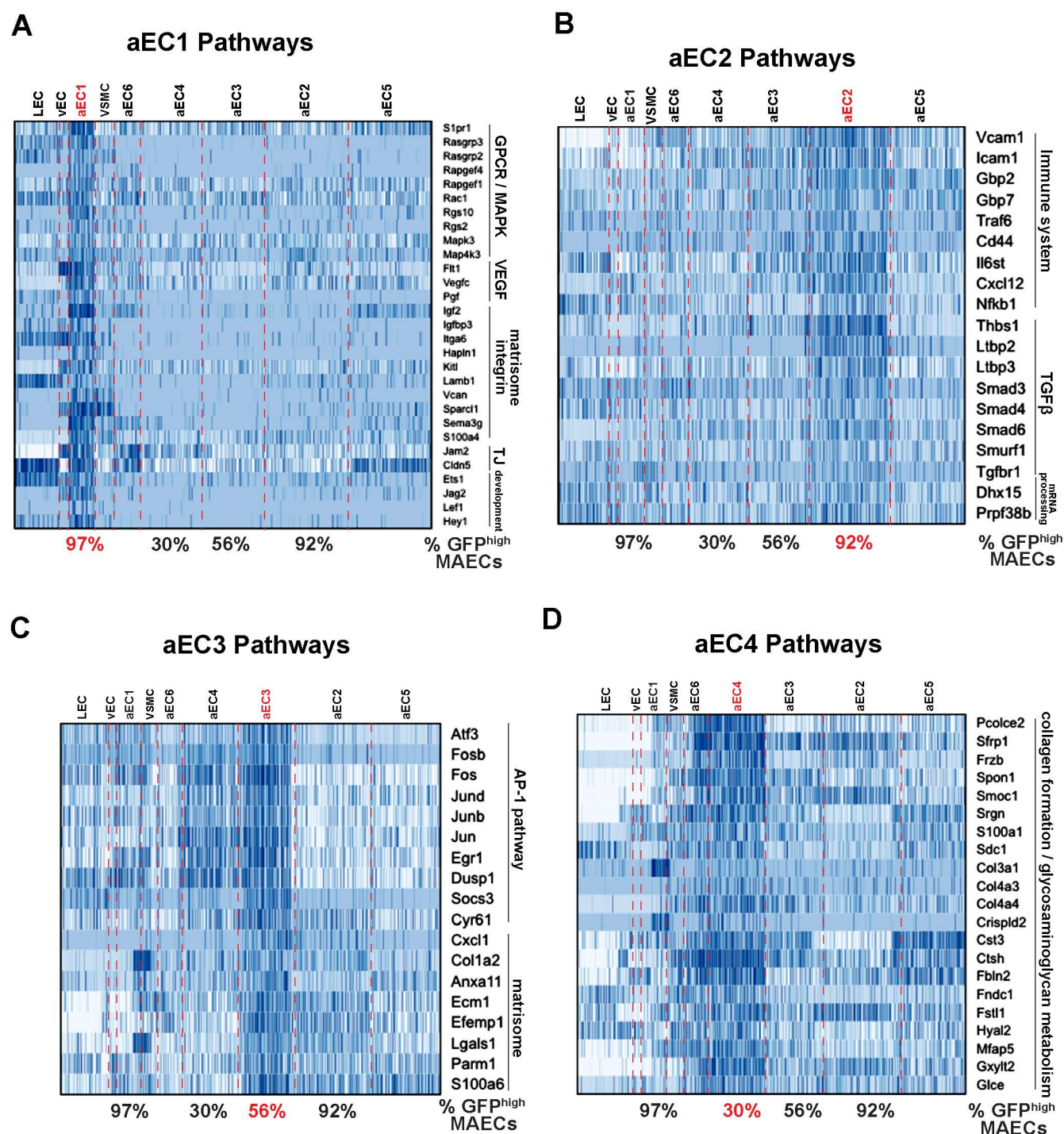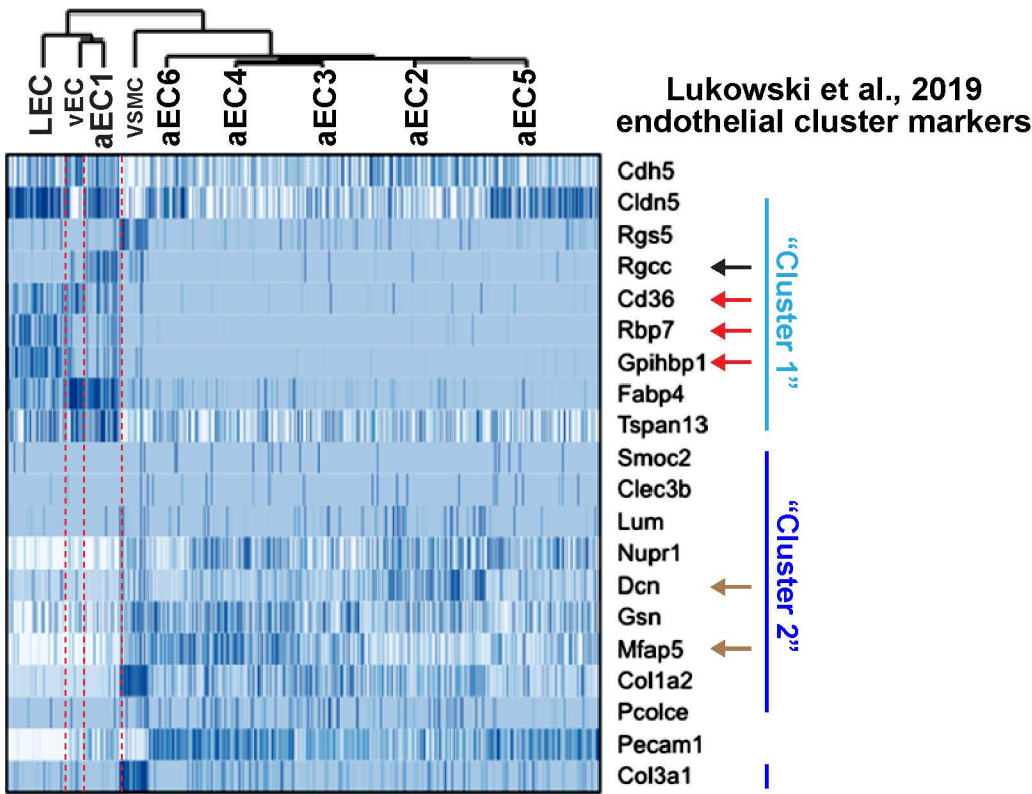
Figure 4. Functional annotation of arterial MAEC clusters aEC1, aEC2, aEC3, and aEC4.
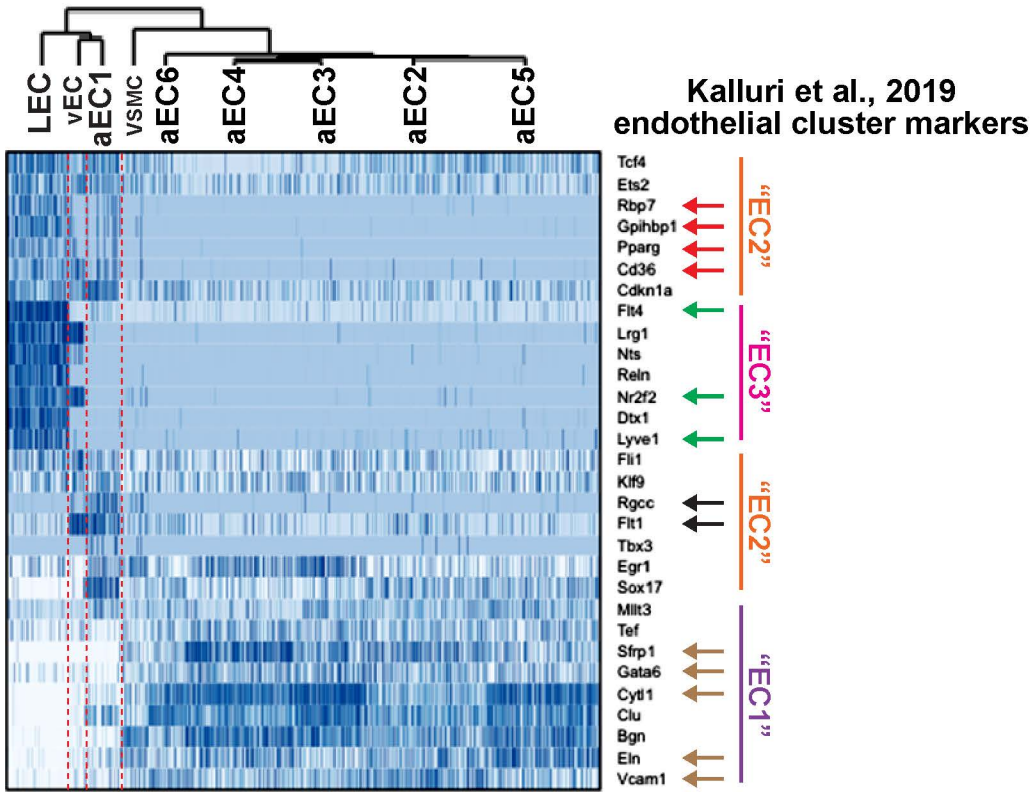
Figure 4 supplement 1. Expression of aortic EC cluster markers from Lukowski et al. (2019) and Kalluri et al. (2019) in LEC, vEC, and aEC1-6.
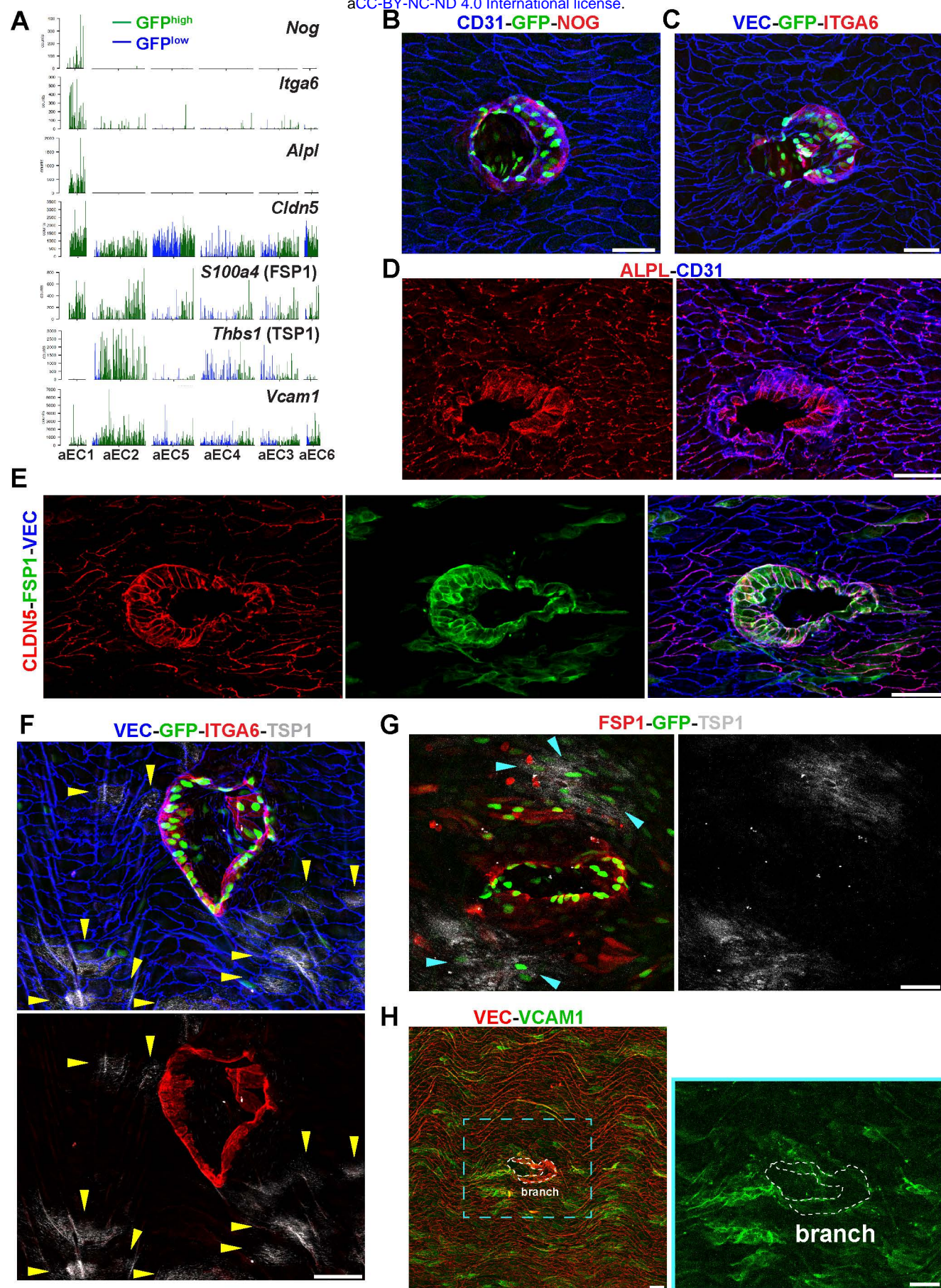
Figure 5. Identification of aEC1 as arterial ECs around the circumference of branch point orifices.
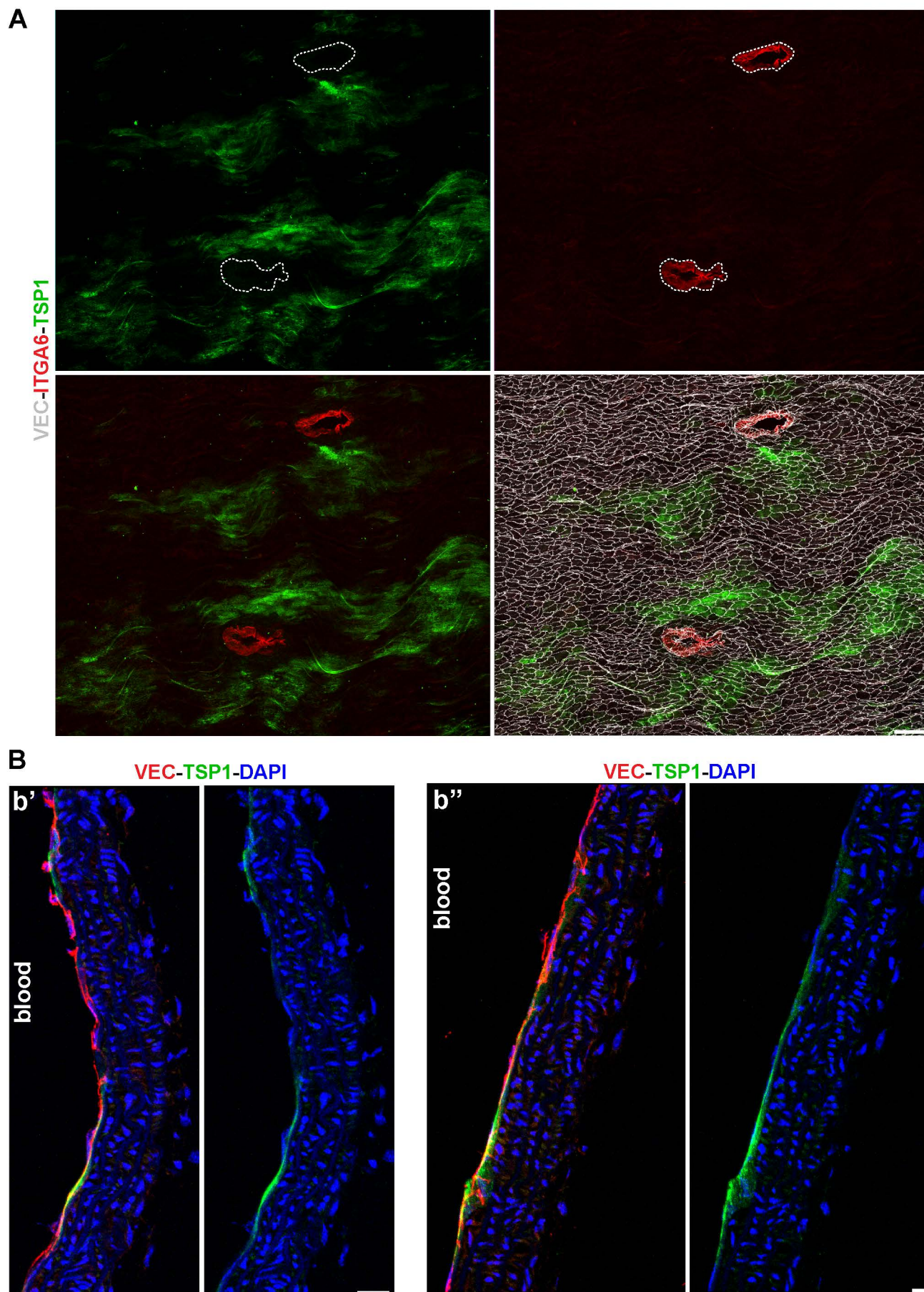
Figure 5 supplement 1. Patchy TSP1 immunoreactivity is endothelial and excluded from thoracic branch point orifices.
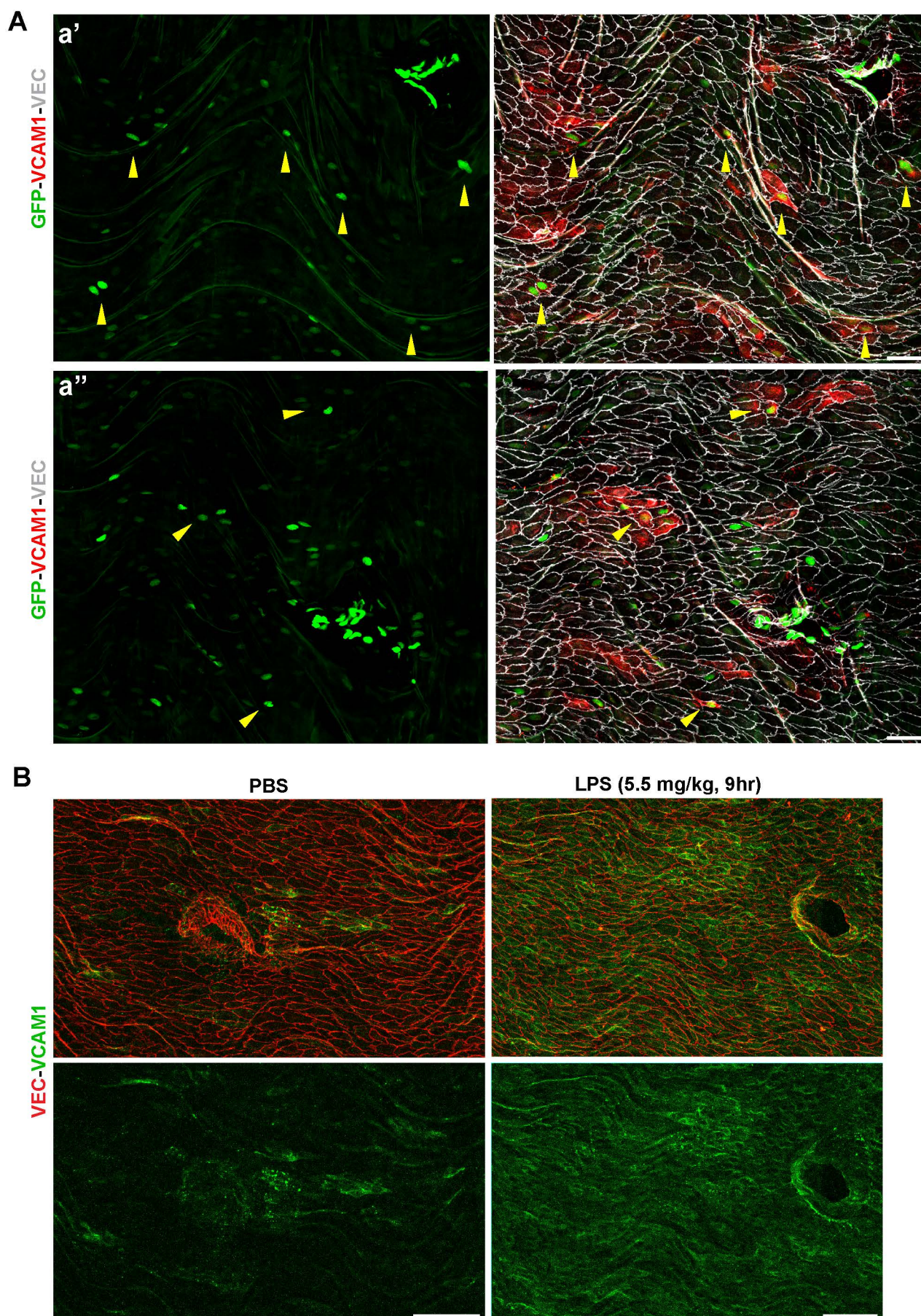
Figure 5 supplement 2. VCAM1 is LPS-inducible and expression is observed in GFP+ ECs distal from thoracic branch point orifices.
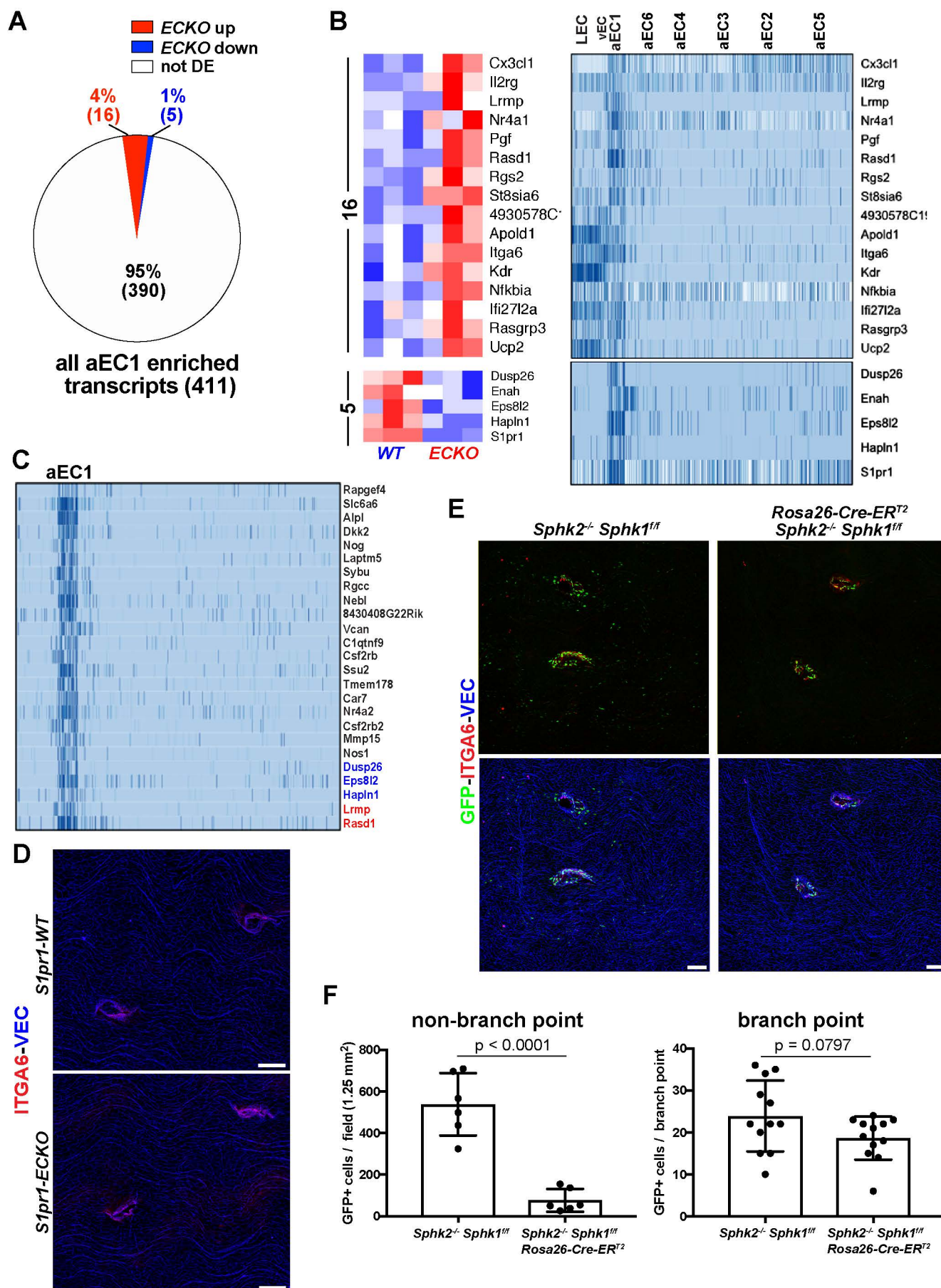
Figure 6. Gene expression in aEC1 cells is largely independent of S1P/S1PR1 signaling.
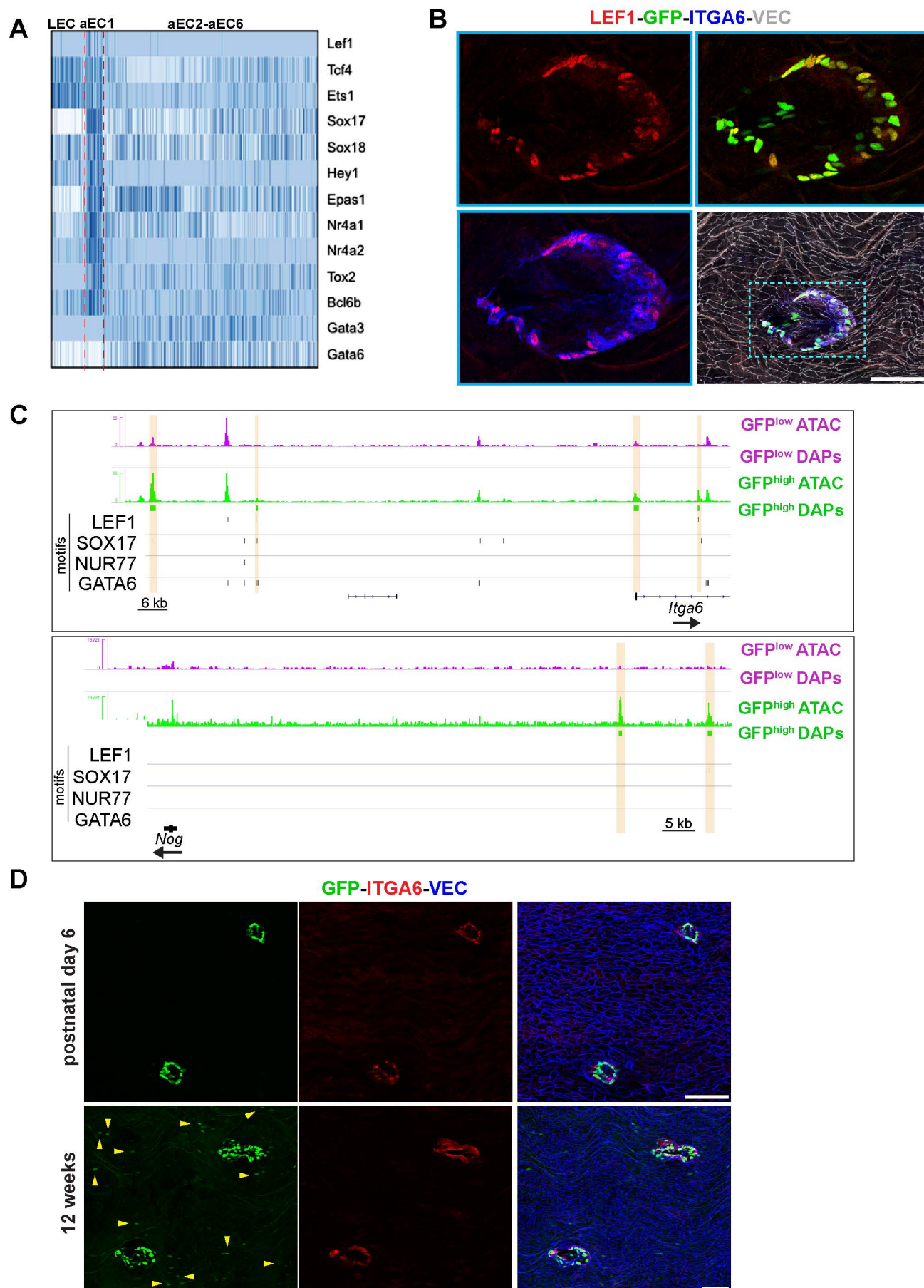
Figure 7. Transcription factors enriched and depleted in aEC1 cells.
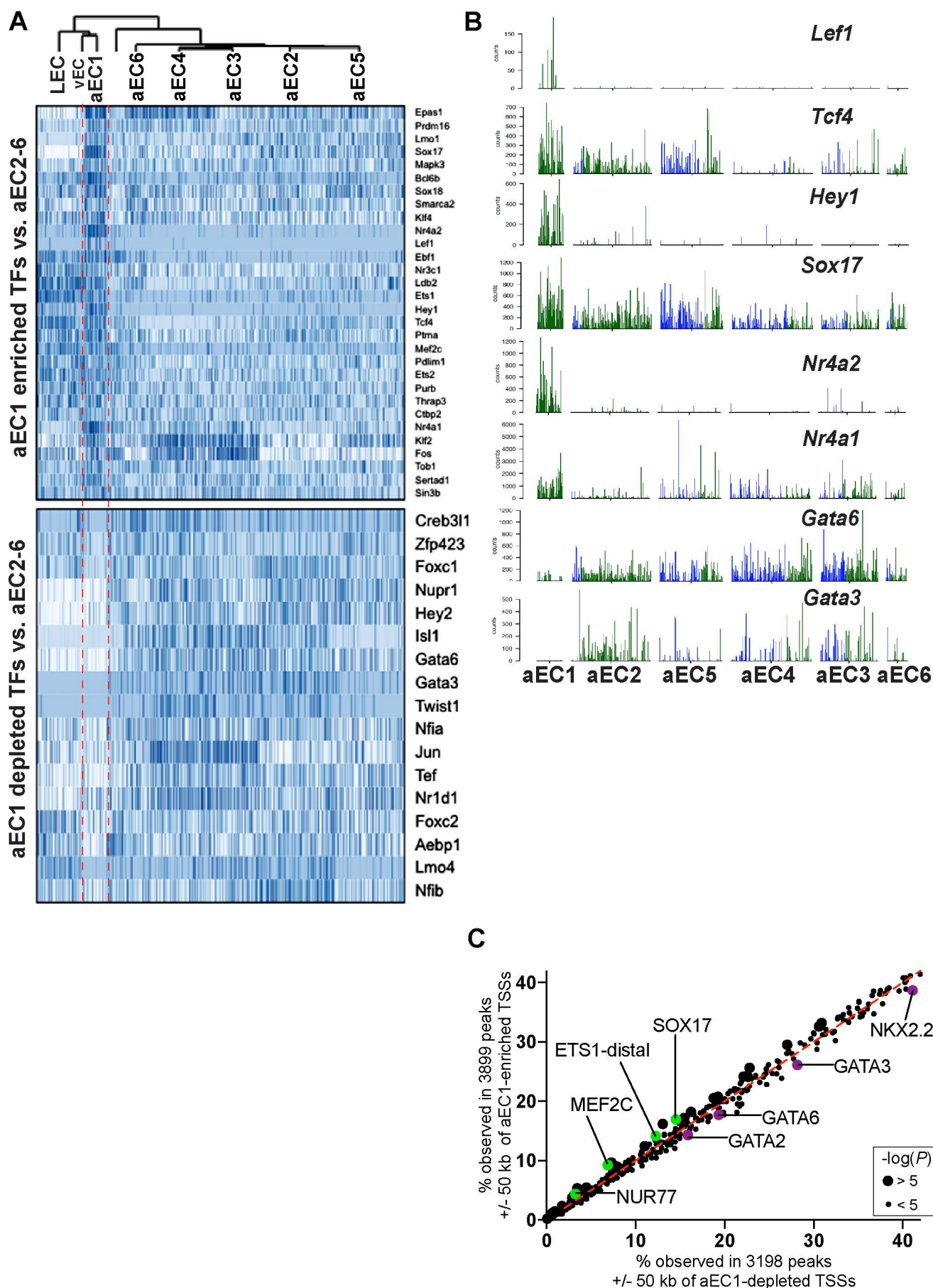
Figure 7 supplement 1. Transcription factors enriched and depleted in aEC1 cells.

A
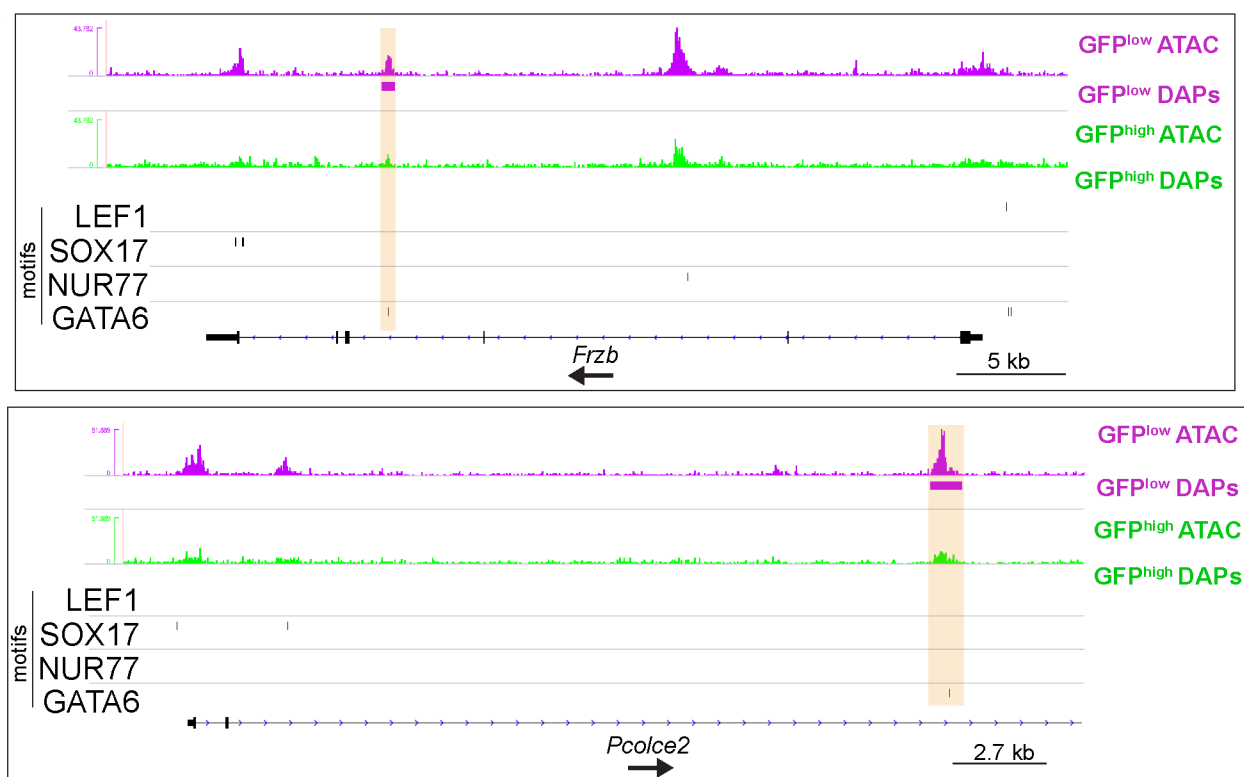
Figure 7 supplement 2. GATA6 motifs in GFP^low MAECs open chromatin within aEC4-enriched genes.

64

Figure 8. S1P is required for S1PR1/β-arrestin coupling in LECs of aorta-associated lymphatics.

A

B
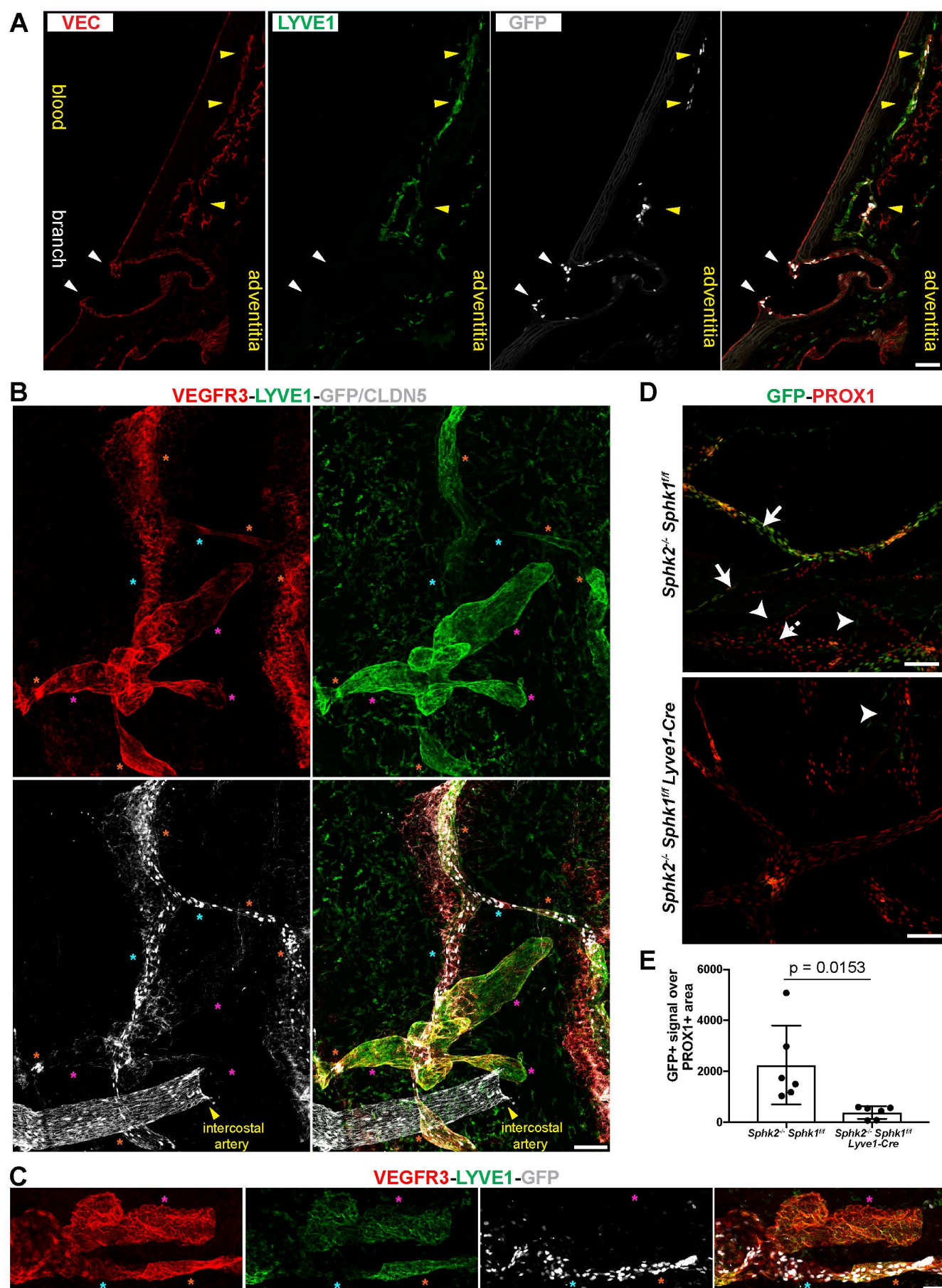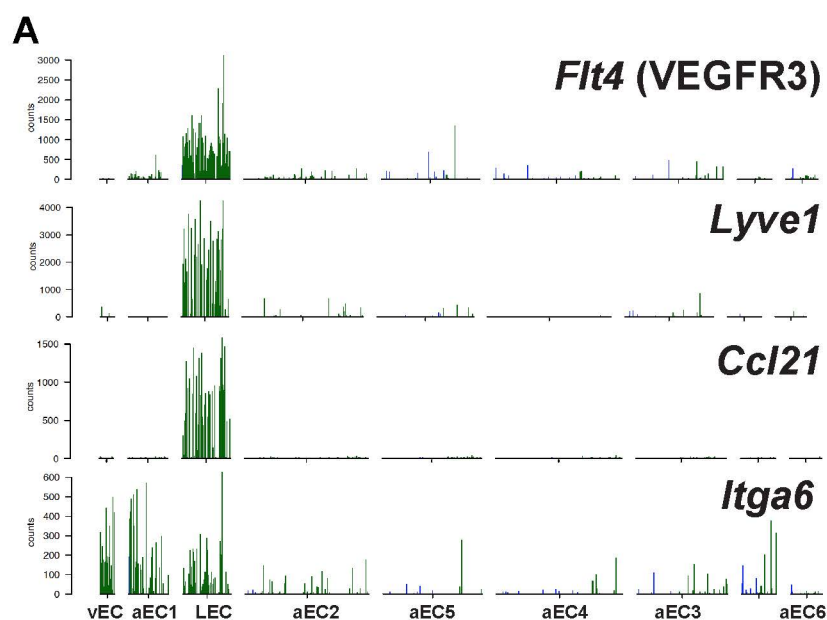
Figure 8 supplement 1. Expression of LEC transcripts and localization of ITGA6+ LEC and branch point arterial EC in close proximity.

A

258 *S1pr1-ECKO* upregulated transcripts
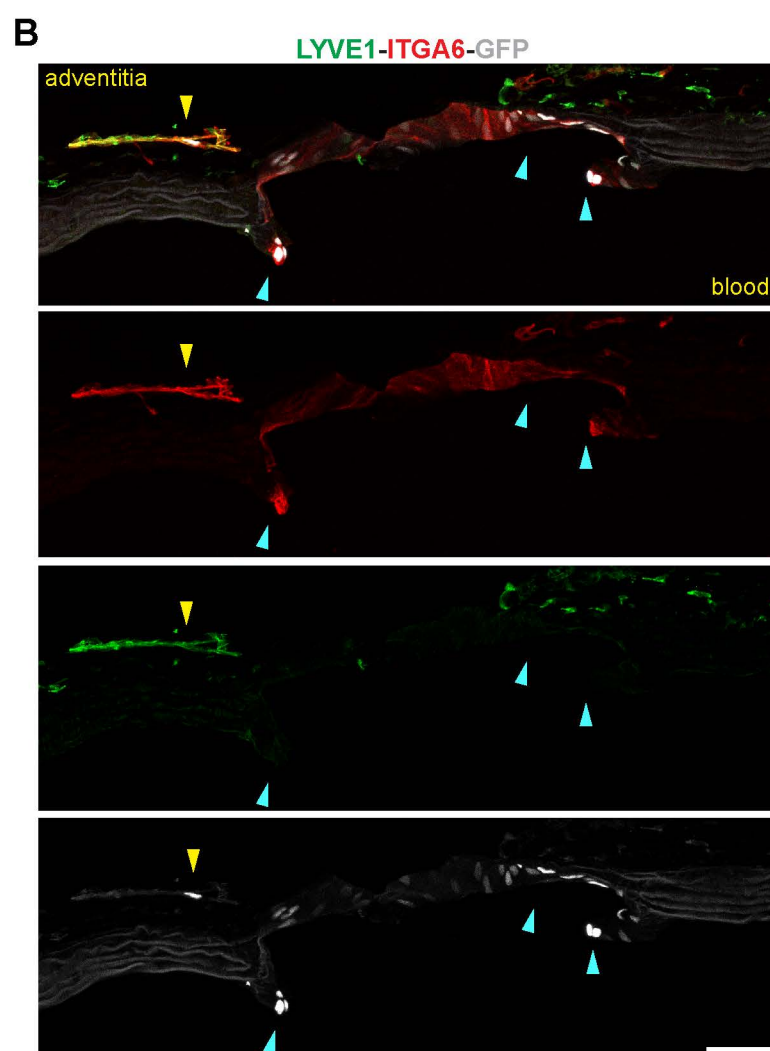
12% (20)
36% (58)
48% (78)

- LEC/vEC/aEC1 (5)
- LEC/vEC (12)
- LEC/aEC1 (3)
- LEC only (58)
- vEC only (4)
- aEC1 only (8)
- aEC2-aEC6 (7)
- not enriched in a cluster (161)

B

78 LEC transcripts

RTK/VEGF
- Vav3
- Nrp2
- Kdr
- Cyfip2
- Tec
- Pcsk6
- Sh3gl3
- Flrt2

GPCR signaling
- Wnt2
- Wnt9b
- Gng2
- Prkcq
- Ednrb
- Nts
- Htr2b
- Rgs16

Cytokine signaling
- Ccl21c
- Il7
- Nfkbia
- Rasgrp3
- Lbp
- Il33
- Fscn1
- Irf8

Serping1, Sema3a, Ptn, Adamtsl1, Mmrn1, Reln, Nid2, Igfbp5, Emid1, Pdpn, Scn3a, Ank3, Nr2f2, Itga6, Pard6g, Gmfg, Slc39a4, Slc8a4, Slc45a3, Ttyh1, Marcksl1, Kirb1f, Ston2, Kcnk5, Arhgap27, Hic1, Gjc2, Abba2, Tnfaip8l1, Hspa12a, Lyve1, Dtx1, Ucp2, Sgsm1, Glis3, Slc16al2, Duoxa2, Meox1, Myo1b, Sh3tc1, Ralgps2, Radil, Prox1, Bok, Stc1, Apold1, Tspan18, Kbtbd11, 4930578C19Rik, Trp53i11, Ifi27l2a, Fam65c, Pvrl2, Sept1

WT   ECKO

C

LYVE1-CCL21-GFP

C'

C''

intercostal artery

intercostal artery

D

LYVE1-CCL21-GFP-DAPI

branch   blood

adventitia

blood

blood

adventitia

adventitia

Figure 9. S1PR1 regulation of gene expression in aorta-associated LECs.

67

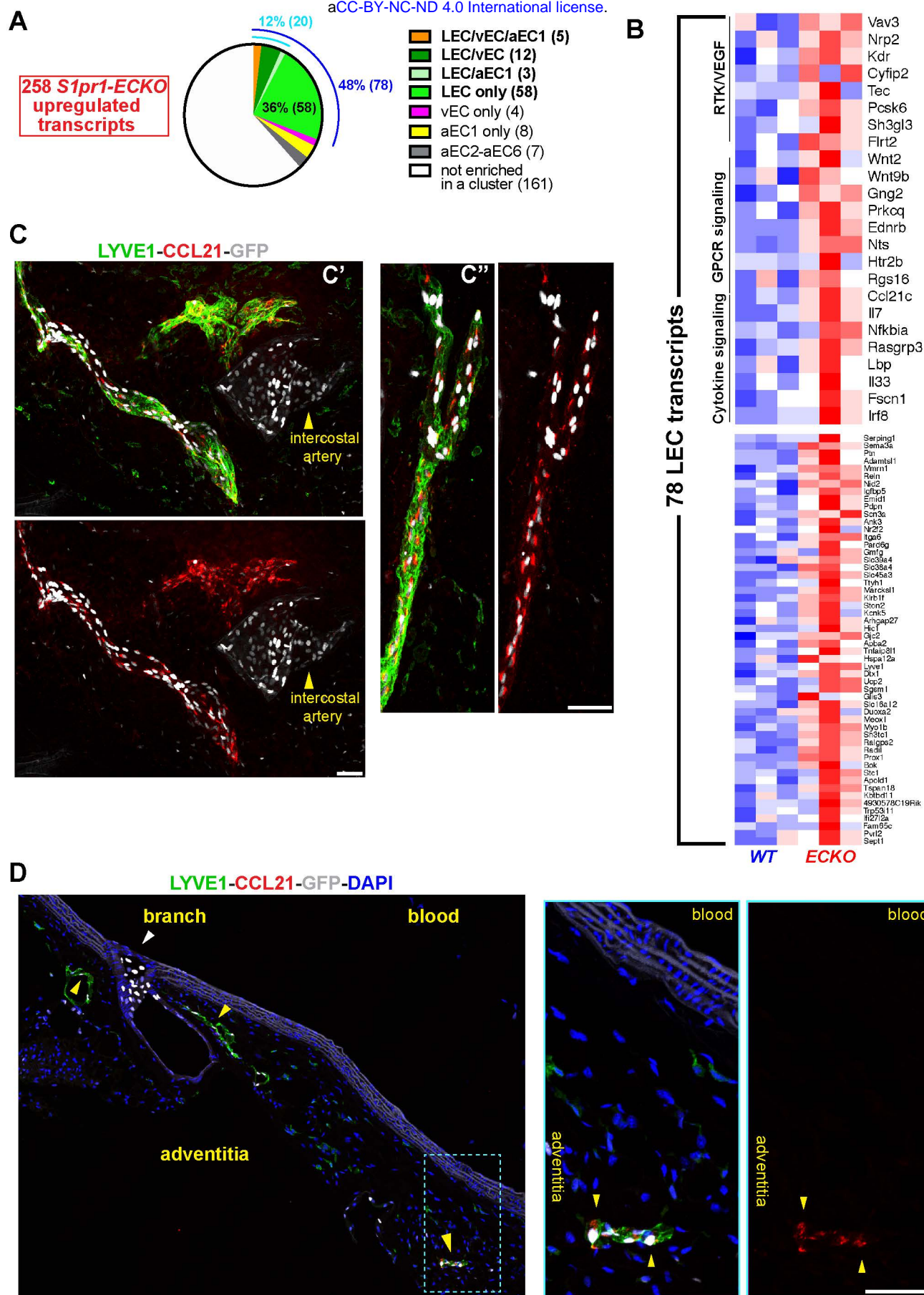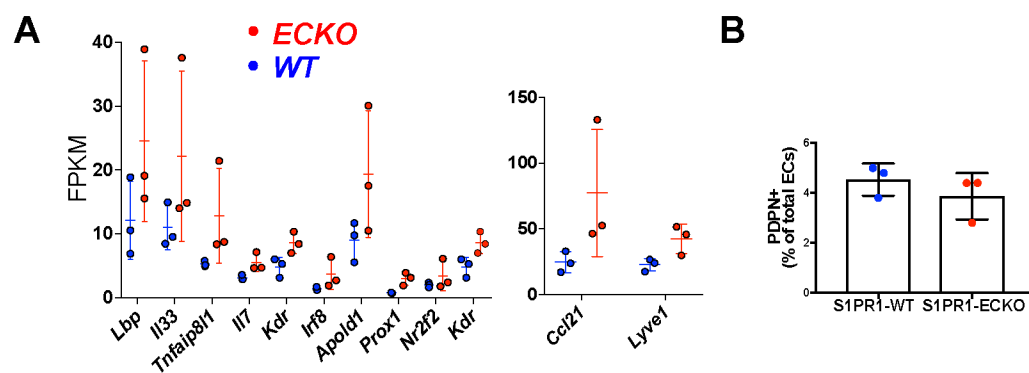**Figure 9 supplement 1.** Up-regulation of LEC transcripts in *S1pr1-ECKO* MAECs is not associated with a change in the proportion of aorta-associated PDPN+ LECs.
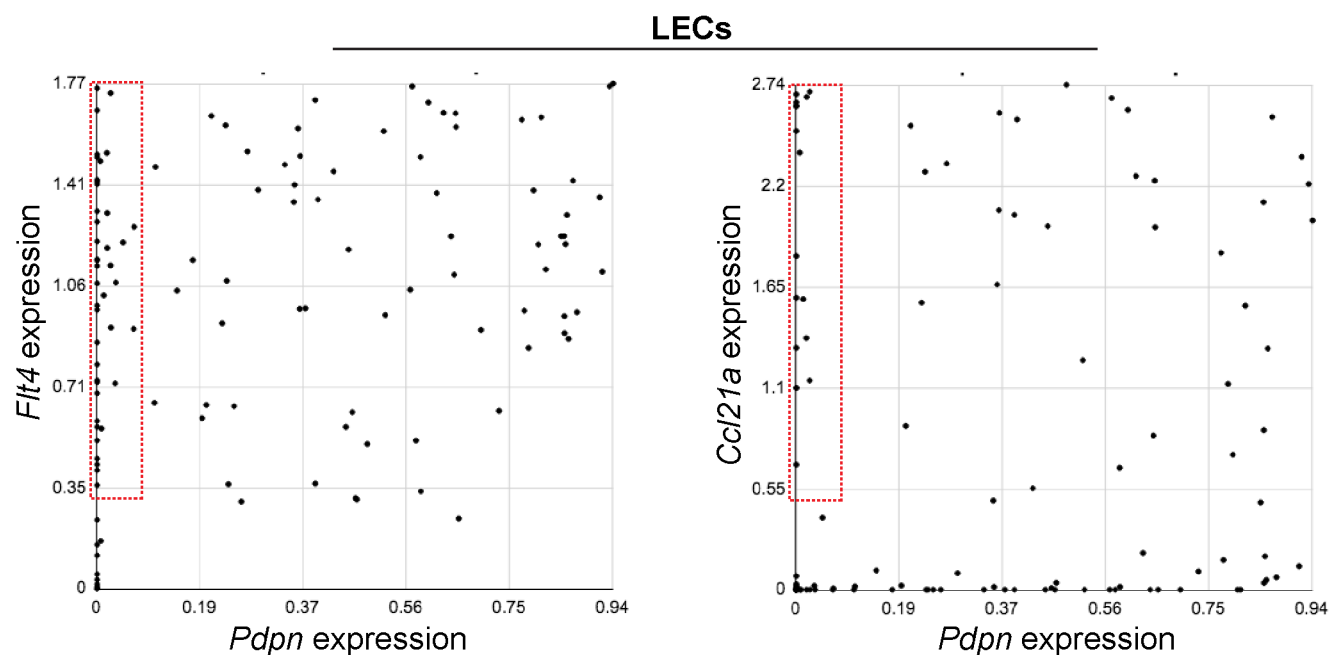
LECs

Figure 9 supplement 2. Heterogeneous LEC marker gene expression in aorta-associated LECs.

1 **Figure and Figure Supplement Legends**

2

3 **Figure 1. High S1PR1/ß-arrestin coupling in normal mouse aortic endothelium exhibits**

4 **transcriptomic concordance with S1PR1 loss-of-function.**

5 **(A)** *H2B-GFP* control and S1PR1-GS mouse thoracic aorta whole mount *en face* preparations.

6 Representative images from different regions of the aorta are presented and show H2B-GFP

7 (GFP), VE-Cadherin (VEC) or CD31, Ki67 (N=3) or Fibrinogen (N=2) immunostaining. Scale

8 bars are 50 μM. **(B)** FACS gating scheme used for isolation of GFP^{high} and GFP^{low} MAECs. *S1pr1-*

9 *ECKO* and *WT* MAECs were isolated using the GFP^{low} gate of this scheme (see Figure 1-figure

10 supplement 1A). **(C)** Venn diagram showing differentially expressed transcripts in the GFP^{high} vs.

11 GFP^{low} and *S1pr1-ECKO* vs. *WT* MAECs comparisons. The number of transcripts individually or

12 co-enriched (p-value < 0.05) are indicated for each overlap. **(D)** Selected upstream factors

13 identified by IPA analysis of GFP^{high} vs. GFP^{low} (top) and *S1pr1-ECKO* vs. *WT* (bottom) MAEC

14 comparisons. Activation Z-scores and P-values are indicated for each selected factor. **(E)**

15 Expression heatmaps (row Z-scores) of the 159 *S1pr1-ECKO* up-regulated transcripts also

16 differentially expressed between GFP^{high} and GFP^{low} MAECs. Selected transcripts are labeled

17 between the heatmaps from the comparison of *S1pr1-ECKO* vs *WT* (left) and GFP^{high} vs GFP^{low}

18 (right).

19

20 **Figure 1 supplement 1. RNA-seq quality control and differential gene expression between**

21 **GFP^{high} and GFP^{low} and *S1pr1-ECKO* and *WT* MAECs.**

22 **(A)** FACS gating scheme for isolation of *S1pr1-WT* and *S1pr1-ECKO*. MAECs were defined as

23 cells in the gate labeled "P6", (CD45$^-$Ter119$^-$CD31$^+$). **(B)** Expression, in fragments per kilobase

24 per million mapped fragments (FPKMs), of indicated transcripts from bulk RNA-seq of GFP^{high},

25   GFP^low, *S1pr1-ECKO* and *WT* MAECs. **(C-D)** Volcano plots of all transcripts (counts per million

26   > 1) illustrate those differentially expressed between GFP^high and GFP^low **(C)** and *S1pr1-ECKO*

27   and *WT* **(D)** MAECs (see Supplementary file 1). Highlighted transcripts are associated with TGFß

28   signaling, inflammatory pathways, and/or show common regulation in GFP^high and *S1pr1-ECKO*

29   MAECs. **(E)** GeneOverlap (Shen et al., 2013) results for the overlaps shown in Figure 1C. **(F)**

30   Expression of transcripts associated with lymphatic endothelial cells.

31

32   **Figure 2. S1PR1 loss-of-function and high levels of ß-arrestin coupling are associated with**

33   **an NFκB signature in open chromatin.**

34   **(A)** Venn diagrams illustrating all peaks (FDR < 0.00001) identified after analysis of individual

35   ATAC-seq replicates of GFP^low, GFP^high *S1pr1-ECKO*, and *WT* MAECs, and subsequent merging

36   of these peaks into a single consensus peak set. **(B)** Three individual experiments were performed

37   for GFP^low vs GFP^high and *S1pr1-ECKO* vs *WT* comparisons. Differentially accessible peaks

38   (DAPs) were determined using edgeR (FDR < 0.05, see Methods). **(C-F)** DAPs were input to the

39   HOMER "findMotifsGenome.pl" script (see also Supplementary File 2) and observed vs expected

40   frequencies of motif occurrances were plotted. **(G-H)** ATAC-seq reads were centered on Tn5 cut

41   sites, trimmed to 10 bp, and nucleotide-resolution bigwig files were generated using DeepTools

42   with reads per genomic content (RPGC) normalization. Reads were subsequently centered on TF

43   binding motifs identified in **(C-F)** and viewed as mean read densities across 600 bp windows.

44

45   **Figure 2 supplement 1. ATAC-seq quality control and peak annotation.**

71

46   **(A)** Enrichment of GFP^{high}, GFP^{low}, *S1pr1-ECKO* and *WT* MAECs peaks with respect to distance

47   from UCSC-annotated transcripts (mm9). Promoters are defined as +/- 1 kb from transcription

48   start sites. **(B)** ATAC-seq signal and peaks at *Cdh5* and *Gata1* loci.

49

50   **Figure 2 supplement 2. Genome-wide concordance between promoter-proximal chromatin**

51   **accessibility and mRNA expression in sorted MAEC populations.**

52   ATAC-seq and RNA-seq reads (RPGC-normalized) were examined from 3kb upstream and 3kb

53   downstream of all UCSC-annotated CDS's using the DeepTools ComputeMatrix function. Signal

54   was generated in bin sizes of 50 bp and 100 bp for ATAC-seq and RNA-seq, respectively.

55

56   **Figure 2 supplement 3. Genome-wide chromatin footprinting with HINT-ATAC.**

57   **(A)** The change in chromatin accessibility scores between GFP^{high} and GFP^{low} MAECs plotted

58   against the change in protection scores for each of the 579 queried JASPAR motifs. **(B)** Lineplots

59   of Tn5 cuts from GFP^{high} and GFP^{low} MAECs averaged over the sites identified in **(A)** for TCF7L2,

60   SOX17, and KLF14 motifs. **(C)** The same plot as **(A)** showing the differences between *S1pr1-*

61   *ECKO* and *S1pr1-WT* MAECs. **(D)** Lineplots of Tn5 cuts from *S1pr1-ECKO* and *S1pr1-WT*

62   MAECs averaged over the sites identified in **(C)** for NFKB2 and TEAD1 motifs.

63

64   **Figure 3. Single-cell RNA-sequencing of GFP^{high} and GFP^{low} MAECs.**

65   **(A)** t-SNE projection from Pagoda2 multilevel clustering of 767 GFP^{high} and 384 GFP^{low} MAECs.

66   Dash-line circles highlight each of the 9 clusters identified. Cells and cluster names are color-

67   coded according to cluster assignment. **(B)** Dendrogram from hierarchical clustering and

68   expression heatmap of selected genes. The dendrogram (top) reveals an upstream split between

69   LEC, vEC, aEC1 and aEC2, aEC3, aEC4, aEC5, and aEC6 populations. The heatmap shows the

70   gradient of expression, from low (white) to high (dark blue), for a selection of transcripts with

71   distinctive expression patterns. **(C-F)** Expression of transcripts specific to VSMCs **(C)** lymphatic

72   ECs **(D)**, venous ECs **(E)** and arterial ECs **(F)** are shown on the t-SNE embedding. **(G-J)**

73   Representative transcripts enriched in arterial EC (aEC) clusters 1 (G), 2 (H), 3 (I) and 4 (J) are

74   shown on the t-SNE embedding.

75

76   **Figure 3 supplement 1. Expression of cluster-defining transcripts in single GFP^{high} and**

77   **GFP^{low} MAECs.**

78   **(A-B)** Barplots of transcript counts of selected genes in individual GFP^{high} and GFP^{low} MAECs

79   cells. Each line represents a single cell.

80

81   **Figure 3 supplement 2. Top markers transcripts for each of the nine clusters defined by**

82   **scRNA-seq analysis of GFP^{high} and GFP^{low} MAECs.**

83   Heatmaps (cells are clustered as shown in Figure 3B) illustrate expression of the top 32 most

84   enriched transcripts in each cluster, according to Z-score.

85

86   **Figure 3 supplement 3. General features and nomenclature of the nine clusters defined by**

87   **scRNA-seq analysis of GFP^{high} and GFP^{low} MAECs.**

88   **(A)** Table summarizing characteristics of the nine clusters. **(B)** tSNE projection of the embedding

89   shown in Figure 1A with cells color-coded according to GFP expression.

90

91   **Figure 3 supplement 4. Transcripts co-enriched in LEC, vEC, and aEC1.**

92   **(A)** Heatmaps of sphingolipid-related transcripts showing enrichment in one or multiple EC

93   clusters. **(B)** Heatmaps of examples of transcripts co-enriched and depleted in LEC, vEC, and

94   aEC1 versus aEC2-6. Cell clustering is as shown in Figure 3B.

95

96   **Figure 4. Functional annotation of arterial MAECs clusters aEC1, aEC2, aEC3, and aEC4.**

97   **(A-D)** Selected pathways from GSEA analysis of cluster-enriched transcripts. Pathways enriched

98   in aEC1 **(A)**, aEC2 **(B)**, aEC3 **(C)**, and aEC4 **(D)** are shown with representeative transcripts

99   identified in each pathway (see also Supplementary File 5). The percent of GFP^{high} cells in each of

100   the four analyzed clusters are indicated at the bottom each heatmap.

101

102   **Figure 4 supplement 1. Expression of aortic EC cluster markers from Lukowski et al. (2019)**

103   **and Kalluri et al. (2019) in LEC, vEC, and aEC1-6.**

104   **(A)** Expression of "Cluster 1" and "Cluster 2" marker genes (Lukowski et al., 2019) in LEC, vEC,

105   and aEC1-6. **(B)** Expression of "EC1", "EC2", and "EC3" marker genes (Kalluri et al., 2019) in

106   LEC, vEC, and aEC1-6. Black arrows indicate enrichment in aEC1, red arrows indicate enrichment

107   in both LEC and aEC1, green arrows indicate enrichment in LEC, beige arrows indicate

108   enrichment in aEC2-6 and depletion from LEC, vEC, and aEC1.

109

110   **Figure 5. Identification of aEC1 as arterial ECs around the circumference of branch point**

111   **orifices.**

112   **(A)** Barplots of scRNA-seq read counts for *Nog*, *Itga6*, *Alpl*, *Cldn5*, *S100a4*, *Thbs1*, and *Vcam1* in

113   arterial EC clusters (aEC1-6). Each bar represents a single cell, either GFP^{high} (green bar) or GFP^{low}

114   (blue bar). **(B-H))** Confocal images of whole-mount *en face* preparations of mouse thoracic aortae

115   centered on intercostal branch points. **(B-C)** Immunostaining of S1PR1-GS mouse aortae for

116   Noggin (NOG) and CD31 **(B)**, or Integrin alpha-6 (ITGA6) and VE-Cadherin (VEC) **(C)**. **(D-E)**

117   Immunostaining of C57BL/6J mouse aortae for CD31 and Alkaline phosphatase, tissue-

118   nonspecific isozyme (ALPL) **(D)** or Claudin-5 (CLDN5), S100-A4 (FSP1), and VEC **(E)**. **(F)**

119   Immunostaining of S1PR1-GS mouse aorta for ITGA6, Thrombospondin 1 (TSP1), and VEC.

120   Yellow arrow indicate TSP1+ ECs. **(G)** Immunostaining of an S1PR1-GS mouse aorta for FSP1

121   and TSP1. The circumference of an intercostal branch point harbors FSP1+GFP+ cells, wereas

122   TSP1+GFP+ cells (cyan arrows) are distal from the circumference of the branch point orifice. **(H)**

123   Immunostaining of a mouse aorta for VCAM1 and VEC. Two rows of cells exhibiting the

124   morphology and VEC-localization of cells around branch point orifices are outlined. Scale bars

125   are 50 μM.

126

127   **Figure 5 supplement 1. Patchy TSP1 immunoreactivity is endothelial and excluded from**

128   **thoracic branch point orifices.**

129   **(A)** Whole-mount *en face* preparation of a mouse thoracic aorta immunostained for ITGA6, TSP1,

130   and VEC. Scale bar is 200 μM. **(B)** Two sagittal sections (b' and b'') of a mouse thoracic aorta

131   demonstrate TSP1 expression in VEC+ arterial ECs. Sections were counterstained with DAPI to

132   image nuclei. Scale bars are 20 μM.

133

134   **Figure 5 supplement 2. VCAM1 is LPS-inducible and expression is observed in GFP+ ECs**

135   **distal from thoracic branch point orifices.**

136   **(A)** Two fields (a' and a'') from a whole mount *en face* preparation of an S1PR1-GS mouse

137   thoracic aorta immunostained for VCAM1 and VEC. Yellow arrows indicate VCAM1+ GFP+

138   ECs distal from the branch point orifice. Scale bars are 50 µM. **(B)** Intraperitoneal administration

139   of LPS (5.5 mg/kg, 9hr) results in uniform VCAM1 induction in aortic ECs, visualized by VCAM1

140   and VEC immunostaining of thoracic aorta whole mount *en face* preparations. Scale bars are 100

141   µM.

142

143   **Figure 6. Gene expression in aEC1 cells is largely independent of S1P/S1PR1 signaling.**

144   **(A)** Pie chart of all aEC1-enriched transcripts (versus aEC2-6) indicating those which were also

145   differentially expressed in *S1pr1-ECKO* MAECs. **(B)** Heatmap (row Z-scores) of the 20 transcripts

146   that were both S1PR1-regulated and aEC1-enriched (left). Expression of these transcripts in each

147   cluster from scRNA-seq analysis is shown (right). **(C)** Gene expression in aEC1 was compared to

148   all ECs (LEC, vEC, and aEC2-6 collectively). All transcripts expressed greater than 16-fold higher

149   in aEC1 are shown (25 transcripts total). Red, blue and black transcript names indicate up-

150   regulated, down-regulated or similar levels of expression in *S1pr1-ECKO* MAECs, respectively.

151   **(D)** Immunostaining of *S1pr1-ECKO* and *WT* aortae whole mount *en face* preparations for ITGA6

152   and VEC. Images are representative of observations from two pairs of animals (N=4). **(E)** ITGA6

153   and VEC immunostaining of whole mount *en face* preparations of thoracic aortae from S1PR1-GS

154   mice bearing *Sphk2$^{-/-}$ Sphk1$^{f/f}$* or *Sphk2$^{-/-}$ Sphk1$^{f/f}$ Rosa26-Cre-ER^{T2}* alleles. **(F)** Quantification of

155   GFP+ arterial EC at branch point (n=12) and non-branch point (n=6) locations (n=2 mice for each

156   genotype). Branch point EC were defined as cells included in the first three rows around the edge

157   of orifices. Only GFP+ EC in the same Z-plane as surrounding arterial EC were counted (GFP+

158   EC of intercostal arteries were in a different Z-plane and therefore were not counted as branch

159   point EC). All scale bars are 100 µM.

160

161 **Figure 7. Transcription factors enriched in aEC1 cells.**

162 **(A)** Heatmap of selected transcription factors enriched and depleted in aEC1 cells (see also Figure

163 7-figure supplement 1A). **(B)** Immunostaining of an S1PR1-GS mouse thoracic aorta for

164 Lymphoid enhancer-binding factor 1 (LEF1), ITGA6, and VEC. Image is representative of

165 observations from 6 total branch points from 2 animals. Scale bar is 100 μM. **(C)** Genome browser

166 images of GFP^{high} and GFP^{low} MAECs ATAC-seq signal (RPGC normalized) at *Itga6* and *Nog*

167 loci. Peaks with increased accessibility in GFP^{high} MAECs (GFP^{high} DAPs) are indicated. All

168 LEF1, Nuclear receptor subfamily 4 group A member 1 (NUR77), Transcription factor SOX-17

169 (SOX17), and Transcription factor GATA-6 (GATA6) motifs identified in consensus peaks

170 (Figure 2A) are also shown. Orange bars highlight GFP^{high} MAECs DAPs harboring LEF1,

171 SOX17, and/or NUR77 motifs. **(D)** Immunostaining of postnatal day 6 (P6) (n=2) and 12-week

172 (n=4) S1PR1-GS mice thoracic aortae for ITGA6 and VEC. Scale bars are 100 μM.

173

174 **Figure 7 supplement 1. Transcription factors enriched and depleted in aEC1 cells.**

175 **(A)** Heatmaps (cells are clustered as shown in Figure 3B) illustrate expression of transcription

176 factors (TFs) enriched or depleted from aEC1 relative to aEC2-6. **(B)** Barplots illustrate transcript

177 counts of selected TFs from **(A)** in arterial ECs clusters aEC1-6. **(C)** The HOMER script

178 "findmotifsgenome.pl" was used for motif enrichment analysis of merged GFP^{high} and GFP^{low}

179 peaks that intsersected a 100 kb window centered on aEC1-enrichd (Z-score > 3) and depleted (Z-

180 score < -3) TSSs.

181

182 **Figure 7 supplement 2. GATA6 motifs in GFP^{low} MAECs open chromatin within aEC4-**

183 **enriched genes.**

184 **(A)** Genome browser images of *Itga6* and *Gata1*. Peaks with increased accessibility in GFP^{low}

185 MAECs are indicated (GFP^{low} DAPs), as well as LEF1, SOX17, NUR77, and GATA6 motifs in

186 consensus peaks (see Figure 2A). Orange bars highlight co-incidence of GATA6 motifs and

187 increased accessibility in GFP^{low} MAECs.

188

189 **Figure 8. S1P is required for S1PR1/ß-arrestin coupling in LECs of aorta-associated**

190 **lymphatics.**

191 **(A)** Confocal images of a sagittal cryosection (14 µM) of an S1RP1-GS mouse aorta

192 immunostained for VE-Cadherin and Lymphatic vessel endothelial hyaluronic acid receptor 1

193 (LYVE1). White arrows indicate GFP+ arterial ECs at a branch point orifices and yellow arrows

194 indicate adventitia-associated GFP+ LECs. Scale bar is 50 µM. **(B-C)** Confocal images of whole-

195 mount preparations of S1RP1-GS mouse thoracic aortae immunostained for Vascular endothelial

196 growth factor receptor 3 (VEGFR3; *Flt4*), LYVE1, and CLDN5 with the tunica intima **(B)** or

197 tunica adventitia **(C)** in contact with coverslip. Orange stars indicate VEGFR3+LYVE1+GFP+

198 areas, cyan stars indicate VEGFR3+LYVE1^{low}GFP+ areas, and magenta stars indicate

199 VEGFR3+LYVE1+GFP- areas. Scale bars are 100 µM **(B)** and 50 µM **(C)**. **(D)** Representative

200 images of mesentery lymphatics from S1PR1-GS mice bearing *Sphk2$^{-/-}$:Sphk1$^{f/f}$* (n=3) or *Sphk2$^{-/-}$*

201 *:Sphk1$^{f/f}$:Lyve1-Cre* (n=3) alleles whole mounted and immunostained for PROX1. Solid arrows:

202 GFP+PROX1+, dashed arrows: GFP-PROX1+, arrowheads: GFP+PROX1- (arterioles). Scale bar

203 is 100 µM. **(E)** Quantification of GFP+ signal over PROX1+ areas (N=6). Scale bars are 100 µM.

204

205 **Figure 8 supplement 1. Expression of LEC transcripts and localization of ITGA6+ LEC and**

206 **branch point arterial EC in close proximity.**

207   **(A)** Barplots illustrate transcript counts of *Flt4* (VEGFR3), *Lyve1*, *Ccl21*, and *Itga6* in each of the

208   nine clusters identified by scRNA-seq analysis. **(B)** Immunostaining of a sagittal section of a

209   S1PR1-GS mouse thoracic aorta for ITGA6 and LYVE1. White arrows indicate

210   GFP+ITGA6+LYVE1- arterial ECs of the branch point orifice. The yellow arrow indicates a GFP+

211   ECs associated with an adventitial LYVE1+ITGA6+ structure. Scale bar is 50 µM.

212

213   **Figure 9. S1PR1 regulation of gene expression in aorta-associated LECs.**

214   (**A**) Pie-chart distribution of *S1pr1-ECKO* MAECs up-regulated transcripts. The 258 transcripts

215   were binned according to their cluster assignment from scRNA-seq analysis. The blue and cyan

216   numbers indicate the total percentage of transcripts enriched in LEC and LEC plus at least one

217   cluster, respectively. The numbers in parentheses are absolute transcripts numbers. (**B**) Heatmap

218   (row Z-scores) of all 78 *S1pr1-ECKO* MAECs up-regulated transcripts that are LEC-enriched.

219   Selected GSEA pathways are identified in the top heatmap. (**C**) Confocal images of two fields (c'

220   and c'') of a whole-mounted S1RP1-GS mouse thoracic aorta immunostained for LYVE1 and C-

221   C motif chemokine 21 (CCL21). The tunica adventitia was facing the coverslip. **(D)** Confocal

222   images of a sagittal cryosection (14 µM) of an S1RP1-GS mouse thoracic aorta immunostained

223   CCL21 and LYVE1. Yellow arrows indicate adventitia-associated CCL21+LYVE1+GFP+ cells

224   and the white arrow indicate GFP+LYVE1- cells at a branch. Scale bars are 50 µM.

225

226   **Figure 9 supplement 1. Up-regulation of LEC transcripts in *S1pr1-ECKO* MAECs is not**

227   **associated with a change in the proportion of aorta-associated PDPN+ LECs.**

228　**(A)** FPKMs of selected transcripts from Figure 9B. (B) Aortae were digested and subjected to flow

229　cytometric analysis as described in Figure 1B. PDPN (PE-Cy7-conjugated) was added to the

230　staining cocktail to distinguish aorta-associated LECs from the remainder of aortic ECs.

231

232　**Figure 9 supplement 2. Heterogeneous LEC marker gene expression in aorta-associated**

233　**LECs.**

234　Expression of *Flt4* vs *Pdpn* (left) or *Ccl21a* vs *Pdpn* (right) was compard in individual LECs. The

235　red boxes indicate cell expressing *Flt4* but not *Pdpn* (left) or *Ccl21a* but not *Pdpn* (right).